UNIVERSITY OF OKLAHOMA

GRADUATE COLLEGE

SIMULATED EFFECTS OF URBAN ENVIRONMENTS ON THE DYNAMICS OF A SUPERCELL THUNDERSTORM

A DISSERTATION

SUBMITTED TO THE GRADUATE FACULTY

in partial fulfillment of the requirements for the

Degree of

DOCTOR OF PHILOSOPHY

By

LARISSA JOY REAMES

Norman, Oklahoma

2017

SIMULATED EFFECTS OF URBAN ENVIRONMENTS ON THE DYNAMICS OF A SUPERCELL THUNDERSTORM

A DISSERTATION APPROVED FOR THE SCHOOL OF METEOROLOGY

BY

Dr. David J. Stensrud, Co-Chair

Dr. David B. Parsons, Co-Chair

Dr. Alan Shapiro

Dr. Petra M. Klein

Dr. Kirsten de Beurs

To my mother.

Acknowledgements

The saying goes that no (wo)man is an island, and I certainly could never have completed this work without the contributions of innumerable friends, colleagues, mentors, and family along the way. First of all, I must thank and acknowledge my advisor, Dr. David Stensrud. Through his careful guidance, I have acquired a wealth of scientific knowledge and immeasurable confidence in my abilities as a scientist. Even when he was drawn to a new, very demanding position halfway across the country, he always made sure I was a priority, and I could have asked for nothing more from an advisor. I also need to thank Dr. Patrick Marsh who, when I was in need of a PhD advisor on short notice, thought to suggest that I contact Dr. Stensrud about an open position, without me ever asking for such a favor. Without this suggestion, I never would have been blessed with the fantastic opportunity to work with a wonderful scientist who I can now certainly call a mentor, colleague, and friend.

I also owe a debt of gratitude to Dr. Kim Elmore. His conversations led me to using hierarchical clustering analysis, a method of which I was completely unaware, as a key component to this dissertation. Without his insightful guidance, the work in this dissertation never would have been possible. I would also like to thank my Masters thesis advisor, Dr. Charles Doswell. His excellent, at times tough, guidance provided me with a great deal of confidence in my abilities as a public speaker and presenter, which made the endless string of presentations required of a graduate student far less stressful than they would have been otherwise.

My committee members, Drs. Kirsten de Beurs, Petra Klein, David Parsons,

and Alan Shapiro, are worthy of a great deal of my gratitude. They have provided wonderful feedback and discussions throughout the dissertation process, and numerous helpful suggestions to make this dissertation better. In addition, the NLCD data that are used throughout this dissertation were acquired and processed in to a usable form by Jess Walker, which was extremely helpful. Also, the majority of Chapter 3 is taken from a publication currently in press, and I would like to thank the anonymous reviewers for their helpful insights and suggestions.

Of course, none of this would have been possible without the continuous support of my entire family, especially my mother. She always encouraged me to follow my dreams, never hesitating to help me however she could, even if that meant answering to the best of her abilities the endless stream of questions about the weather from my 3-year-old self. I must also thank my best friend of ten years, understanding, patient officemate of 7 years, and honorary family member, Dr. Kevin Haghi. I'm grateful that he put up with my hatred of chewing noises, even if that meant I got irrationally angry at him on occasion.

This research was supported in part by the NASA Interdisciplinary Science program grant NNX12AM89G. This research is also part of the Blue Waters sustained-petascale computing project, which is supported by the National Science Foundation (awards OCI-0725070 and ACI-1238993) and the state of Illinois. Blue Waters is a joint effort of the University of Illinois at Urbana-Champaign and its National Center for Supercomputing Applications. Some of the data used in this study were acquired as part of the mission of NASA's Earth Science Division and archived and distributed by the Goddard Earth Sciences (GES) Data and Information Services Center (DISC). Rainfall data provided by NCAR/EOL under sponsorship of the National Science Foundation. Also, this dissertation was typeset with LaTeXby the author using the OU dissertation

package developed by Dr. Brian Fiedler–without this, I certainly would have required numerous bottles of pain relievers while wrangling with MS Word.

Table of Contents

List of Tables

List of Figures

Abstract

The world's population is increasingly concentrated in large urban areas. Many observational and modeling studies have explored how large, population-dense cities modify local and mesoscale atmospheric phenomena. Urban modeling studies often use an explicit urban canopy model to parameterize urban surfaces. However, it is unclear whether this approach is appropriate for more suburban cities, such as those found in the Great Plains. To investigate this problem, the Weather Research and Forecasting model is used to simulated a week of conditions in and around the Oklahoma City, Oklahoma area, and results from these simulations are compared with observations. Overall, five simulations with varying urban land-surface parameterization configurations are examined. Three simulations use the Noah land surface model (LSM): one with all urban areas removed, one using the original Noam LSM, and the other with urban areas parameterized by a modified Noah LSM with three urban categories. Additional simulations utilize a single layer urban canopy model either with default urban fraction values or with urban fractions taken from the National Land Cover Database. In general, all simulations produce warmer, drier urban areas, with a stronger urban heat island at night. However, the prediction of near-surface winds is problematic in the two simulations that use the single layer urban canopy model as neither simulation correctly reproduces reduced wind speeds over the city. The modified Noah LSM provides the best overall agreement with observations and represents a reasonable option for simulating the urban effects of more suburban cities.

The effect of urban areas on weakly-forced precipitation systems has also been

studied extensively. However, interactions between urban areas and synoptically-active convection, such as supercells, remain relatively unexamined. Simulations of a supercell thunderstorm, with an urban area parameterized using the modified Noah LSM scheme, are used to quantify the impacts of a large Plains urban area on the evolution and strength of a supercell thunderstorm. Simulations with urban areas are compared to an initial-condition ensemble of simulations without any urban areas, with hierarchical clustering analysis used to form statistically similar groups of simulations. In this analysis, the effects of the storm having various city-relative paths, as well as the storm life cycle stage during urban interactions, are investigated. The results suggest that, when the storm passes to the north of or directly over the city center late in its life cycle, low-and mid-level mesocyclone strength increases, and the mesocyclone tracks further south. In general, low-level storm characteristics are more sensitive to the location of the city than are mid-level storm properties.

To supplement this analysis, a factor separation approach is undertaken to determine the relative importance of the roughness and thermal characteristics of urban areas on storm modification. City locations near the beginning and end of the storm's life cycle are used to determine if the storm's maturity while interacting directly with the city modulates these effects. Results generally suggest that surface roughness and its interactions between thermodynamic properties are the dominant contributors to urban-induced effects on storm strength and evolution. Additionally, the amplitude of interactions between shear and thermodynamic modifications is often similar in magnitude to either effect individually.

Chapter 1

Introduction

A large body of research (e.g., Shepherd 2005; Shepherd et al. 2010b) suggests that urban areas modify atmospheric properties in their vicinity due to the special properties of urban areas (e.g., surface albedo and emissivity, anthropogenic emissions, etc.) (Oke 1976, 1981, 1982; Arnfield 2003; Barlow 2014). To better understand urban-rural differences, researchers have undertaken efforts in the past few decades to observe and quantify the range of effects that urban areas can have on the environment. Studies involving first-order urban effects focus almost exclusively on urban-induced near-surface warming, particularly at night (e.g. Gedzelman et al. 2003; Yow and Carbone 2006; Alonso et al. 2007; Basara et al. 2008; Yang et al. 2013; Smoliak et al. 2015; Hu et al. 2016), which is frequently referred to as the urban heat island (UHI; Oke 1982). Although not as well-documented, in-situ measurements also suggest slower wind speeds in the city, most prominently during the day (Bornstein and Johnson 1977; Dou et al. 2015; Hu et al. 2016), and decreased humidity (Dou et al. 2015) in urban areas.

Modifications of microscale atmospheric properties by urban areas can also affect mesoscale and storm-scale weather phenomena. For example, researchers have observed urban areas across the globe to cause earlier arrival of Spring (Alonso et al. 2007), fewer freezing rain events (Changnon 2003), and more severe floods (e.g. Smith et al. 2002). Of particular relevance to the present study is the effect that urban areas have on intense convection; a wide breadth of research

indicates that convective precipitation pattern, frequency, and intensity can be altered as a consequence of urban modifications of temperature, humidity, and flow structure (e.g. Huff and Changnon 1973; Changnon 1979; Changnon et al. 1991; Bornstein and Lin 2000; Shepherd et al. 2002; Shepherd and Burian 2003; Burian et al. 2005; Dou et al. 2015; Seino et al. 2016). Research also suggests that urban aerosols can cause altered lightning frequency (e.g., Orville et al. 2001; Rose et al. 2008; Tan et al. 2016), though aerosols will not be addressed in this study.

Earth's population is increasingly concentrated in urban areas, with nearly two-thirds of the world's population expected to live in urban areas by 2050 (United Nations 2015). As the number of people within cities grows, it is becoming more important to understand, and to be able to correctly predict (especially via numerical modeling), the interactions between urban environments and the atmosphere. Hence, this study will simulate the interaction between an isolated supercell and a large plains urban environment after first identifying the best urban parameterization to use in these simulations. These analyses will be supplemented by a factor separation analysis in an attempt to determine which aspects of the urban environment most affect supercell strength and evolution.

1.1 Motivation and previous work

1.1.1 Direct urban effects on the atmosphere

While the exact mechanisms through which urban areas modify their environment are not fully understood, the meteorological conditions observed in urban areas are likely caused by a multitude of factors (Table 1.1). The majority of research involving these mechanisms focuses on the UHI. The primary culprit of the UHI effect is the modification of surface properties, such as albedo, emissiv-

Table 1.1: Suggested causes of the urban heat island (not rank ordered). (Adapted from Oke 1982)

Altered energy balance terms leading to positive thermal anomaly	Features of urbanization underlying energy balance changes
A. Canopy Layer	
1. Increased absorption of short-wave radiation	Canyon geometry – increased surface area and multiple reflection
2. Increased long-wave radiation from the sky	Air pollution – greater absorption and re-emission
3. Decreased long-wave radiation loss	Canyon geometry – reduction of sky view factor
4. Anthropogenic heat source	Building and traffic heat losses
5. Increased sensible heat storage	Construction materials – increased thermal admittance
6. Decreased evapotranspiration	Construction materials – increased 'water-proofing'
7. Decreased total turbulent heat transport	Canyon geometry – reduction of wind speed
B. Boundary Layer	
1. Increased absorption of short-wave radiation	Air pollution – increased aerosol absorption
2. Anthropogenic heat source	Chimney and stack heat losses
3. Increased sensible heat input from below	Canopy heat island – increased heat flux from canopy layer and roofs
4. Increased sensible heat input from above	Heat island, roughness – increased turbulent entrainment

ity, and thermal conductivity, in the urban area due to the replacement of natural vegetation with man-made materials. Though the albedo of urban materials can vary ($\alpha_{asphalt} \simeq 0.05$, $\alpha_{concrete} \simeq 0.55$), artificial materials used for construction typically have a higher thermal admittance, resulting in greater heat storage and increased sensible heat release, particularly at night. Additionally, by replacing natural, evaporating surfaces by generally water-proof materials, latent heat flux is reduced. This results in drier urban air, thus compounding the effect of higher sensible heat flux. Air pollution, by increasing absorption and re-emission of radiation, contributes both to increased sensible heating and decreased long-wave radiation loss at night. Anthropogenic heat release, though typically only important in very large cities, is also a direct contributor to increased sensible heating in the urban area. A warm urban area also results in increased turbulent mixing

near the surface, which provides an additional source of sensible heat due to turbulent entrainment, though this process may be tempered by the impedance of urban structures. (Oke 1982; Oke et al. 1991). Together, these complicated processes generally result in warmer temperatures in urban areas, up to $4-5^{\circ}$C under ideal conditions at night(e.g., Aase and Siddoway 1982; Hu and Xue 2016).

Tall buildings in urban areas also modify winds near the surface due to increased surface roughness length, z_0 (Oke 1987). Bornstein and Johnson (1977) observed slower winds over the New York City urban area. As a result, the Coriolis force decreased, causing a counter-clockwise turning of the winds as they passed over and downstream of the urban area. More recent observational investigations (e.g., Dou et al. 2015; Hu et al. 2016) have observed $\sim 10-20\%$ slower wind speeds over urban areas during the day when wind rural speeds are moderate, which they attribute to urban surface roughness impeding the flow.

These land-atmosphere interactions can also be modulated by larger-scale meteorological conditions. Moderate wind speeds at night increase boundary layer turbulence, which acts as an equalizer for urban-rural temperature differences through turbulent heat transport (e.g., Alonso et al. 2007; Hu et al. 2013, 2016). Similarly, cloud cover acts as an insulator that prevents heat loss to the free atmosphere at night, hence increasing rural temperatures and decreasing the UHI intensity (UHII; e.g., Alonso et al. 2007), or the difference between urban and rural near-surface temperatures, and urban boundary layer development. . Wet soils cool more slowly at night, hence precipitation also causes warmer rural nighttime temperatures (e.g., Oke et al. 1991), while drought conditions can result in higher rural daytime soil temperatures, minimizing or reversing (i.e., cooler urban than rural temperatures) the daytime UHII (e.g., Winguth and Kelp 2013; Husain et al. 2014). These examples illustrate the complicated processes that create, modify, and maintain the UHI, which motivates the continued

observational and modeling studies involving the urban area and its multitude of effects.

1.1.2 Modeling urban effects

Recent studies have used the Noah land surface model (LSM; Chen and Dudhia 2001; Ek 2003) coupled with a single-layer urban canopy model (SLUCM; Kusaka et al. 2001; Kusaka and Kimura 2004) in the Advanced Research Weather Research and Forecasting (ARW-WRF Skamarock and Klemp 2008) model to investigate land-atmosphere interactions in urban areas. Researchers have performed modeling studies in large, dense cities across the globe, such as New York City (Gutiérrez et al. 2015a), Taipei, Taiwan (Lin et al. 2008), Beijing, China (Miao et al. 2009), Baltimore-Washington D.C. (Zhang et al. 2011; Li et al. 2013), Mexico City (Cui and de Foy 2012), Hangzhou, China (Chen et al. 2014), Tokyo, Japan (Adachi et al. 2014; Takane et al. 2015), and Nanjing, China (Chen et al. 2015). Although less numerous, some studies have used the LSM-SLUCM framework in the WRF to model urban effects of smaller or less-dense cities such as Las Vegas (Kamal et al. 2015), Dallas-Fort Worth, Texas (Hu et al. 2016), Oklahoma City (Hu et al. 2013), Houston, Texas (Chen et al. 2011), and Phoenix, Arizona (Grossman-Clarke et al. 2010; Shaffer et al. 2015). These investigations showed that using the SLUCM to parameterize urban areas improves model representation of UHI intensity (UHII), or the difference between urban and rural near-surface temperatures, and urban boundary layer development.

In the WRF LSM-SLUCM modeling framework, the Noah LSM is used to compute surface fluxes in all non-urban grid points based on vegetative and soil properties such as surface roughness, emissivity, and albedo, as well as soil moisture and temperature. In urban areas, the SLUCM is used to compute

fluxes in the urban canopy, taking into account building materials, building height, and more complex surface geometry. The LSM is also used at these locations to compute fluxes, however the LSM considers the grid point to be "natural" (i.e. non-urban). In this study, grassland was used to parameterize the natural, non-urban surface. Each urban grid cell is then partitioned based on urban fraction (i.e., how much of a grid cell is urbanized), and surface fluxes from the LSM and SLUCM are aggregated.

To analyze the performance of the LSM-SLUCM modeling system, many investigations have made modifications to land use categories, urban fraction, vegetation percentage, and various urban canopy and LSM parameters. For example, Miao et al. (2009) used the WRF Noah LSM-SLUCM system with modified land use categories, building height, and anthropogenic heat release within the urban area. They concluded that increasing urban development intensity resulted in a warmer and drier urban environment extending to 1.8 km above ground level (AGL). In addition, their results suggested that increased building height slows nocturnal wind speeds in the lowest 1 km AGL due to increased friction, but enhances vertical mixing during the day, resulting in stronger wind speeds. Cui and de Foy (2012) found that increasing vegetative cover in an urban area moderates the UHI effect. Others, such as Li et al. (2013) and Chen et al. (2014, 2015), simulated urban expansion by changing the urban land use representation to that from various years. As urban extent and intensity increased, so did sensible heat, ground heat storage, and air temperature throughout the boundary layer. Additionally, Adachi et al. (2014) found that a compact city with the same population as a disperse one (simulated by modifying urban fraction) had a weaker average UHI, but had higher temperatures in the urban core. These findings suggest that accurate urban land cover representation is essential for accurately simulating meteorological conditions in urban areas.

1.1.3 Urban modification of convection

Atmospheric modifications by urban areas can affect storm-scale weather phenomena. Enhanced convergence on the outskirts of urban area, as a result of increased surface roughness, can result in precipitation enhancement in and near the urban area (e.g., Bornstein and Lin 2000; Thielen et al. 2000), as can UHI-induced destabilization over and downwind of cities (e.g., Shepherd et al. 2002; Shepherd and Burian 2003; Shepherd 2006; Mote et al. 2007; Baik et al. 2007). In support of these theories, recent observational studies find significant $(10-30\%)$ precipitation increases over and downwind of cities (e.g., Lacke et al. 2009; Shepherd et al. 2010a; Li et al. 2011; Ganeshan et al. 2013; Seino et al. 2016). In comparing rain gauge measurements in and around Houston, Texas, Burian et al. (2005) show that warm season rainfall increased by 25% from 1950–58 to 1984–99, suggesting that the urban effect on downwind precipitation is affected by urban size. Modeling studies (e.g., Li et al. 2011; Wang et al. 2014; Yang et al. 2014b) have suggested that this additional precipitation is a result of more (less) frequent heavy (light) rainfall events. Additionally, observational (e.g., Loose and Bornstein 1977; Bornstein and Lin 2000; Niyogi et al. 2011) and modeling (e.g., Niyogi et al. 2011; Miao et al. 2011; Yang et al. 2014b) investigations have suggested that the increased surface roughness of the urban canopy can cause a bifurcation or diversion of precipitation systems, thereby further modifying precipitation distribution.

Though most of these investigations only consider weakly-forced precipitation events in typical summertime environments, others analyze urban effects on precipitation systems that form in strongly forced, synoptically active regimes. Yang et al. (2014a) and Yeung et al. (2015) find that while *organized* thunderstorms associated with strong dynamic forcing change structure and initiate

new cells more frequently over the urban area, these storms do not split as they approach from the west, and there are negligible large-scale differences in precipitation patterns caused by urban areas. Ryu et al. (2016) found that simulated, urban-induced low-level temperature and wind field modifications in the Baltimore-Washington D.C. metropolitan area resulted in downwind precipitation enhancements from an organized thunderstorm complex, though the the interaction of these modifications with the Chesapeake bay breeze was a necessary factor. The results of these studies differ from those of studies that consider weakly forced convection, suggesting that interactions between urban areas and organized, forced convection merit further investigation.

1.2 Questions to be addressed

1.2.1 What is the most accurate urban parameterization option to use in severe weather simulations in the Plains?

While most studies find the WRF to properly reproduce many aspects of the boundary layer, some weaknesses still exist, particularly the simulation of boundary-layer winds. Zhang and Zheng (2004) and Ngan et al. (2013) find that phase and amplitude errors exist across all WRF PBL schemes throughout the depth of the PBL, both during the day and at night. In addition, results from Lee et al. (2011), Li et al. (2013), and Hu et al. (2016) depict errors in boundary layer winds in urban areas, particularly near the surface. However, there is a paucity of observational studies that investigate the modification of winds in urban areas alongside UHI effects against which to compare these modeling results (Klein 2012; Klein and Galvez 2014; Hu et al. 2016). In addition, as

many modeling investigations of the urban canopy focus on intense heat wave events with weak synoptic wind speeds (e.g., Chen et al. 2014; Takane et al. 2015), few closely examine urban modification of the wind field. Studies that do examine time periods with moderate wind speeds frequently focus on land-sea breeze processes (e.g., Chen et al. 2011; Gutiérrez et al. 2015a; Sharma et al. 2016), a phenomenon separate from the daytime low-level wind speed increase that results from radiation-induced turbulence. Chen et al. (2015), using a robust analysis of WRF-simulated 10-m wind speed modifications in a continental urban area, found that while increasing urban extent improved the accuracy of simulated winds, urban wind speeds were still too high.

Aside from documented errors in the reproduction of urban wind speeds, there are also reasons to believe that using an explicit urban parameterization scheme, such as the SLUCM, is not appropriate for all urban areas, particularly the geometric considerations of urban buildings made by explicit urban schemes. The SLUCM assumes that all urban areas are covered by street canyons (Fig. 1.1), which motivates how the scheme computes radiative terms, particularly ground shading by tall buildings and trapping of longwave radiation due to reflections off building walls. These radiative differences comprise the largest difference between urban canopy models and the bulk urban parameterizations used in the Noah LSM. While this basic model of urban areas may be relatively realistic for very large, highly urbanized cities (e.g., New York City, London, Beijing, etcl.), this kind of urban morphology is not common in largely suburban cities typical of the Great Plains (e.g., Dallas-Ft. Worth, Oklahoma City, Kansas City, etc.). Given that the ultimate goal in this dissertation is to use an urban parameterization in a Plains supercell case, the first objective will be to determine the most accurate method by which to parameterize an urban area typical of the Great Plains.

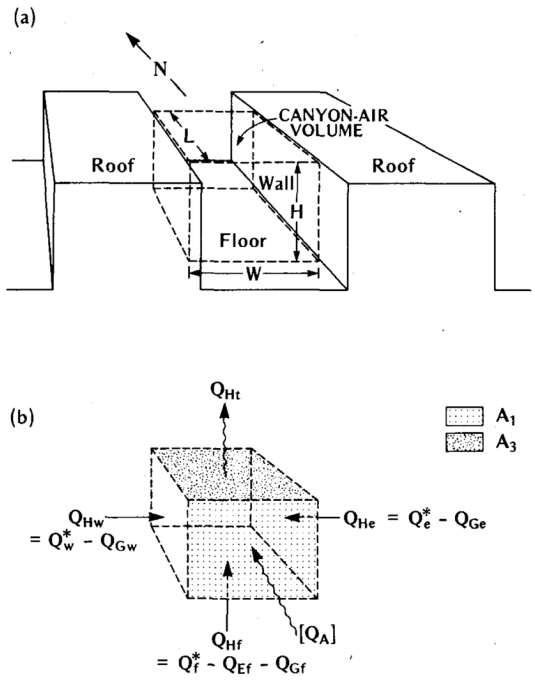

Figure 1.1: Schematic depiction of (a) the urban/atmosphere interface, including an urban canyon and its canyon air volume (dashed); and (b) sensible heat exchanges into and out of the canyon air volume. (Adapted from Nunez and Oke (1977).)

1.2.2 Does the presence of a city modify the strength and evolution of a supercell?

As yet unexplored are the effects that urban areas could have on *severe* organized convection, particularly supercells. Recent research involving supercells has focused on properties of the lowest 500 to 1000 m of the PBL, especially the role that near-surface shear properties play in low-level mesocyclone strength and tornadogenesis. Thompson and Edwards (2000) first noted a prominent low-level hodograph "kink" separating primarily near-surface speed shear from principally directional shear above in some environments of significantly tornadic supercells. Subsequent analyses of proximity soundings and modeling investigations suggest that the properties of the PBL below this "kink" (i.e., typically

below 500 m) discriminate tornadic from non-tornadic environments better than traditional deep-layer metrics used to identify environments supportive of supercells (e.g., Esterheld and Giuliano 2008; Togstad et al. 2011; Nowotarski and Jensen 2013). Using idealized simulations, Markowski et al. (2012) and Markowski and Richardson (2014) show that environmental shear in the lowest few hundred meters of the PBL is dynamically beneficial to the development of a supecell's low-level mesocyclone (Fig. 1.2). Their results suggest that stronger near-surface shear lowers the base of the mid-level mesocyclone, thereby enhancing the dynamic vertical perturbation pressure gradient force. This results in greater stretching of negatively buoyant near-surface outflow parcels that possess cyclonic vorticity (ζ), thereby strengthening the low-level mesocyclone. Examining properties even closer to the surface, it has been shown that surface friction can intensify tornadoes by preventing the development of cyclostrophic balance and thereby promoting radial convergence (e.g., Rotunno 1979; Howells et al. 1988; Lewellen 1993). Additionally, recent simulations (Schenkman et al. 2012; Xu et al. 2015) suggest that friction can also act as a *source* of vorticity in storm inflows rather than solely serving to enhance vorticity generated by other means, though Markowski and Richardson (2014) finds the contributions of frictionally-generated vorticity to be highly variant in idealized storms.

The lifting condensation level (LCL) of an environment, which approximates cloud base, is raised by warmer, drier near-surface conditions. Lower lifting condensation level heights (LCLs) are well-documented to favor tornadic supercells (e.g., Thompson et al. 2003; Craven et al. 2004). Lower LCLs tend to suppress supercell cold pools (i.e., they have small negative buoyancy through decreased evaporative cooling; Markowski et al. 2002), which Markowski and Richardson (2014) argue increases vortex stretching (less negatively buoyant parcles are easier to lift), and thus the vertical pressure gradient force, in the supercell's

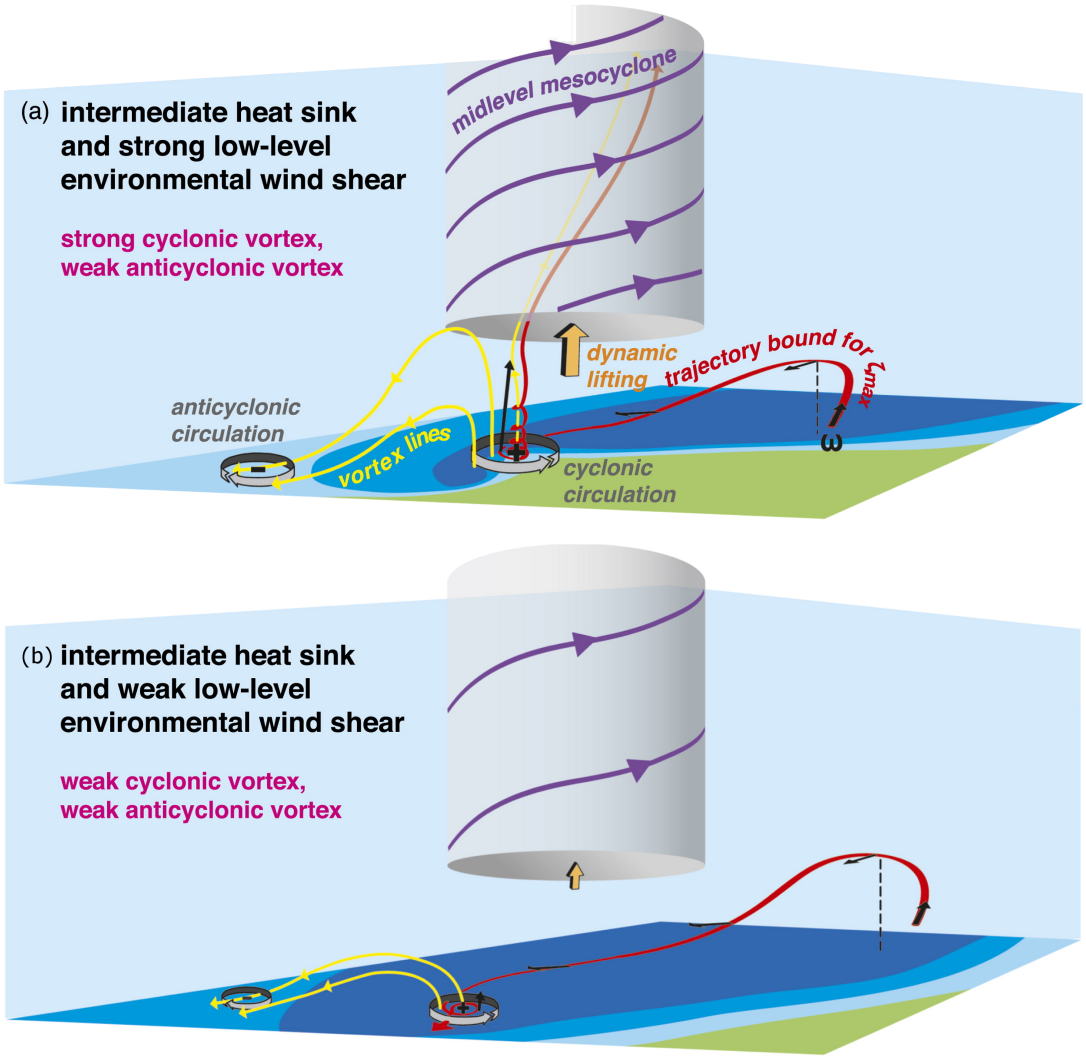

Figure 1.2: Schematic summarizing the simulation outcomes of: (a) a baseline simulation in which a strong cyclonic vortex develops and a simulation where (b) the environmental wind shear is too weak (results in a weaker dynamic vertical pressure gradient force). (Adapted from Markowski and Richardson (2014)).

low-level mesocyclone. The result is a stronger low-level mesocyclone, and thus a higher likelihood of tornadogenesis.

Given that urban areas can modify near-surface winds, temperature, and humidity, and that these properties modulate storm strength, there is the possibility that these alterations to the pre-storm (or even perhaps during-storm) environment could possibly effect the strength and evolution of a supercell. Hence,

this possibility will be investigated in this dissertation.

1.2.3 What aspect of the urban area has the largest impact on supercell characteristics?

As discussed above, the differences between urban and natural surfaces can generally be categorized as either thermodynamic properties or roughness. While each surface attribute most directly affects atmospheric properties of the same type (i.e., changes in heat capacity typically have the largest effect on temperatures), there are also cross-category effects. For example, increased surface roughness in the urban area can induce stronger turbulence, which then results in greater downward transport of cooler air (in the case of a super-adiabatic layer near the surface), resulting in lower near-surface temperatures. However, the degree to which each of the multitude of effects of surface roughness and thermodynamic properties result in atmospheric modifications is still a subject of debate. Additionally, research suggests that both the UHI and urban surface roughness can modify storm properties, particularly rainfall patterns. However, it is unclear which of these two would most affect supercellular properties and evolution. Thus, the final goal of this dissertation will be to investigate which properties of the urban area have the greatest effect on a simulated supercell, and if this relationship changes dependent on city location relative to the storm's track.

1.3 Dissertation overview

The following chapter will discuss methods and data analyses techniques that will be used in one or more chapters. Chapter 3 will present the results from testing and selection of an appropriate WRF urban parameterization, and Chap-

ter 4 will examine how a simulated urban area, parameterized using this chosen urban scheme, modifies the strength and evolution of a supercell when in various locations relative to the storm's path. A factor separation analysis of several simulations from Chapter 4 is presented in Chapter 5, and an overall summary concludes the dissertation in Chapter 6.

Chapter 2

Model modifications, analysis techniques, and observational data

2.1 Update of urban land use and urban fraction data

The default land use / land cover (LULC) arrays used by the Noah LSM are computed from (at best) 30-second Global Land Cover Characterization (GLCC) data (available from the U. S. Geological Survey; USGS), which is derived primarily from 1992-1993 Advanced Very High Resolution Radiometer (AVHRR) 10-day Normalized Difference Vegetation Index (NDVI) composites (Loveland et al. 2000). This data is categorized according to the USGS 24-category LULC system. Using these data sets results in coarse, sometimes inaccurate, representations of finer-scale land surface features that change frequently over time, such as urban areas. In addition, the USGS LULC data has only one category of urban land use. Consequently, complicated urban morphology is represented by just one urban class, such that the majority of the OKC metropolitan area is defined simply as urban.

As an accurate representation of the OKC and DFW urban areas are critical to this dissertation, LULC and urban fraction data were modified (for all but one simulation in Chapter 3) using data from the 2011 National Land Cover Database (NLCD; Homer et al. 2015). The NLCD provides a 30-m, 20-category,

4-urban-type continental United States land cover classification (LCC) derived from Landsat data. Unfortunately, the NLCD LCC data use a different classification scheme than the USGS data, and LULC data classified using the USGS categories are required by the Noah LSM. Thus, the NLCD data were re-classified to match the USGS 24-category classification system (Table 2.1), with the developed open space (DOS) and developed low-intensity (DLI) categories merged to allow for 3 urban categories.

When the SLUCM is used, its default strategy is to assign grid cell urban fraction percentage based on urban category. If the single-urban-category USGS LULC data set is used, all urban grid cells have 90% urban fractional coverage. However, when paired with NLCD LULC data with re-mapped 3 urban categories, urban fraction values of 50%, 90%, and 95% are assigned to the low-intensity residential (LIR), high-intensity residential(HIR), and commercial

Table 2.1: Specifications for how NLCD2011 data were remapped to USGS LULC categories.

NLCD 2011 Category	Reclassified USGS Category
Open Water	Water Bodies
Perrenial Ice/ Snow	Snow or Ice
Developed, Open Space	Low-Intensity Residential
Developed, Low Intensity	Low-Intensity Residential
Developed, Medium Intensity	High-Intensity Residential
Developed, High Intensity	Commercial
Barren Land	Barren or Sparsely Vegetated
Deciduous Forest	Deciduous Broadleaf Forest
Evergreen Forest	Evergreen Needleleaf Forest
Mixed Forest	Mixed Forest
Shrub/ Scrub	Shrubland
Grassland, Herbaceous	Grassland
Pasture/ Hay	Dryland Cropland and Pasture
Cultivated Crops	Irrigated Cropland and Pasture
Woody Wetlands	Wooded Weland
Emergent Herbaceous Wetlands	Herbaceous Wetland

(COM) urban LULC types, respectively. In addition, NLCD's impervious surface area (ISA; Xian et al. 2011) data is used as a direct substitute for urban fraction, such that urban fraction is no longer assigned a default value according the land use type. To arrive at the data used in the WRF, raw ISA data were median aggregated to 510-m cell sizing, then re-sampled to the same 500-m grid sizes as the LULC data using the nearest-neighbor (NN) method. The WRF uses this data to create the urban fraction array on the model grid using NN interpolation. Note that combining the DOS and DLI categories in to the USGS's LIR category tends to over-estimate the default urban fraction ($f_{urb} = 50\%$) of the grid points that were originally categorized as NLCD DOS, which is typically assigned to areas with 0% $\leq$ISA$\leq$ 20% (Homer et al. 2004; Shaffer et al. 2016).

2.2 Noah LSM modifications

In its original form, the Noah LSM uses a single land use category to represent all urban areas (e.g., a bulk urban scheme; Liu et al. 2006). In order to take advantage of the NLCD 3-category urban land use information, the Noah LSM code and parameters table were modified. The added entries from the Noah LSM's parameter table are shown in Table 2.2. Two variables from this table, Q_{GL} and α, both empirical vegetation-dependent parameters, are used to parameterize latent heating within the model through their control on canopy resistance. In the Noah LSM (Chen and Dudhia 2001), canopy resistance, r_c, is computed as

$$r_c = \frac{r_{c_{min}}}{LAI \cdot F_1 \cdot F_2 \cdot F_3 \cdot F_4} \tag{2.1}$$

where $r_{c_{min}}$ is the minimum possible canopy resistance, LAI is leaf area index, and the F_1, F_2, F_3, and F_4 factors correspond to stomatal response to insolation, vapor pressure deficit, ambient air temperature, and soil moisture, respectively.

The F_1 factor is defined as

$$F_1 = \frac{f + \left(\frac{r_{c_{min}}}{r_{c_{max}}}\right)}{1 + f} \tag{2.2}$$

with

$$f = 0.55 \frac{Q_s}{Q_{GL}} \frac{2}{LAI} \tag{2.3}$$

where $r_{c_{max}}$ is the maximum possible canopy resistance (typically set to 5000 s m^{-1}), Q_s is insolation reaching the surface, and Q_{GL} is an empirical scaling parameter assigned for each vegetation type, typically varying from 30 W m^{-2} for forests to 100 W m^{-2} for cropland (Jacquemin and Noilhan 1990). Holding all else constant, larger values of Q_{GL} typically lead to larger values of canopy resistance, hence lower evapotranspiration. In addition, the F_2 factor, which parameterizes stomatal response to vapor pressure deficit, is dependent on α as

$$F_2 = \frac{1}{1 + \alpha\big[q_s(T_a) - q_a\big]} \tag{2.4}$$

where $q_s(T_a)$ is the saturation water vapor mixing ratio of the near-surface air, q_a is the water vapor mixing ratio, and α is an empirical vegetation-dependent parameter, varying from 40 for crops, to 150 for forests and 300 for shrubland. As with Q_{GL}, larger values of α produce greater canopy resistance and less evapotranspiration.

In order to achieve very little evapotranspiration from urban areas, the Noah LSM sets Q_{GL} and α to 999 W m^{-2} and 999, respectively. These large parameter values result in very small $F1$ and $F2$ factors, thereby creating an abnormally high canopy resistance and little to no evapotranspiration. However, for cities such as OKC, where many urban locations have grassy areas and trees, this treatment of evapotranspiration is not appropriate. To allow some latent heat

flux within urban areas, Q_{GL} and α were modified to values of 150, 200 and 250 W m^{-2} and 75, 100, and 125, respectively, for LIR, HIR, and COM, respectively. These values are higher than the highest value used for any vegetation type (maximum Q_{GL} of 100 W m^{-2} for cropland and grassland and maximum α of 60.00 for wetlands), but not high enough to nearly completely shut off evapotranspiration as is achieved by the default values. In addition, these parameters were scaled below these given values in proportion to urban fraction, hence the quantities shown here indicate *maximum* values. Chosen values for Q_{GL} and α are not based on previous studies and are reasonable estimates at what parameters might provide the most realistic results in simulations. Hence, other values could possibly be used in their place and realistic results obtained.

The surface roughness values (z_o) assigned to NLCD categories developed low, medium, and high intensity (0.7 m, 1.5 m, and 2.0 m, respectively) were used as a first guess, then adjusted to better agree with OKCNET (described in Section 2.4) wind observations. This adjustment was conducted via a trial and error approach wherein different values were tested within a physically reasonable range, given the known characteristics of the land cover, until the results agreed with observations. This method is similar to that discussed in Wang et al. (2011) in which many of the parameters needed by the SLUCM are estimated and calibrated for each case. As a result, surface roughness lengths of 0.5 m, 1.0 m, and 2.0 m were used for LIR, HIR, and COM grid points, respectively (Table 2.2). As surface roughness values are typically $\sim$ 10% of the height of the average obstruction, the surface roughness values used would correspond to 5 m, 10 m, and 20 m mean building height for the three urban categories.

2.3 Computation of winds in the urban surface layer

Following Monin-Obukhov similarity theory (Monin and Obukhov 1954), and computational formulations developed by Paulson (1970), Dyer and Hicks (1970), and Zhang and Anthes (1982), the MM5 surface layer scheme used in all simulations presented here computes the effect of surface roughness on winds in the surface layer through the frictional velocity, u_*, computed as

$$u_* = \frac{k\,U}{\ln\left(\frac{z_a}{z_o}\right) - \Psi_m}, \tag{2.5}$$

where k is the Von Karman constant ($= 0.4$), U is the wind speed at the first model level, z_a is the height above ground of the first model level ($\sim$ 25 m in this dissertation), z_o is the surface roughness length, and Ψ_m is the stability correction function. The height of the first model level is required to be above 10 meters. As surface roughness increases, u_* decreases. The frictional velocity is used to directly compute the diagnostic 10-m wind speed, u_{10} and v_{10}, using the log wind profile assumption valid in the surface layer:

$$u_{10} = u_a \left[\frac{\ln\left(\frac{10}{z_o}\right) - \Psi_m(z = 10)}{\ln\left(\frac{z}{z_o}\right) - \Psi_m(z = z_a + z_o)} \right], \tag{2.6}$$

$$v_{10} = v_a \left[\frac{\ln\left(\frac{10}{z_o}\right) - \Psi_m(z = 10)}{\ln\left(\frac{z}{z_o}\right) - \Psi_m(z = z_a + z_o)} \right], \tag{2.7}$$

where u_a and v_a are the x and y components, respectively, of the wind at the first model level. While the values of u_{10} and v_{10} are not used in any further computations in the WRF, they are frequently used in studies to compare to observed wind speeds, which are traditionally measured at 10 m AGL.

Computation of the stability correction function, Ψ_m is dependent on surface layer stability. As the results presented here generally focus on properties of the atmosphere during the day under warm, high insolation conditions, this discussion of the wind profile function will only consider unstable (i.e., super adiabatic) surface layer computation. In an unstable surface layer (as determined by the bulk Richardson number, $Ri < 0.0$), the MM5 scheme computes Ψ_m according to modified Dyer and Hicks (1970) parameterization (Fairall et al. 1996; Grachev et al. 2000; Jiménez et al. 2012) as

$$\Psi_m = \frac{\Psi_{Km}\left(\frac{zz}{L}\right) + \left(\frac{z}{L}\right)^2 \Psi_{Cm}\left(\frac{zz}{L}\right)}{1 + \left(\frac{zz}{L}\right)^2}, \tag{2.8}$$

where $zz = z_a + z_o$ and L is the Monin-Obukhov length. The functions Ψ_{Km} and Ψ_{Cm} are computed as

$$\Psi_{Km}\left(\frac{zz}{L}\right) = 2\ln\left(\frac{1+x}{2}\right) + \ln\left(\frac{1+x^2}{2}\right) - 2\arctan x + \frac{\pi}{2} \tag{2.9}$$

and

$$\Psi_{Cm}\left(\frac{zz}{L}\right) = \frac{3}{2}\ln\left(y^2 + y + \frac{1}{3}\right) - \sqrt{3}\arctan\left(2y + \frac{1}{\sqrt{3}}\right) + \frac{\pi}{\sqrt{3}}, \tag{2.10}$$

with

$$x = \left(1 - 16\frac{zz}{L}\right)^{1/4} \tag{2.11}$$

and

$$y = \sqrt[3]{1 - 10\left(\frac{zz}{L}\right)}. \tag{2.12}$$

After the MM5 computes these parameters at any one model time step, the SLUCM (if used) then computes an urban frictional velocity, $u_{*_{urb}}$, as well as an urban stability correction function, $\Psi_{m_{urb}}$. The SLUCM computes urban

frictional velocity as

$$u_{*_{urb}} = \sqrt{\Phi_{uv}}. \tag{2.13}$$

Φ_{uv}, which is only used to compute $u_{*_{urb}}$, is computed as

$$\Phi_{uv} = (f_R\, C_{DR} + f_{NR}\, C_{DC})\; U^2, \tag{2.14}$$

where f_R and f_NR are the fraction of the grid cell that are road and non-road ($f_R + f_{NR} = 1$), respectively, and C_{DR} and C_{DC} are momentum diffusion coefficients associated with the road and non-road portions of the grid cell, respectively. Urban and non-urban frictional velocities computed by the MM5 surface layer parameterization and the SLUCM, respectively, are aggregated based on grid cell urban fraction to create an updated frictional velocity,$u_{*_{pbl}}$, according to

$$u_{*_{pbl}} = f_{urb}\, u_{*_{urb}} + (1 - f_{urb})\, u_*, \tag{2.15}$$

which is then passed on to the YSU PBL scheme and used to compute the winds at each grid point in the boundary layer starting at the lowest model grid cell. The urban stability function correction, $\Psi_{m_{urb}}$, is computed using the equation for Ψ_{Km} ((2.9)), but with x computed using urban values for $^z/_L$ as

$$\frac{z}{L} = -\frac{k\, g\; (z_a - d)\; \Phi_h}{u_{*_{urb}}\, T_a} \tag{2.16}$$

where T_a is the temperature at the first model level, d is the zero-plane displacement height, is the gravitational constant, and Φ_h is heat transfer (i.e., heat flux normalized by density and heat capacity). When the SLUCM is used, $\Psi_{m_{urb}}$ completely replaces Ψ_m computed previously by the MM5 surface layer scheme, which is then used in the PBL scheme . It is also used to compute a new diagnostic 10-m wind speed (with $\Psi_{m_{urb}}$ and $z_{o_{urb}}$ used in place of Ψ_m and

z_o, respectively, in (2.6) and (2.7)) which also overrides the quantities computed by the surface layer scheme.

The YSU PBL scheme uses $u_{*_{pbl}}$ and $\Psi_{m_{urb}}$ in computation of wind speeds on model grid points in the PBL. The frictional velocity is used to compute momentum eddy diffusivity, K_m, as

$$K_m(z) = k w_s z \left(1 - \frac{z}{h}\right), \tag{2.17}$$

where h is the height of the boundary layer, and w_s is the mixed layer velocity scale. The mixed layer velocity scale is computed as

$$w_s = u_* \phi_m^{-1}, \tag{2.18}$$

where ϕ_m is the Monin-Obukhov similarity function for momentum evaluated at the top of the surface layer. Under unstable surface layer conditions, ϕ_m is computed in the PBL scheme according to Dyer and Hicks (1970) as

$$\phi_m \left(\frac{h}{L}\right) = \left(1 - 16\frac{h}{L}\right)^{-1/4}, \tag{2.19}$$

where h is the height of the PBL top. The fraction h/L is computed using $\Psi_{m_{urb}}$ as

$$\frac{h}{L} = 0.1 \frac{Ri\, \Psi_{m_{urb}}^2\, h}{z\, \Psi_{h_{urb}}}, \tag{2.20}$$

where Ri is the bulk Richardson number in the surface layer and $\Psi_{h_{urb}}$ is the stability correction for heat transfer.

2.4 Observational data

For verification purposes in Chapter 3, two sets of surface observations are used. Oklahoma City Micronet (OKCNET; Basara et al. 2011) data are obtained for comparisons to model results within the OKC urban area (Fig. 2.1). The OKC-

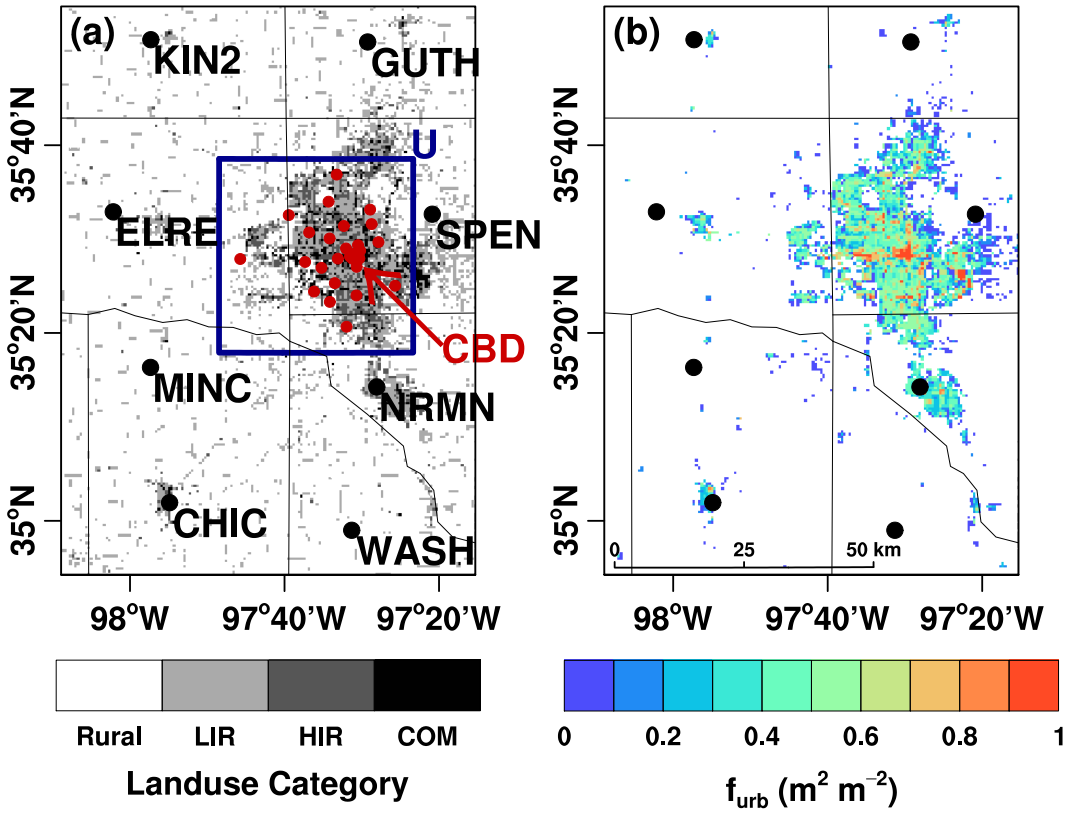

Figure 2.1: (a) For the Oklahoma City region, background shading corresponding to rural ares (white), as well as land use categories LIR (low-intensity residential), HIR (high-intensity residential) and COM (commercial) derived from NLCD 2011 data. Red dots are locations of OKCNET stations, with the central business district (CBD) labeled in red. Not all station locations are visible in the CBD due to symbol overlap. Black dots and labels are the 8 Oklahoma Mesonet locations surrounding OKC. Urban points (land use = LIR, HIR, or COM) inside the blue box labeled "U" are used as urban grid points in WRF analyses, while all rural points not contained within box U, but within box R, are considered rural areas. (b) Color-filled contours are urban fraction (f_{urb}, m^2 m^{-2}), also derived from NLCD 2011 data. Black dots are rural Mesonet sites.

NET, which was designed to improve atmospheric monitoring throughout the OKC metropolitan area, consisted of 39 stations, spaced approximately 3 km apart, with 36 traffic-signal-mounted (9 m AGL) stations and 3 stations sited according to Oklahoma Mesonet (Brock et al. 1995; McPherson et al. 2007) standards. These observations are available at 1-minute-averaged intervals from November 2008 through November 2010. Oklahoma Mesonet data are used as a rural counterpart to OKCNET observations. The Oklahoma Mesonet, a rural network of 120 meteorological stations with citing chosen so as to minimize influences from urban landscapes, provides a continuous data set of 5-minute averages of 2-m and 9-m temperature, 2-m relative humidity, as well as 10-m wind speed and direction from across Oklahoma (Brock et al. 1995).

Spatial comparison of observed data to model-derived quantities is desired, so point measurements at OKCNET and Oklahoma Mesonet sites are interpolated to a regular grid using the ordinary kriging method of Journel and Huijbrgts (2004). Kriging is a technique commonly used in mapping point-observations of meteorological, geological, and chemical quantities to continuous two-dimensional fields (Moore and Rojstaczer 2002; Alfieri et al. 2009; Mercer et al. 2011; Smoliak et al. 2015; Gutiérrez et al. 2015a; Hu et al. 2016). While kriging interpolation is a statistical method subject to errors based on user-defined interpolation options, and may change significantly if various data points are removed, it maintains observational integrity at the observed locations. The purpose here is only to provide a two-dimensional field of observations against which to visually compare model results, and to supplement point-to-point analyses of model biases. Hence, though kriging analyses are subject to errors, they are not of much concern here as the analyses presented here will not include a statistical comparison of the field of kriged observations to model results.

2.5 Heirarchical clustering algorithm

Groups of model simulations are used in this study to make the resulting analyses more robust and less susceptible to noise that necessarily arises due to small-scaled artifacts. While the various members could be grouped subjectively or based upon various characteristics, there is no guarantee that clustering the simulations in this manner yields groups whose members are most similar to each other. Hence, we perform hierarchical clustering analysis (HCA; Anderberg 1973; Alhamed et al. 2002) using selected variables to determine which simulations should be grouped together. HCA can help identify potentially important relationships in highly complex datasets that could easily be overlooked otherwise, requires no a priori assumptions about how many clusters exist, and allows clusters and their secondary subclusters to be identified simultaneously (Wilks 2011). These qualities make HCA an ideal choice for the present study, and it has been used previously to draw insight from ensemble simulations (e.g., Yussouf et al. 2004; Nakaegawa and Kanamitsu 2006; Branković et al. 2008; Johnson et al. 2011b)

Let $\mathbf{X} = [x_{ij}]$, $1 \leq i \leq m$, $1 \leq j \leq n$, be the *data* matrix, where each jth column represents an *object* (in this case, a simulation member), and each ith row represents an *observation* (a grid point in the horizontal plane). Hence, for the following analyses, $\mathbf{X} \in \mathbb{R}^{248{,}004 \times 108}$, and $x_{\star j}$ denotes the jth object / simulation member across all m observations, and $x_{i\star}$ denotes the ith observation across all n objects / simulation members.

HCA uses either similarity or dissimilarity measures to quantify the distance between objects. The pairwise distances between all objects are calculated and arranged in the form of a square, $n \times n$, matrix where the ij^{th} entry denotes the distance between objects i and j, and n is the number of objects. For

this study, the commonly-employed Euclidean distance dissimilarity measure is selected for use, as tests using other similarity/dissimilarity measures (e.g. correlation) produced results similar to those presented herein using Euclidian distance. The Euclidean distance, e_{ij}, between two objects, i and j, is defined as:

$$e_{ij} = \sqrt{\sum_{k=1}^{m} (x_{ki} - x_{kj})^2} \geq 0, \tag{2.21}$$

where m is the number of observations in each object, or in this case the total number of grid points in the horizontal plane (248,004). A unique $n \times n$ dissimilarity matrix, $\mathbf{E}$, formed by the pairwise Euclidean distances, is computed for each 5-min model output time during the storm's life cycle (2130–0300 UTC, or 64 Δt). Each matrix $\mathbf{E}$ is normalized to form a new normalized distance matrix, $\mathbf{D}$, whose elements are computed as

$$0 \leq d_{ij} = \frac{e_{ij} - e_{min}}{e_{max} - e_{min}} \leq 1, \tag{2.22}$$

where e_{min} and e_{max} are the minimum and maximum distances, respectively, of the original distance matrix $\mathbf{E}$. All unique normalized matrix elements d_{ij} are averaged over all times, and the resulting is used as a composite distance measure. The resulting matrix $\overline{\mathbf{D}}$ is then used for HCA using Ward's algorithm (Ward 1963; Murtagh and Legendre 2014). This procedure is similar to that used by Johnson et al. (2011a) to perform HCA on ensemble precipitation forecasts.

The results of hierarchical clustering are displayed graphically as a dendrogram, which shows a stepwise merging of the various clusters identified by the algorithm. Each simulation is initially a single-member group displayed along the bottom. Each single-element group is then merged with the next most similar member. The vertical height of each merger, represented by a horizontal

line connecting the two groups, indicates the increase in within-group variance caused by the combination. This process of merging the most similar groups is repeated until all groups are combined. Thus, lower-level clusters are composed of simulation members that are more similar to each other than those merged near the top.

In Chapter 4, HCA will be performed on several different variables indicative of storm structure and strength one variable at the time (i.e., $\mathbf{X}$ will be a horizontal field of a single variable). As many studies have found urban areas to affect rainfall patterns, accumulated rainfall will be analyzed with HCA to determine the statistical correlation between city location and accumulated rainfall over time. To analyze how varying city location modifies mid-level storm strength, HCA will be used on 2–5-km updraft helicity (UH; Kain et al. 2008) and column-maximum updraft velocity. UH, computed as

$$UH = \int_{z_o}^{z_t} w\zeta dz, \tag{2.23}$$

where z_o and z_t are the height above ground level (AGL) of the bottom and top, respectively, of layer over which UH is to be computed, w is vertical velocity, and ζ is vertical vorticity, quantifies the rotational strength of a storm over the layer in question, and thus is indicative of mesocyclone location. UH computed over the standard 2–5-km layer indicates mid-level rotation in a storm. However, UH can also be computed over a layer closer to the ground, for example 0–1-km, to location strong low-level storm rotation. Hence, HCA will also be performed using 0–1-km UH to determine the effect of city location on low-level storm strength. To analyze the effect of urban location on storm properties very near the surface, HCA will also be performed on first-model-level minimum temperature (quantifies cold pool strength), maximum wind speed (analyzes

outflow and inflow strength and patterns), and vertical vorticity.

2.6 Calculation of group difference fields

Once meaningful groups of ensemble members are computed using HCA, we quantify differences between members of two groups to investigate group differences over a specific time interval. For each variable (except storm-total rainfall), the field presented, $\overline{\mathbf{Y}}$, is computed as

$$\overline{\mathbf{Y}}(x,y) = \frac{1}{\ell}\sum_{i=1}^{\ell} \max_{1\leq t\leq nt} \mathbf{A}_i\,(x,y,t) - \frac{1}{p}\sum_{j=1}^{p} \max_{1\leq t\leq nt} \mathbf{B}_j\,(x,y,t)\,, \tag{2.24}$$

where $\mathbf{A}_i$ is the i^{th} HCA member in a group with ℓ members, $\mathbf{B}_j$ is the j^{th} member of either another HCA grouping (or the control group with no urban areas) with p members, and t is time with nt time steps spanning the time interval of interest. For temperature, min is used in place of max to investigate surface cold pool strength. These fields represent the difference between group-averaged, time-maximum values at each grid point of two groups. Because storm-total rainfall is already a cumulative quantity, the computation for its field is simply a difference between point-to-point group averages of the run-total accumulated rainfall, computed as

$$\overline{\mathbf{Y}}(x,y) = \frac{1}{\ell}\sum_{i=1}^{\ell} \mathbf{A}_i\,(x,y) - \frac{1}{p}\sum_{j=1}^{p} \mathbf{B}_j\,(x,y)\,. \tag{2.25}$$

This same procedure also will be used to compare parameter fields in the factor separation analysis.

2.7 Significance testing

To test the significance of group difference fields, permutation tests for the difference of group means (Pitman 1937) were conducted. This non-parametric permutation test assesses the significance of the difference between the means of two samples (groups) without any assumptions about the distributions of the sampled population. The significance of the test statistic, p, represents the probability that the difference between the means of the two groups could arise by pure chance.

For each pair of groups we wish to compare, group differences fields, $\overline{\mathbf{Y}}$, are computed as described in Section 2.6. We also retain the time-composite fields for each i^{th} urban group member, $\mathbf{U}_i$, and each j^{th} non-urban group member, $\mathbf{C}_j$, computed as

$$\mathbf{U}_i\left(x,y\right) = \max_{1\leq t\leq nt} \mathbf{A}_i\left(x,y,t\right) \tag{2.26}$$

$$\mathbf{C}_i\left(x,y\right) = \max_{1\leq t\leq nt} \mathbf{B}_i\left(x,y,t\right) \tag{2.27}$$

where $\mathbf{A}_i$ is the i^{th} HCA member in a group with ℓ members, $\mathbf{B}_j$ is the j^{th} member of the non-urban simulation group with p members, and t is time with nt time steps spanning the selected time interval. As described in Section 2.6, this procedure is slightly modified for computing composite minimum temperature (use min in place of max) and storm total rainfall (there's no need for a composite as it is accumulated). For each permutation in the testing procedure, ℓ members in the set $(\mathbf{U},\mathbf{C})$ are randomly chosen to represent the urban group and placed in the permuted urban group, $\mathbf{Up}$, and the remaining members of $(\mathbf{U},\mathbf{C})$ are assigned to the permuted non-urban group, $\mathbf{Cp}$. Differences, $\overline{\mathbf{Dp}}$ between the

permuted groups are computed as

$$\overline{\mathbf{Dp}}\,(x,y) = \frac{1}{\ell}\sum_{i=0}^{\ell}\mathbf{Up}_i\,(x,y) - \frac{1}{p}\sum_{j=0}^{p}\mathbf{Cp}_j\,(x,y)\,. \tag{2.28}$$

This permutation procedure is iterated 10,000 times, providing 10,000 unique $\overline{\mathbf{Dp}}$. At each point (x, y), the fraction, p, of $\overline{\mathbf{Dp}}\,(x,y)$ that exceed (in magnitude) the original $\overline{\mathbf{Y}}(x,y)$ are determined, and p is the test statistic we use for our significance test. A significance level of $\alpha = 0.05$ is used in all calculations.

2.8 Factor separation procedure

Factor separation has been found to provide useful interpretation of various simulated weather phenomena, including climate sensitivities (e.g., Yin and Berger 2012), heavy rain in the Washington D.C. area (Ryu et al. 2016), precipitation distribution over the Atlantic (Siongco et al. 2017), and land-surface-aerosol interactions in tropical sea breezes (Grant and van den Heever 2014). In Chapter 5, factor separation will be used in a novel manner to determine the relative contributions of urban surface roughness and thermal properties to changes in simulated supercell morphology and strength.

In each simulation in Chapter 5, the parameterization of the urban area (i.e., which aspects of the urban area are included) is controlled by modifying the vegetation parameter values used by the Noah LSM (Table 2.3). In the non-urban simulations (f_0), all areas are parameterized as grassland, and in the original simulations (f_{RT}), the full suite of urban characteristics are used. To simulate an urban area that is only warm and dry (f_T), urban surface roughness, as parameterized by roughness length (z_0), is changed to be equal to that of grassland. Likewise, to incorporate a city that is only a roughness element (f_R) all parameters *other* than roughness length are changed to match those of

grassland.

To determine the contributions to storm modifications of urban roughness ($\hat{f_R}$), urban thermal characteristics ($\hat{f_T}$), and the interactions between thermal and roughness characteristics ($\hat{f_{RT}}$) compared to the storm morphology characteristics that are unrelated to any urban properties ($\hat{f_0}$), the method of Stein and Alpert (1993) is followed. The contributions of the four factors are computed as

$$\hat{f}_0 = f_0 \tag{2.29}$$

$$\hat{f}_R = f_R - f_0 \tag{2.30}$$

$$\hat{f}_T = f_T - f_0 \tag{2.31}$$

$$\hat{f}_{RT} = f_{RT} - (f_R + f_T) + f_0. \tag{2.32}$$

These differences may be computed point-to-point, which provides a horizontal field of differences, or calculated as the difference between two time series. For the former, the group difference computational procedure described in Section 2.6 is followed.

Table 2.2: Modified Noah LSM parameter table entries for the three categories of urban land use. $SHDFAC$ is fractional areal coverage of green vegetation, $NROOT$ is number of root layers, RS is minimum stomatal resistance, Q_{GL} and α are scaling factors which modulate evapotranspiration in response to insolation and vapor pressure deficit, respectively, SN_{up} is the threshold snow depth which implies 100% snow coverage, $MAXALB$ LAI_{min}/LAI_{max}, $EMISS_{min}/EMISS_{max}$, $\alpha_{min}/\alpha_{max}$ and $Z_{0_{min}}/Z_{0_{max}}$ are mimimum and maximum values of leaf area index, emissivity, albedo, and surface roughness, respectively, and Z_{topv}/Z_{botv} are the heights of the top and bottom of the canopy.

Landuse	$SHDFAC$	$NROOT$	RS	Q_{GL}	α	SN_{up}	LAI_{min}	LAI_{max}	$EMISS_{min}$	$EMISS_{max}$	α_{min}	α_{max}	$Z_{0_{min}}$	$Z_{0_{max}}$	Z_{topv}	Z_{botv}
Urban	0.10	1	200	999	999	0.04	1.00	1.00	0.880	0.880	0.15	0.15	1.0 0	1.00	0.00	0.00
Low-Int. Res.	0.27	1	75	150	100	0.04	1.00	1.00	0.880	0.880	0.20	0.20	0.70	0.70	0.00	0.00
High-Int. Res	0.02	1	100	175	150	0.04	1.00	1.00	0.880	0.880	0.20	0.20	1.50	1.50	0.00	0.00
Commercial	0.11	1	200	200	200	0.04	1.00	1.00	0.880	0.880	0.20	0.20	2.00	2.00	0.00	0.00

Table 2.3: Modified Noah LSM parameter table entries for the three categories of urban land use for each factor separation simulation category in Chapter 5. Parameter names are the same as in Table 2.2.

		Parameter Name															
Simulation	Land use cat.	$SHDFAC$	$NROOT$	RS	Q_{GL}	α	SN_{up}	LAI_{min}	LAI_{max}	$EMISS_{min}$	$EMISS_{max}$	α_{min}	α_{max}	$Z_{0_{min}}$	$Z_{0_{max}}$	Z_{topv}	Z_{botv}
CTRLE	Grassland	0.8	3	40	100	36.25	0.04	0.52	2.90	0.920	0.960	0.19	0.23	0.10	0.12	0.50	0.01
ORIG	Low-Int. Res.	0.27	1	75	150	100	0.04	1.00	1.00	0.880	0.880	0.20	0.20	0.50	0.50	0.00	0.00
	High-Int. Res.	0.02	1	100	175	150	0.04	1.00	1.00	0.880	0.880	0.20	0.20	1.00	1.00	0.00	0.00
	Commercial	0.11	1	200	200	200	0.04	1.00	1.00	0.880	0.880	0.20	0.20	2.00	2.00	0.00	0.00
DFW.W.R	Low-Int. Res.	0.8	3	40	100	36.25	0.04	0.52	2.90	0.920	0.960	0.19	0.23	0.50	0.50	0.50	0.01
&	High-Int. Res.	0.8	3	40	100	36.25	0.04	0.52	2.90	0.920	0.960	0.19	0.23	1.00	1.00	0.50	0.01
DFW.E.R	Commercial	0.8	3	40	100	36.25	0.04	0.52	2.90	0.920	0.960	0.19	0.23	2.00	2.00	0.50	0.01
DFW.W.T	Low-Int. Res.	0.27	1	75	150	100	0.04	1.00	1.00	0.880	0.880	0.20	0.20	0.10	0.12	0.00	0.00
&	High-Int. Res.	0.02	1	100	175	150	0.04	1.00	1.00	0.880	0.880	0.20	0.20	0.10	0.12	0.00	0.00
DFW.E.T	Commercial	0.11	1	200	200	200	0.04	1.00	1.00	0.880	0.880	0.20	0.20	0.10	0.12	0.00	0.00

Chapter 3

Sensitivity of simulated urban-atmosphere interactions in Oklahoma City to urban parameterization

Before approaching the main objective of simulating a supercell interacting with an urban area, it is important to ensure that the urban parameterization that is used represents urban-atmosphere interactions appropriately. To achieve this, WRF results using various urban parameterization options will be compared to observations, and the highest-performing parameterization will be used for the supercell simulations. This chapter will present the results from these simulations and make the argument that using a modified version of the Noah LSM to parameterize Plains urban areas provides the most accurate results. This chapter was taken in large part from Reames and Stensrud (2017), which is currently in press.

3.1 Data and chapter-specific methods

3.1.1 Study area and Synoptic Background

Oklahoma City (OKC), Oklahoma (35°28'56"N, 97°32'06"W) is located in central Oklahoma in the Sandstone Hills region of Oklahoma, which is characterized by 75–120-m tall rolling hills, and sits on the North Canadian River. The

metropolitan area, however, is quite flat (Fig. 3.1). OKC has a humid subtropical climate, with daily mean temperatures ranging from to 4^oC in January to 29^oC in July, and an average of 912 mm of annual precipitation. The average prevailing wind in May is from the SSE at 3.5 m s $^{-1}$. OKC ranks as the 7th largest city in the United States by land area ($\sim$ 1610 km^2), and, as of 2010, 27th largest by population ($\sim$ 580,000; United States Census Bureau 2010). While it has a small central business district ($\sim$27 km^2; Burian et al. 2005) with a number of buildings with more than 20 stories ($>$ 60 m), the majority of OKC is a mixture of suburban homes with $1-3$ story ($3-10$ m) commercial buildings along the major arterial roadways.

The time period chosen for this study, from 1–7 May 2010, was selected because it is characterized by conditions typical of mid-spring in central Oklahoma, it occurs just prior to the 10 May 2010 severe weather outbreak in central Oklahoma, and because it resides within the time period during which Hu et al. (2016) analyzed observations from the Oklahoma City (OKC) Micronet (OKC-

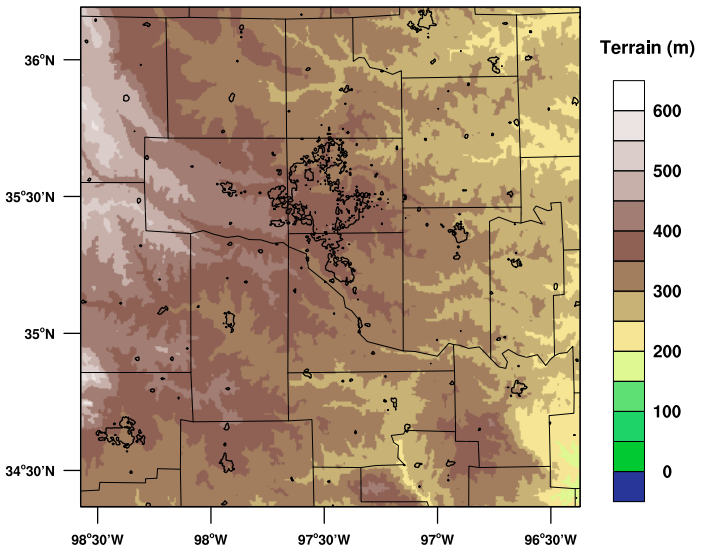

Figure 3.1: Shaded terrain height and urban areas outlined in black over the study domain. Oklahoma county borders are in gray.

NET; Basara et al. 2011). One goal of this research is to select an urban parameterization that is appropriate for use in a severe weather simulation, hence the proximity of the study's time period to the 10 May 2010 outbreak is ideal. This week at the beginning of May was characterized by a 500 mb trough over the mountain west (Fig. 3.2), as well as minimal cloud cover, very little rain, high temperatures between 20 and 35^{o}C, and moderate wind speeds in the OKC area (Fig. 3.3). An UHI was present during each day of this seven-day period(Fig. 3.3a), and rural wind speeds were consistently stronger than urban wind speeds at similar times (Fig. 3.3b).

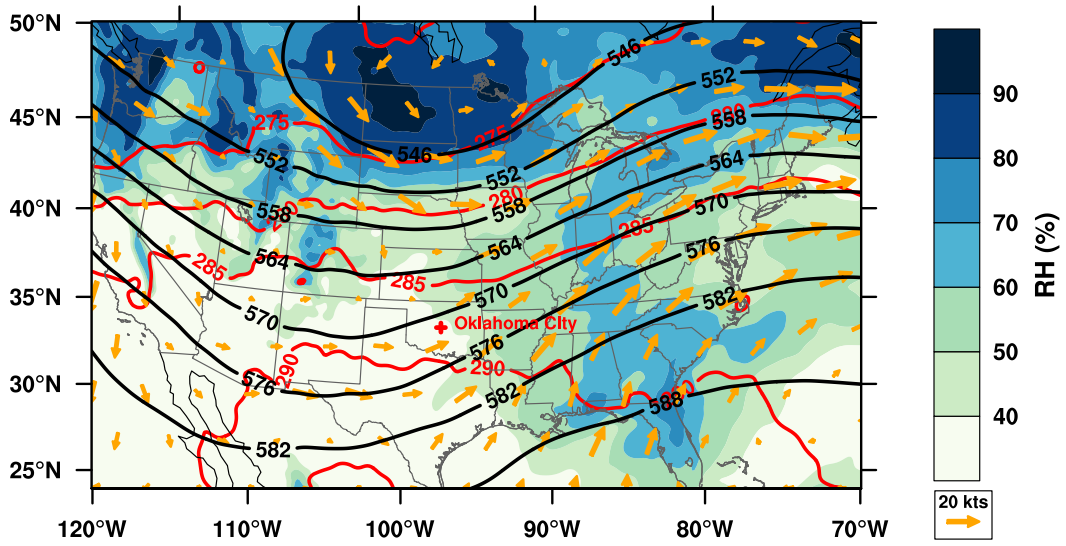

Figure 3.2: Geopotential height at 500 hPa (black lines, 10 gpm), 850 hPa relative humidity (shaded, %), 850 hPa temperature (red lines, K), and 850 hPa wind vectors (orange, kts) averaged over the investigation period. State and geopolitical borders are in gray. The red + indicates the location of Oklahoma City.

3.1.2 Model configuration

The simulations for this study were performed using the ARW-WRF model Version 3.6.1. Three one-way nested domains with grid spacing of 4.5 km, 1.5

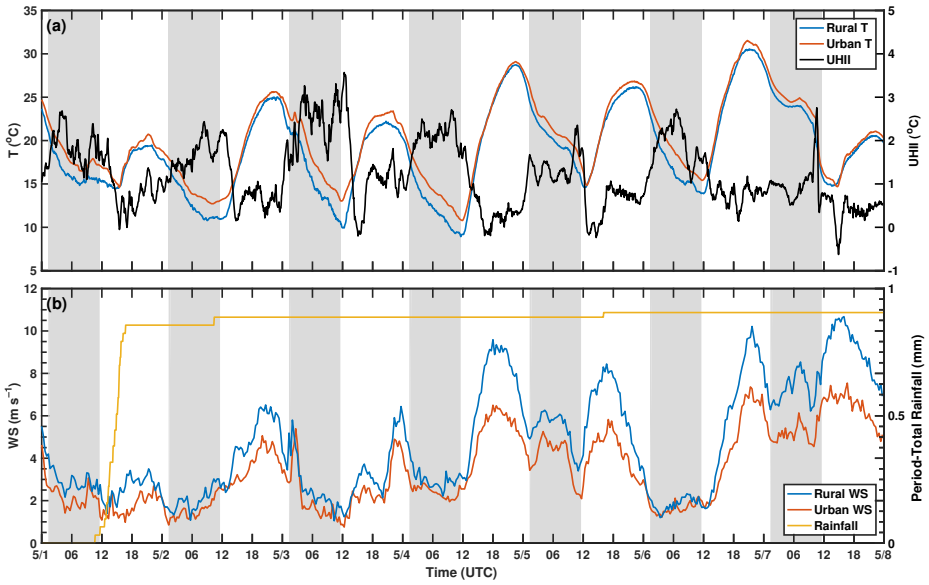

Figure 3.3: Time series of averaged observed (a) Mesonet (rural; blue) and OKCNET (urban; red) temperature, and the difference between them (black) and (b) Mesonet (blue) and OKCNET (red) wind speed and Mesonet rainfall (orange) over the duration of the study period. The times between sunset and sunrise are shaded in gray.

km and 0.5 km on grids of size 300 x 300, 400 x 400, and 399 x 399, respectively, were used (Fig. 3.4a). Each domain had 119 terrain-following vertical levels from the surface to 100-hPa ($\sim$ 16 km), with vertical spacing of $\sim$ 50 m from the surface to 800 hPa ($\sim$ 2 km) and $\sim$ 150 m above that. Approximately 20 of these levels were below 1 km, providing fine vertical resolution in the PBL.

Identical physics schemes were used across all domains, including the double-moment, six-class, graupel particle density predicting NSSL microphysics scheme (Mansell et al. 2010), the Goddard short and long wave radiation schemes (Chou and Suarez 1999; Chou et al. 2001; Matsui and Tao 2007), the Yonsei University (YSU) PBL scheme, (Noh et al. 2003), the MM5 Monin-Obukhov surface layer scheme (Monin and Obukhov 1954; Paulson 1970; Dyer and Hicks 1970; Webb 1970), and the Noah LSM. The YSU PBL scheme was chosen because it reproduces PBL moisture and temperature profiles accurately in warm, moist, severe

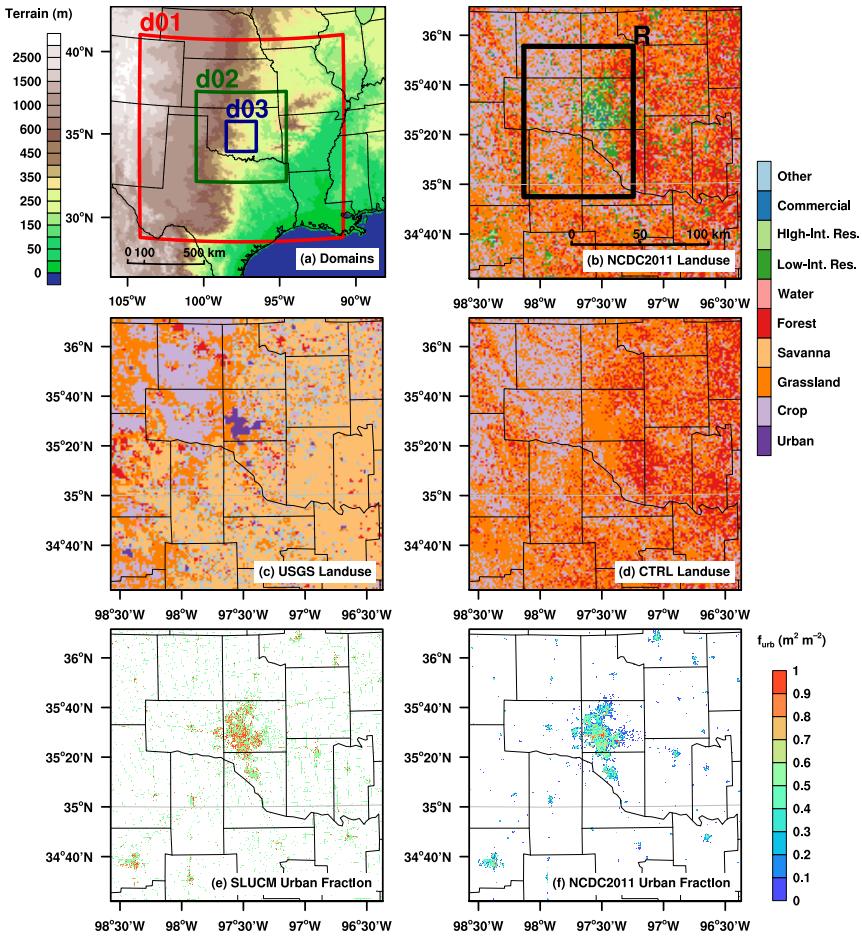

Figure 3.4: (a) Domain locations for all WRF simulations in Chapter 3, d01, d02, and d03, with 4500m, 1500m, and 500m horizontal grid spacing. State and geopolitical boundaries are drawn in black. (b) Color-filled land use/land cover of d03 from the re-mapped NLCD 2011 datasets, which which was used in LSM, SLUCM1, and SLUCM2. Oklahoma county boundaries are outlined in black. Box R encompasses the region used for "rural" calculations. (c) Color-filled land use/land cover of the original 24-category USGS. (d) Shaded land use map with all urban areas replaced by natural vegetation, as used in CTRL. (e) The original d03 SLUCM-prescribed urban fraction used for SLUCM1. (f) Urban fraction derived from NLCD 2011 impervious surface data, used for LSM and SLUCM2.

weather environments (Coniglio et al. 2013; Clark et al. 2015) in addition to its ability to simulate surface energy balance terms in rural and urban areas well (Shaffer et al. 2015). In 2 of the 4 simulations, noted SLUCM1 and SLUCM2 (Table 3.1), the single-layer urban canopy model was employed to simulate the

Table 3.1: Parameterization details for the different WRF model simulations performed in Chapter 3.

Run name	LSM code version	Urban parameterization	LULC source	Urban fraction source
CTRL	Original	N/A	NLCD2011	N/A
LSM	Original	LSM bulk	USGS	N/A
LSMMOD	Modified	LSM bulk	NLCD2011	NLCD2011 impervious surface %
SLUCM1	Original	SLUCM	NLCD2011	SLUCM default by LULC category
SLUCM2	Original	SLUCM	NLCD2011	NLCD2011 impervious surface %

effects of urban land use. The SLUCM default values for heat capacity, conductivity, albedo, emissivity, and roughness lengths for heat and momentum of roof, road, and wall surfaces (Loridan and Grimmond 2012) were employed. Anthropogenic heating in OKC, estimated at < 5 W m^{-2} in the summer by Sailor et al. (2015), was set to zero for all SLUCM simulations. Additionally, observations indicate that soil moisture was at normal levels in early May 2010, so although irrigation in urban areas is not explicitly parameterized in the present model configuration, it would likely not play a large role, if any, in modifying observations.

Each WRF simulation was initialized at 0000 UTC on 1 May 2010 (1800 CST 30 April 2010), and was integrated for 168-h until 0000 UTC 8 May 2010 (1800 CST 7 May 2010). Initial and lateral atmospheric boundary conditions were taken from the 13-km Rapid Update Cycle (RUC; Benjamin et al. 2004) at 1-h intervals. Soil state variables were initialized with offline North American Land Data Assimilation-2 (NLDAS-2) 0.125-degree Noah Model output (Xia et al. 2012), provided by the Goddard Earth Sciences Data and Information Services Center (GES DISC).

3.1.3 Numerical experiments

Five numerical simulations were performed for this study: CTRL, LSM, LSMMOD, SLUCM1, and SLUCM2 (Table 3.1). In CTRL, the modified land cover data (Fig. 3.4b) were used, but with all representations of urban areas in d03 replaced with grassland, cropland, or forest, depending on surrounding rural vegetation types (Fig. 3.4d). This model run will serve as a basis for how the WRF performs without any urban areas. Simulation LSM used the original Noah LSM bulk-urban code with the default USGS 30-second LULC data (Fig. 3.4c), while LSMMOD used the modified land use information (Fig. 3.4b) with the modified Noah LSM (Section 2.2), thus having three urban categories but still using a bulk representation of urban areas. The SLUCM1 and SLUCM2 runs employed the SLUCM scheme, but SLUCM1 used the default urban fraction values (Fig. 3.4e), while SLUCM2 ingested NLCD impervious surface data as a proxy for urban fraction (Fig. 3.4f). These latter three simulations will be compared against each other, to the CTRL run, as well as against observations to evaluate their ability to properly reproduce the effects of urban areas on their surroundings.

3.2 Results

3.2.1 Model Verification

We can evaluate general WRF performance by comparing mean biases (MB) and RMSEs for near-surface conditions of all 5 simulations at Mesonet (Table 3.2) and OKCNET (Table 3.3) locations, as well as time series of diurnal average model differences from observations (Fig. 3.5). Modeled rural conditions are too warm during the day and even more so at night (Table 3.2 and Fig. 3.5a), a

Table 3.2: Statistical comparison of the observed 10-m and simulated first-model-level rural (Mesonet locations) temperatures (T_{low}, ^{o}C), mixing ratios (q_{low}, g kg^{-1}), and wind speeds (WS_{low},m s^{-1}) at night ($0400-1100$ UTC) and during the day ($1500-2300$ UTC).

Rural Stations		T_{low} (^{o}C)			q_{low} (g kg^{-1})			WS_{low} (m s^{-1})		
		Mean	MB	RMSE	Mean	MB	RMSE	Mean	MB	RMSE
OBS	Night	15.9	–	–	7.82	–	–	2.94	–	–
	Day	21.9	–	–	7.44	–	–	6.30	–	–
CTRL	Night	16.5	1.22	3.12	6.16	-1.66	2.13	3.83	0.89	2.12
	Day	24.1	0.10	1.85	7.02	-0.43	1.23	6.18	-0.10	2.17
LSM	Night	16.6	1.29	3.16	5.98	–1.85	2.26	3.84	0.90	2.16
	Day	24.3	0.3	1.9	6.77	–0.68	1.34	6.29	0.02	2.21
LSMMOD	Night	16.8	1.47	3.15	6.12	-1.70	2.16	3.73	0.80	2.06
	Day	24.2	0.17	1.86	6.92	-0.52	1.27	5.95	-0.33	2.19
SLUCM1	Night	16.8	1.49	3.21	6.08	-1.74	2.19	3.75	0.81	2.19
	Day	24.2	0.17	1.86	6.92	-0.53	1.27	6.27	-0.01	3.86
SLUCM2	Night	16.8	1.42	3.20	6.10	-1.72	2.17	3.77	0.83	2.15
	Day	24.2	0.14	1.86	6.96	-0.48	1.25	6.25	-0.03	2.18

Table 3.3: Same as Table 3.2, but for urban (OKCNET) stations. The bold numbers represent better results compared with other cases.

Urban Stations		T_{low} (^{o}C)			q_{low} (g kg^{-1})			WS_{low} (m s^{-1})		
		Mean	MB	RMSE	Mean	MB	RMSE	Mean	MB	RMSE
OBS	Night	17.3	–	–	6.54	–	–	2.35	–	–
	Day	24.7	–	–	6.98	–	–	4.47	–	–
CTRL	Night	16.6	–0.65	3.05	6.02	–0.52	0.91	4.28	1.94	2.69
	Day	23.6	–1.09	1.63	7.30	0.31	1.12	6.69	2.22	3.42
LSM	Night	17.8	0.49	**2.54**	5.64	–0.9	1.15	3.97	1.62	2.50
	Day	24	**–0.64**	**1.36**	6.59	–0.4	1.22	6.05	1.58	2.82
LSMMOD	Night	17.4	**0.13**	2.62	5.98	**–0.55**	**0.94**	3.32	**0.97**	**1.88**
	Day	23.9	-0.78	1.43	6.88	–0.10	1.09	5.16	**0.69**	**2.26**
SLUCM1	Night	18.0	0.74	2.77	5.73	–0.81	1.08	3.86	1.50	2.76
	Day	23.9	–0.79	1.44	6.77	–0.21	1.12	6.68	2.22	3.36
SLUCM2	Night	17.4	0.17	2.82	5.81	–0.73	1.03	3.66	1.31	2.51
	Day	23.8	–0.93	1.53	7.00	**0.01**	**1.08**	6.64	2.18	3.35

bias common with the YSU PBL scheme (Hu et al. 2010; Coniglio et al. 2013; Clark et al. 2015), though it may also be a byproduct of too-dry soil moisture initialization (Fig. 3.6). Simulated rural wind speeds are in agreement with observations during the day, but are overestimated by $\sim 25\%$ at night in all simulations (Table 3.2 and Fig. 3.5c). Simulated urban areas (Table 3.3 and Fig. 3.5a,b) are also too warm (except in CTRL, which has no urban areas) and dry at night, particularly for SLUCM. However, daytime urban tempera-

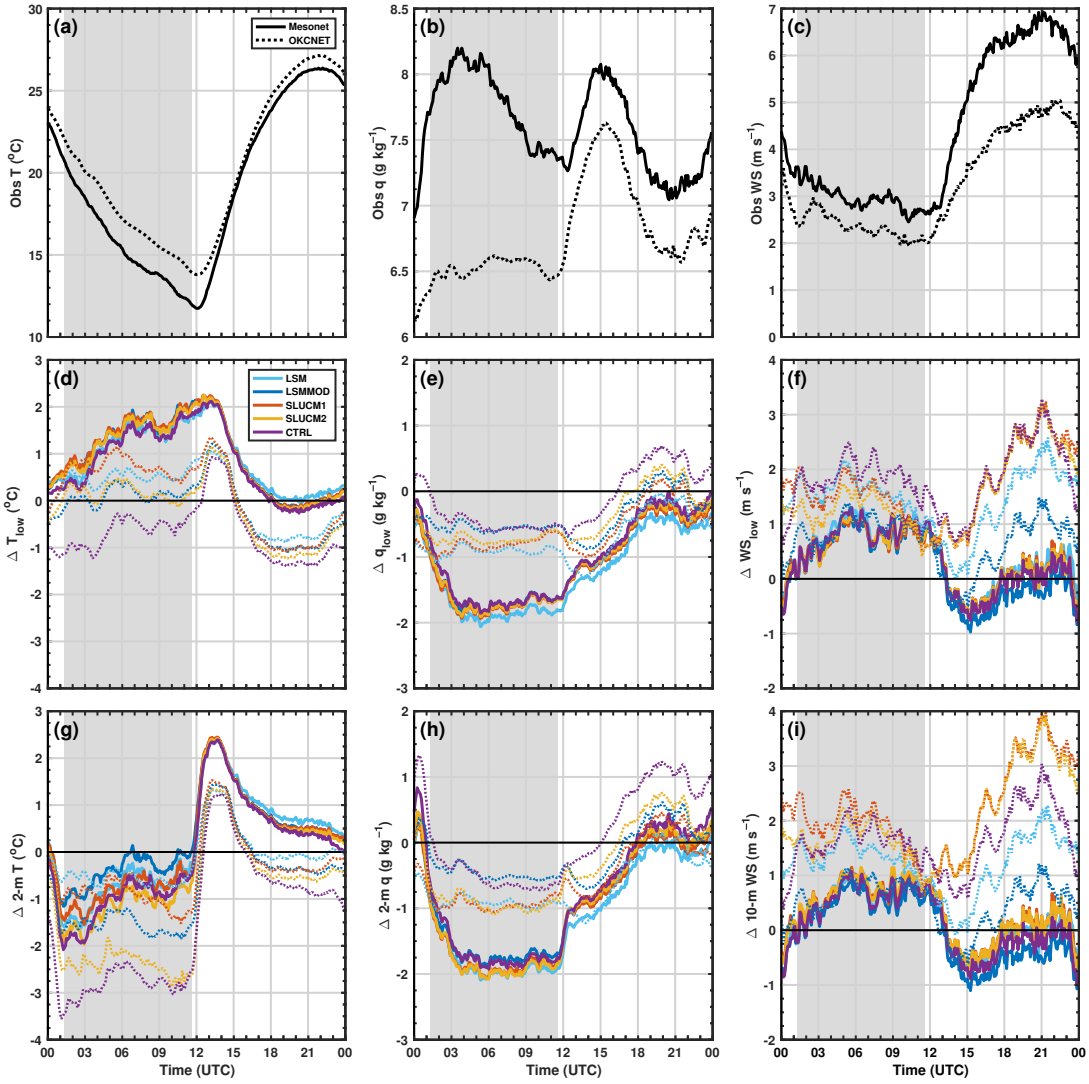

Figure 3.5: Diurnal variation of simulation-average 9-m observed OKCNET (dashed) and Mesonet (solid) (a) T (^{o}C), (b) q (g kg^{-1}), and (c) WS (m s^{-1}). Also, diurnal variation of simulation-average differences from OKCNET (dashed) and Mesonet (solid) observations for (a) first-model-level T, (b) first-model-level q, (c) first-model-level WS, (d) 2-m T, (e) 2-m q, and (f) 10-m WS. Comparisons are made only for model results from the grid points closest to each OKCNET and Mesonet station location. Positive (negative) values denote a greater (lesser) modeled value than observations. LSMMOD, SLUCM1, SLUCM2, and CTRL correspond to the blue, red, yellow, and purple lines, respectively. Times from sunset to sunrise are shaded in gray.

tures are underestimated by all urban simulations, and simulated daytime urban mixing ratios agree well with observations. The CTRL simulation has the

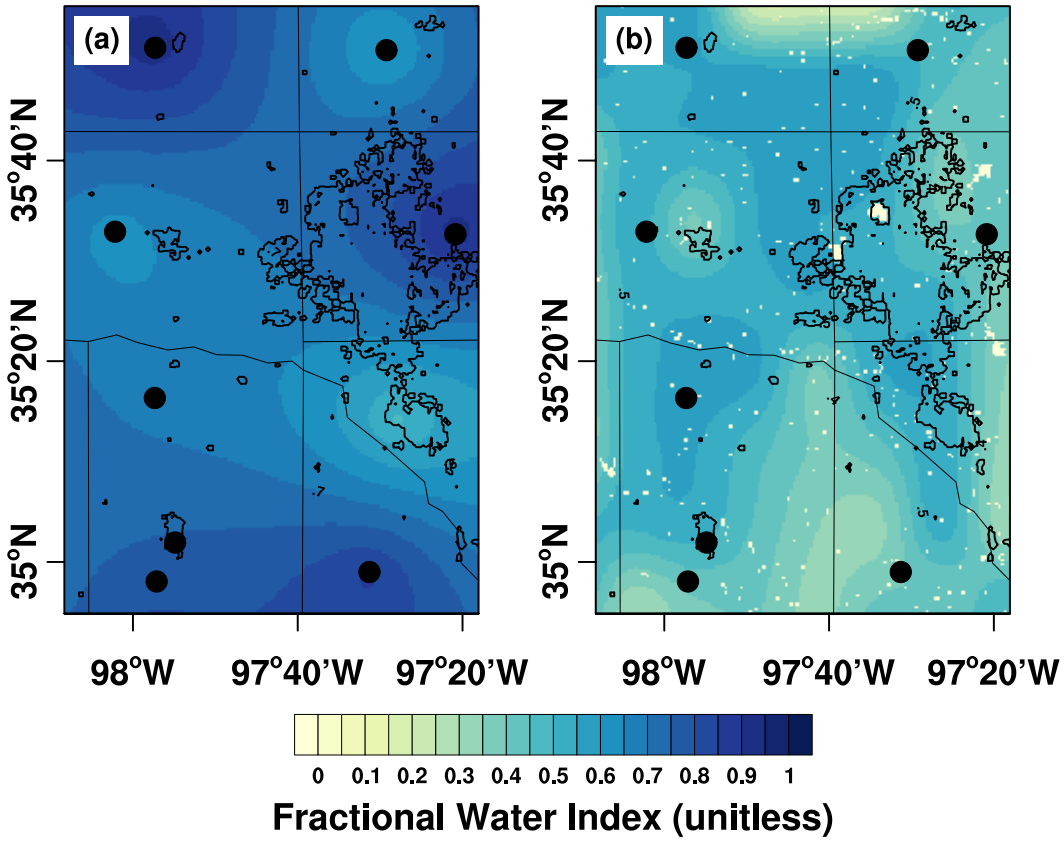

Figure 3.6: Color-filled contours of fractional water index (FWI; Schneider et al. 2003) (a) as observed by Mesonet stations and interpolated using kriging interpolation, and (b) as used in the WRF initialization. NLCD 2011 urban fraction of 0.1 m^2 m^{-2} and Oklahoma county boundaries are contoured in black. Black dots are rural Mesonet sites. FWI is a unitless measure of how close the soil is to saturation, with 0 indicating that the soil is at the wilting point, and 1 indicating that the soil is saturated.

coolest temperatures and highest mixing ratios throughout the day, indicating the urban-induced thermodynamic modifications in the simulations with urban areas. Simulation LSMMOD outperforms all other simulations for both urban MB and RMSE for daytime and nighttime wind speed and mixing ratio. Furthermore, LSMMOD has lower absolute mixing ratio and wind speed MB and RMSE than LSM, and a decreased nighttime warm temperature bias, though LSM's lower absolute MB for daytime temperature is a result of its larger neg-

ative moisture bias. Hence, because LSMMOD generally outperforms LSM in urban areas, further analyses will not consider simulation LSM.

Spatial variations in the average daily minimum, maximum, and mean first-model level (approx. 25 m AGL) temperature from SLUCM1 and LSMMOD are compared to kriging-interpolated Mesonet and OKCNET 9-m temperature for the seven days of the simulations in Fig. 3.7. .The SLUCM1 simulation is selected over SLUCM2 because it has urban fraction values assigned per the SLUCM's default values. The UHI effect is evident in the mean (T_{mean}), maximum (T_{max}), and minimum (T_{min}) 9-m temperature (T) observations (Fig. 3.7a,d,g). Observed temperatures are spatially-correlated with urban fraction (Fig. 3.4f; correlation coefficient, $r \sim 0.55$ for T_{min}), particularly over the Oklahoma City central business district (CBD) at night, with an area of warmer ($1 - 2^{o}$C) concentrated in central OKC. During the day, this warm air extends north of the CBD, likely attributable to advection by predominately southerly winds (Fig. 3.3b). Other studies have observed similar spatial distributions of temperature in Oklahoma City (Basara et al. 2008, 2010; Hu et al. 2013, 2016), although there is no evidence of the daytime cool island observed by Basara et al. (2008) during part of their study period.

Observed mean daily 9-m water vapor mixing ratios (q; Fig. 3.8a) are drier in the urban area ($0.5-0.75$ g kg^{-1}), particularly near and north of the CBD. Similar patterns were noted for more dense cities (e.g., Dou et al. 2015). Urban effects on humidity are contradictory; while combustion and lawn irrigation release water vapor in to the urban surface layer (not explicitly accounted for in the present study), replacement of natural vegetation with impervious artificial materials decreases potential evapotranspiration. In addition, warmer and rougher daytime urban PBLs experience greater turbulent mixing and slower near-surface wind speeds than cooler, smoother rural PBLs, increasing the upward flux of mois-

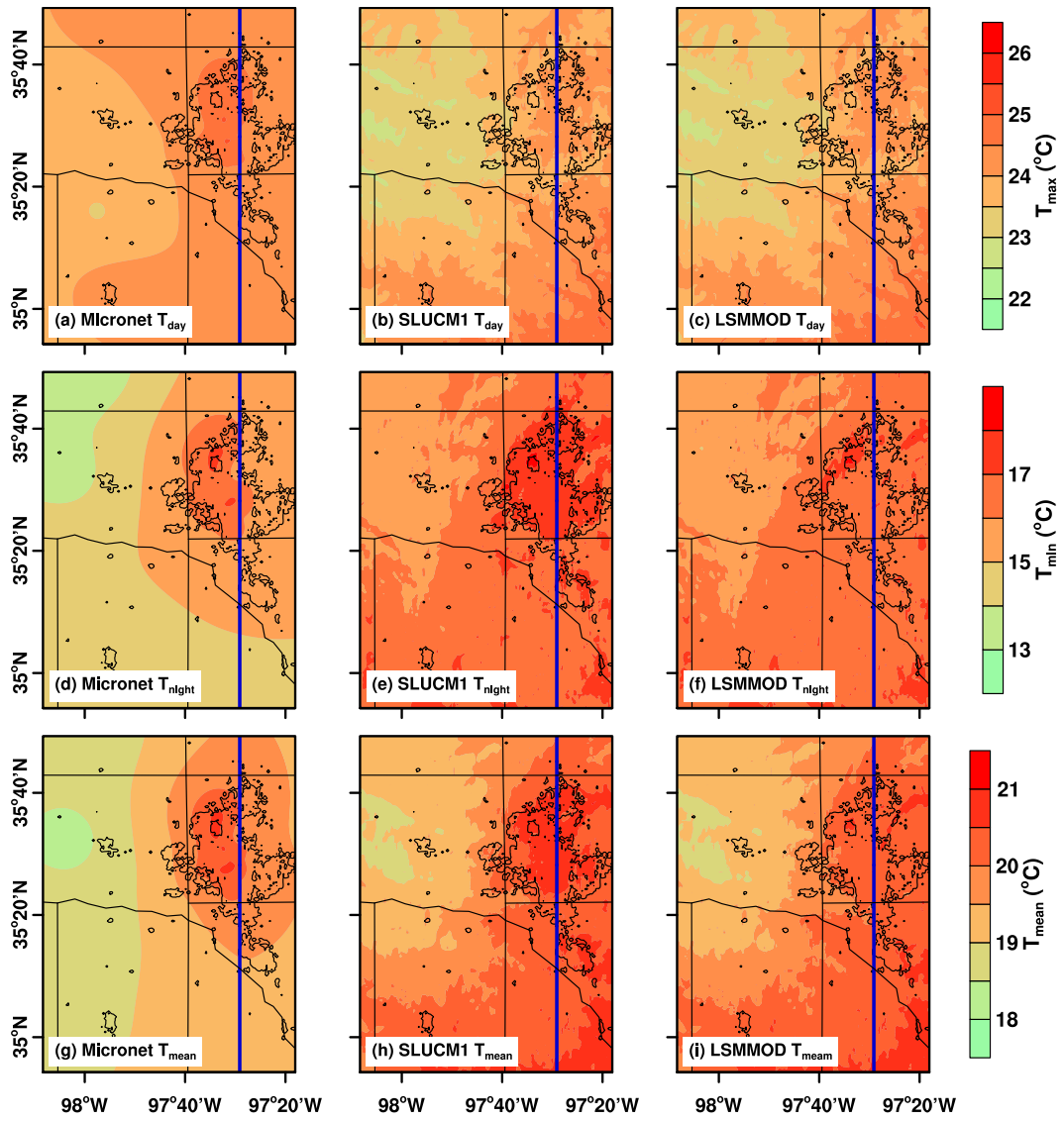

Figure 3.7: (a) Color-filled contours of Kriging-interpolated OKCNET and Oklahoma Mesonet observations of average daytime (1500−2300 UTC) 9-m temperature, T. NLCD 2011 urban fraction of 0.1 m^2 m^{-2} and Oklahoma county boundaries are contoured in black. Model vertical cross sections taken along the blue line ($\sim 97.48^o$W) are plotted in Fig.3.14. (b), (c) Same as (a) but for first-model-level T simulated by SLUCM1 and LSMMOD, respectively. (d)−(f) Same as (a)−(c) but for average nighttime (0400−1100 UTC) temperature. (g)−(i) Same as (a)−(c) but for average daily mean temperature.

ture while also decreasing the surface moisture transfer coefficient. Together, these mechanisms typically result in lower urban humidity values (Grimmond

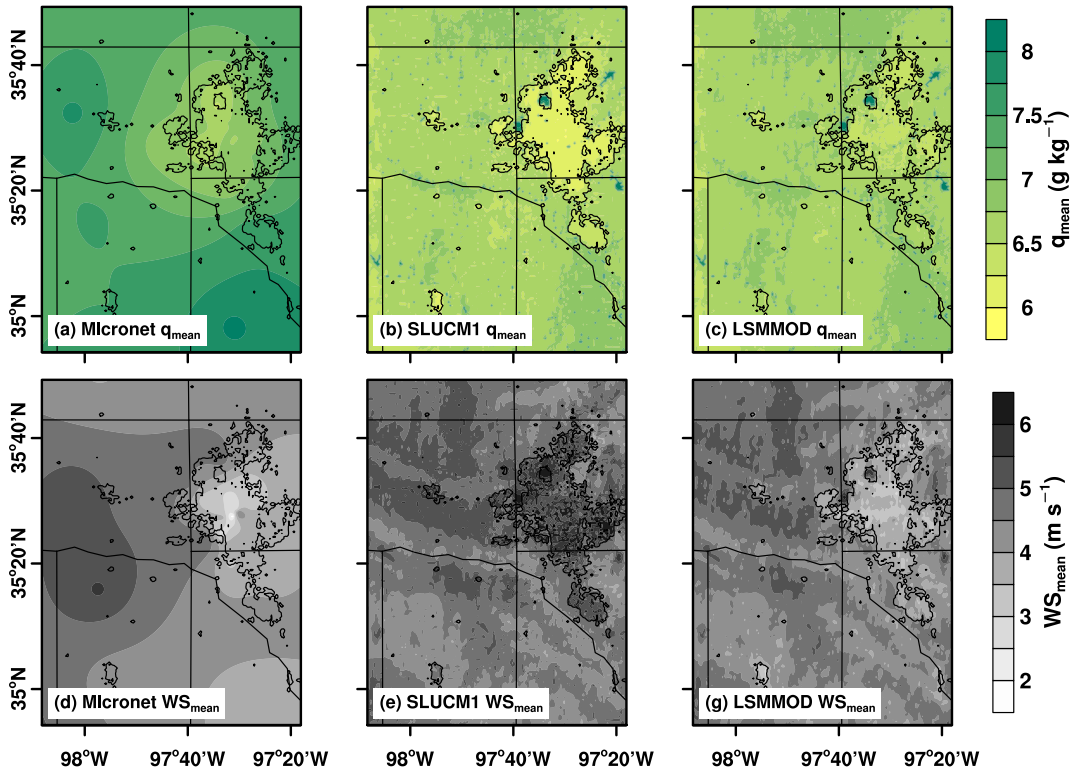

Figure 3.8: (a) Color-filled contours of Kriging-interpolated OKCNET and Oklahoma Mesonet observations of simulation-mean 9-m water vapor mixing ratio, q. Urban fraction of 0.1 m^2 m^{-2} and Oklahoma county boundaries are contoured in black. (b), (c) Same as (a) but for first-model-level q simulated by SLUCM1 and LSMMOD, respectively.(d)−(e) Same as (a)−(c) but for mean wind speed, WS.

and Oke 1986; Dou et al. 2015), hence the dry urban area simulated here is appropriate. Also consistent with this theory, and similar to results from Hu et al. (2016), mean 10-m wind speeds (WS; Fig. 3.8b) are as much as 2 m s^{-1} (approx. 50%) weaker over the CBD than the surrounding rural areas owing to increased surface roughness. However, unlike in the temperature observations, these decreased wind speeds do not appear to be plume-like, but instead appear to be correlated with urban fraction (Fig. 2.1a; $r \sim -0.54$), which suggests that weaker winds are a direct result of increased surface roughness, in agreement with Hu et al. (2016).

The SLUCM1 and LSMMOD simulations reproduce the general warm, dry pattern over most of the urban area (Fig. 3.7b−c,e−f,h−i, Fig.3.8b−c), though both are too warm and dry overall, especially at night. Both of these biases are perhaps a result of over zealous turbulent mixing seen frequently with the YSU scheme (Hu et al. 2010; Coniglio et al. 2013; Clark et al. 2015) as well as dry soils (Fig. 3.6). However, these differences can also be expected given the ∼15-m height difference between the observations and the first WRF model level. However, unlike observations and results from LSMMOD (Fig. 3.8d,g), mean first model level wind speeds in SLUCM (Fig. 3.8e) are only slightly negatively correlated with urban fraction ($r \sim -0.09$), and are generally higher than in rural areas. These results, which appear to be unrealistic given the OKCNET and Mesonet observations, suggest that vertical transport of momentum may be overestimated by the SLUCM/YSU combination, thereby mixing excess momentum downward from aloft.

3.2.2 Model reproduction of diurnal changes in urban-rural differences

The diurnal cycle of observed urban-rural differences in near-surface atmospheric conditions can be analyzed by calculating the averages over all OKCNET sites at each time and subtracting the average of all 8 Mesonet sites (Fig. 2.1) to arrive at an observed urban-rural difference. These sites correspond to those used by Hu et al. (2016) for UHI comparisons, thus our results are directly comparable to their observations. The observed urban-rural differences are compared to WRF-simulated urban-rural dissimilarities. These are computed by subtracting the mean values at each 5-minute output of rural grid points contained in the area covered by Fig. 2.1 but not within box U from averages of urban grid points

within box U in Fig. 2.1. Both observed and simulated urban-rural differences are averaged over days 2−6 of the simulation. Day 1 was not used due to spin-up adjustment time period, and a sharp cold front crossed the study area during day 7, hence the exclusion of both days. The results of these calculations for temperature, T, q, and WS are shown in Fig. 3.9. For each parameter, differences in simulated first-model-level ($\sim$ 25 m) and diagnostic quantities (2-m T and q, and 10-m WS) are compared to observed urban-rural dissimilarities at 9-m. While the diagnostic variables should be closer to the 9-m observations

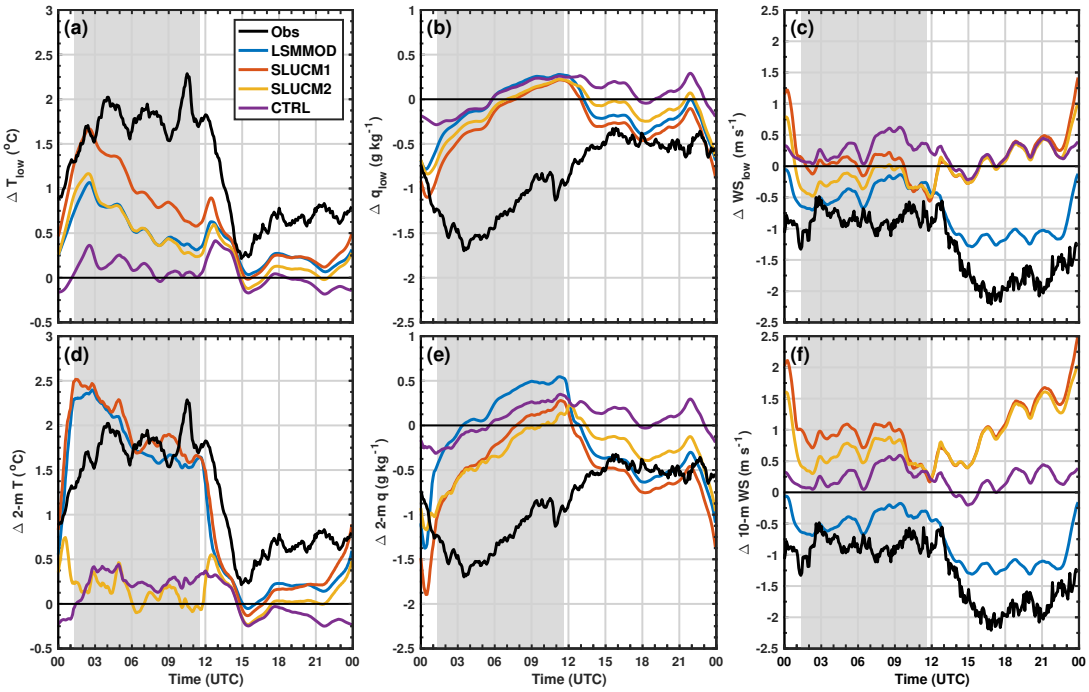

Figure 3.9: Diurnal variation of averages of urban−rural differences in (a) first-model-level T (^{o}C), (b) first-model-level q (g kg^{-1}), (c) first-model-level WS (m s^{-1}) , (d) 2-m T, (e) 2-m q, and (f) 10-m WS. Negative (positive) values denote a greater (lesser) parameter value in the rural areas. Observations are plotted in black, while LSMMOD, SLUCM1, SLUCM2, and CTRL correspond to the blue, red, yellow, and purple lines, respectively. Urban average is taken over all urban grid points inside box U (Fig.2.1), while rural averages are taken over all non-urban points inside box R (Fig.3.4) but outside box U. In all plots, observational urban−rural differences are computed from 9-m measurements. Times from sunset to sunrise are shaded in gray.

than the model-level computations valid at approximately 25 m AGL, they are parameterized values, and are thus more susceptible to errors.

Observed UHII (Fig. 3.9a) remains constant throughout the night near $1.5 - 2^o$C, before decreasing to near 0^oC $\sim$ 3 hr after sunrise. The UHII slowly rises again in response to daytime heating, reaching a maximum daytime UHII of 0.75^oC around 2200 UTC. Differences between the three urban representations of UHII are evident (Fig. 3.9d). Given relatively higher urban fractions, SLUCM1 has a greater UHII at night in both the first-model-level T (Fig. 3.9a) and diagnostic 2-m T (Fig. 3.9d). UHII is higher at 2 m than at 25 m, likely because model-level computations allow for turbulence and diffusion, while diagnostic variables are based primarily on surface fluxes. However, none of the runs sustains the UHII, either at 2 or 25 m, throughout the night at the level ($\sim 2^o$C) seen in the observations. Chen et al. (2014) simulated a similar slow decrease in UHI throughout the night over Beijing. Although UHII is not maintained as long as observed, all three simulations produce a greater first-model-level UHII throughout most of the night than their maximum daytime UHII, which agrees with the observations.

Measured urban mixing ratios are consistently drier than those in rural areas (Fig. 3.9b), especially when rural downward turbulent transport of drier air decreases overnight, when the mean urban mixing ratio is as much as 1.5 g kg^{-1} drier. These observations agree with those of Hu et al. (2013) which suggested that, in the absence of strong low-level wind speeds, turbulence decreases dramatically in rural areas after sunset, while rougher and warmer surface characteristics of urban areas result in enhanced vertical mixing, which then inhibits the formation of a cool, moist, surface-based stable layer. None of the WRF runs correctly reproduces this diurnal pattern. While daytime urban-rural mixing ratio differences are comparable to observations ($\sim$0.5 g kg^{-1}), particularly

for 2-m q (Fig. 3.9e), nighttime urban and rural mixing ratio differences are near zero. This difference is perhaps because of the strong wind speed and dry biases in rural areas (Table 3.2), which may inhibit the formation of the rural stable layer. Both simulated and observed urban-rural mixing ratio differences decrease dramatically near sunset. However, modeled urban-rural differences reduce shortly afterwards, while observed differences remain constant for several hours before slowly equalizing.

The most noticeable difference between the three urban runs is in their simulation of near-surface wind speeds (Fig. 3.9c,f). The LSMMOD run, similar to observations, produces lower urban wind speeds throughout the diurnal cycle, with the greatest differences ($\sim$1 m s^{-1}, $\sim$ 15%) occurring during the daytime. However, nighttime urban and rural wind speeds in SLUCM1 and SLUCM2 are very similar at 25 m, and urban 10-m wind speeds are upwards of 1 m s^{-1} ($\sim$ 23%) *greater* than over rural areas, which is in disagreement with observations. These results are in accordance with the diurnal mean wind speeds seen in Fig. 3.8d, and those simulated by Hu et al. (2016).

3.2.3 Urban modification of surface and near-surface properties

To ascertain exactly how the various representations of the Oklahoma City urban area modify their environment, the analysis from here will consider differences between CTRL and each of the three urban runs, LSMMOD, SLUCM1, and SLUCM2, averaged over days 2−6 of the simulation. Fig. 3.10a−f shows that urban−CTRL differences in near-surface T, q, and WS are similar to the urban−rural differences seen in Fig. 3.9. First-model level and 2-m temperatures are warmer in the urban runs, especially at night, with SLUCM1 producing the

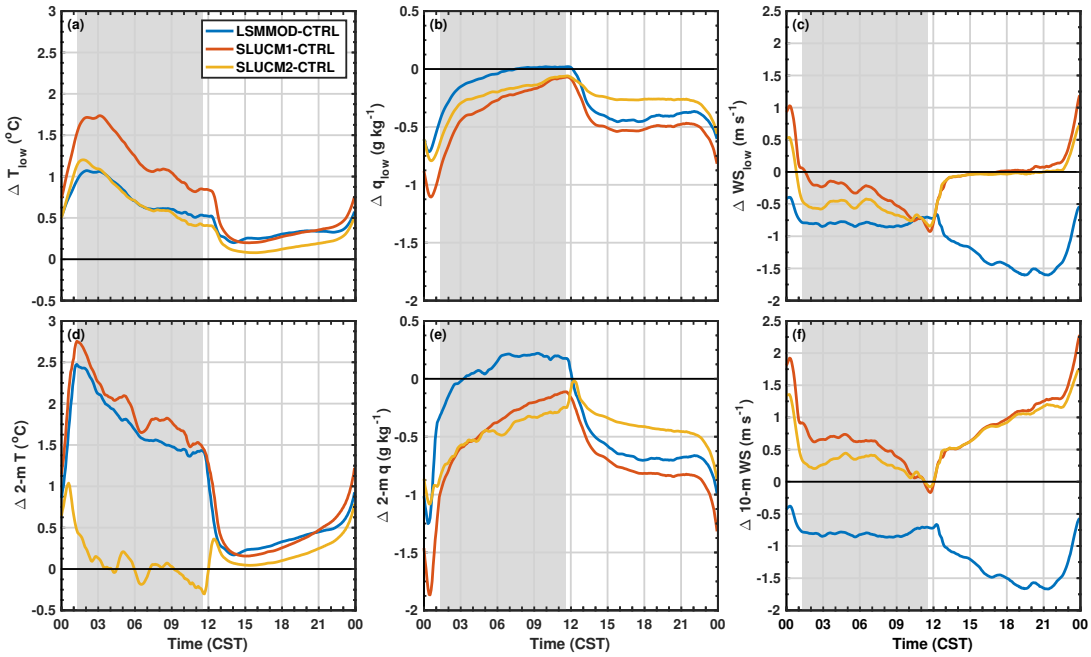

Figure 3.10: Diurnal averages of urban-CTRL run differences, averaged over urban areas in box U (Fig.2.1), in (a) first-model-level T (^{o}C), (b) first-model-level q (g kg^{-1}), (c) first-model-level WS (m s^{-1}) , (d) 2-m T, (e) 2-m q, and (f) 10-m WS. Negative (positive) values denote a greater (lesser) value in the CTRL run. LSMMOD-CTRL, SLUCM1-CTRL, and SLUCM2-CTRL correspond to the blue, red, and yellow lines. Times from sunset to sunrise are shaded in gray.

warmest nocturnal near-surface temperatures. Additionally, all urban runs produce generally drier urban areas, especially in the early evening, while SLUCM1 and SLUCM2 (LSMMOD) have higher (lower) wind speeds over the city during the day.

To further investigate how these average urban-CTRL differences are produced, we examine spatial distributions of T (Fig. 3.11) throughout the diurnal cycle. During the day (1500 to 2300 UTC), all three urban runs have urban temperatures $\sim 0.0 - 0.5^o$C greater than the CTRL run (Fig. 3.11a−c), with somewhat warmer temperatures in LSMMOD (Fig. 3.11a) and SLUCM1 (Fig. 3.11b) compared to SLUCM2 (Fig. 3.11c). Evening (0000−0400 UCT; Fig. 3.11d-f) urban near-surface temperatures are even warmer compared to CTRL

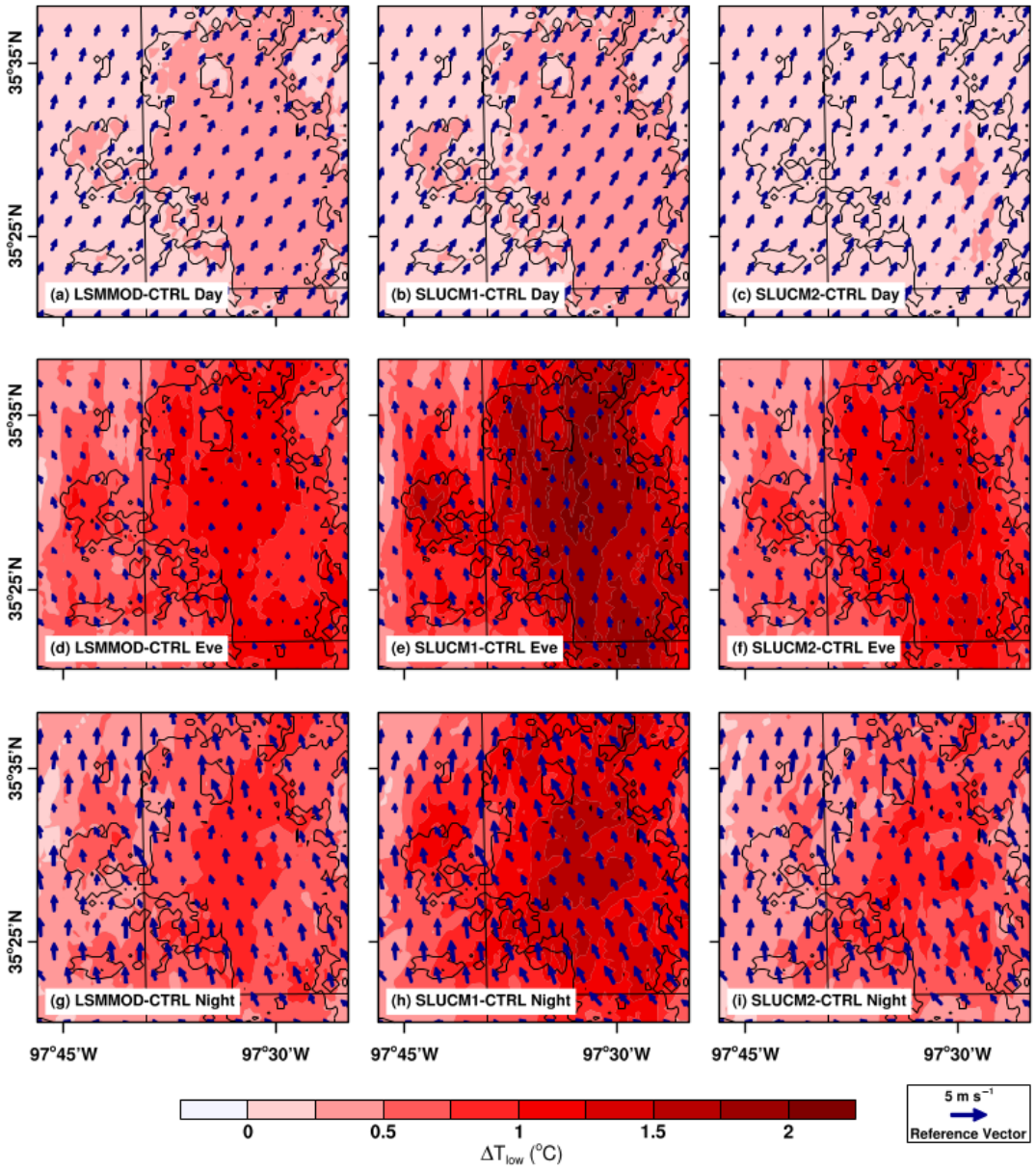

Figure 3.11: (a)-(c) Color-filled contours of average urban-CTRL run differences in box U (Fig. 3.4) of first-model-level T (^{o}C), as well as urban run first-model-level wind speeds (blue arrows), during daytime (1500−2300 UTC) for LSMMOD−CTRL, SLUCM1−SLUCM2, and SLUCM2−CTRL. Negative (positive) contoured values denote a greater (lesser) value in the CTRL run. Urban fraction of 0.1 is contoured in black. (d)−(f) Same as (a)−(c) but for evening (0000−0400 UTC). (g)−(i) Same as (a)−(c) except for nighttime (0400−1100 UTC).

than during the day, with SLUCM1 the warmest during the evening (Fig. 3.11e; $> 2^{o}$C over northwestern OKC). SLUCM2's (Fig. 3.11f) urban area is also warmer during the evening than that of LSMMOD (Fig. 3.11d), but cooler than that of SLUCM1, and SLUCM2's warmest area is more concentrated over and downwind of the CBD than the other 2 runs. The spatial patterns of nocturnal (0400−1100 UTC) near-surface temperatures in LSMMOD (Fig. 3.11g), SLUCM1 (Fig. 3.11h), and SLUCM2 (Fig. 3.11i) are similar to those in the evening, though the urban warming is $\sim 0.5 - 1.0^{o}$C less intense.

The diurnal cycle of spatial distributions of first-model-level wind speeds are also examined in Fig. 3.12. During the day, the wind speeds in the LSMMOD run (Fig. 3.12a) are $1-3$ m s^{-1} ($15-20\%$) slower over urban areas than in the CTRL run, with the slowest wind speeds located in central OKC. However, neither SLUCM1 (Fig. 3.12b) or SLUCM2 (Fig. 3.12c) show similar patterns of wind speed differences, with few concentrated areas of winds faster or slower than in CTRL anywhere near the city. Near sunset, urban wind speeds remain slower in LSMMOD (Fig. 3.12d), however to a lesser degree than during the day. Evening urban wind speeds in SLUCM1 (Fig. 3.12e) are, in many locations, faster than those in CTRL, particularly on the southwest side of OKC. However, the pattern of SLUCM2−CTRL wind speeds (Fig. 3.12f) now more closely resembles those of LSMMOD−CTRL, with mostly slower wind speeds over OKC. At night (Fig. 3.12g−i), wind speeds in LSMMOD and SLUCM2 are $0.5 - 2.0$ m s^{-1} slower over all of OKC, and $0.0 - 1.5$ m s^{-1} slower in SLUCM1.

Analyzing all observations within an urban area as a single category, when each is affected by the different underlying surface structure and LULC, may be inadequate to properly analyze urban effects (Stewart 2011; Stewart and Oke 2012). The spatial plots of T, q, and WS show that simulated temperature and wind speed are dependent on urban category or urban fraction, as the warmest

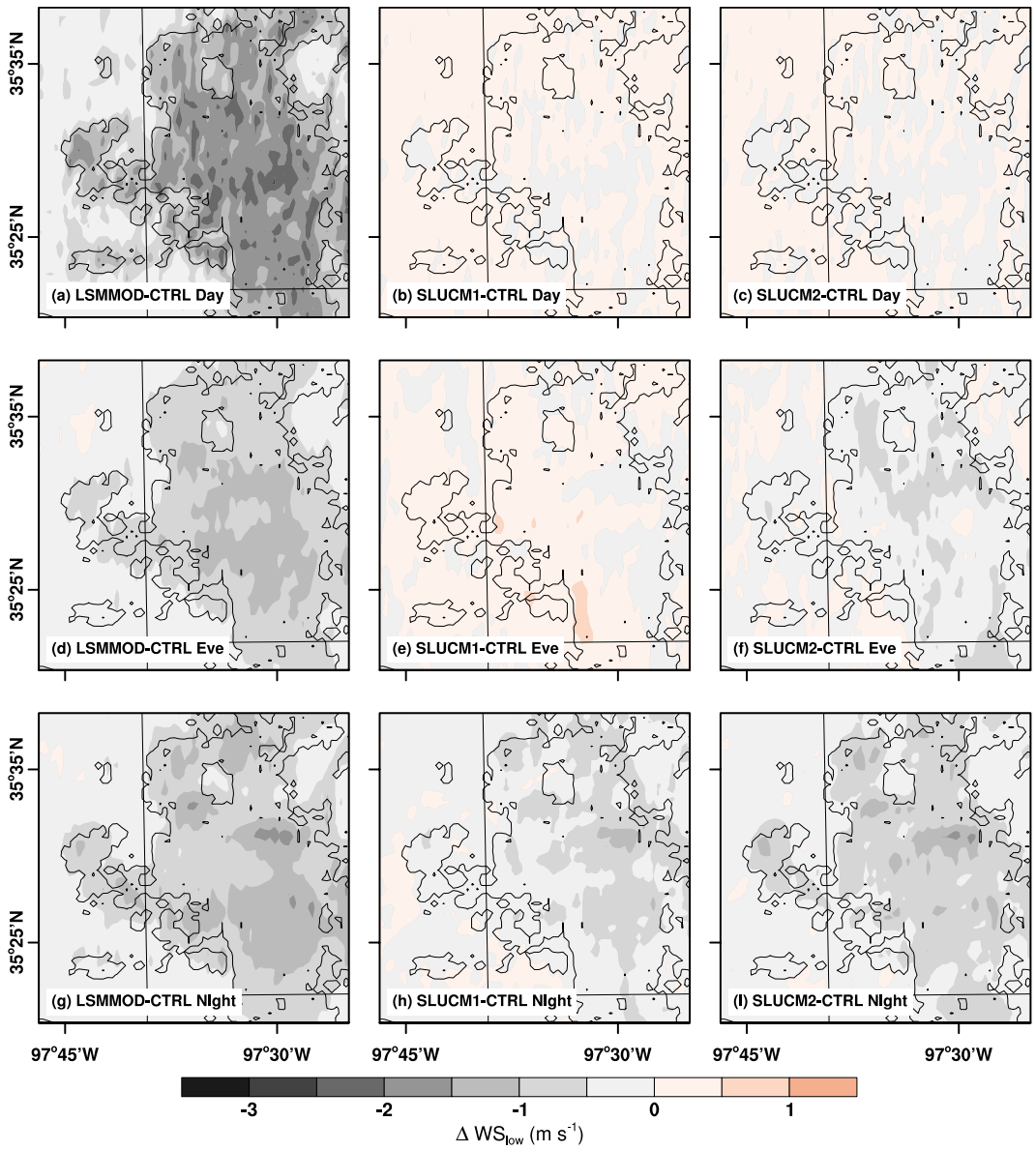

Figure 3.12: Same as Fig. 3.11 but for first-model-level wind speed difference

first-model-level temperatures and slowest first-model-level wind speeds are often concentrated near the CBD (e.g. Fig. 3.11f and Fig. 3.12a). Analysis of OKCNET observations by urban category by Hu et al. (2016) suggested that this should be the case for OKC. Analysis of the times series of the 5-day mean and standard deviation of urban−CTRL temperature (Fig. 3.13a-c) and wind speed (Fig. 3.13d-f) differences for each urban category indicates that this is only some-

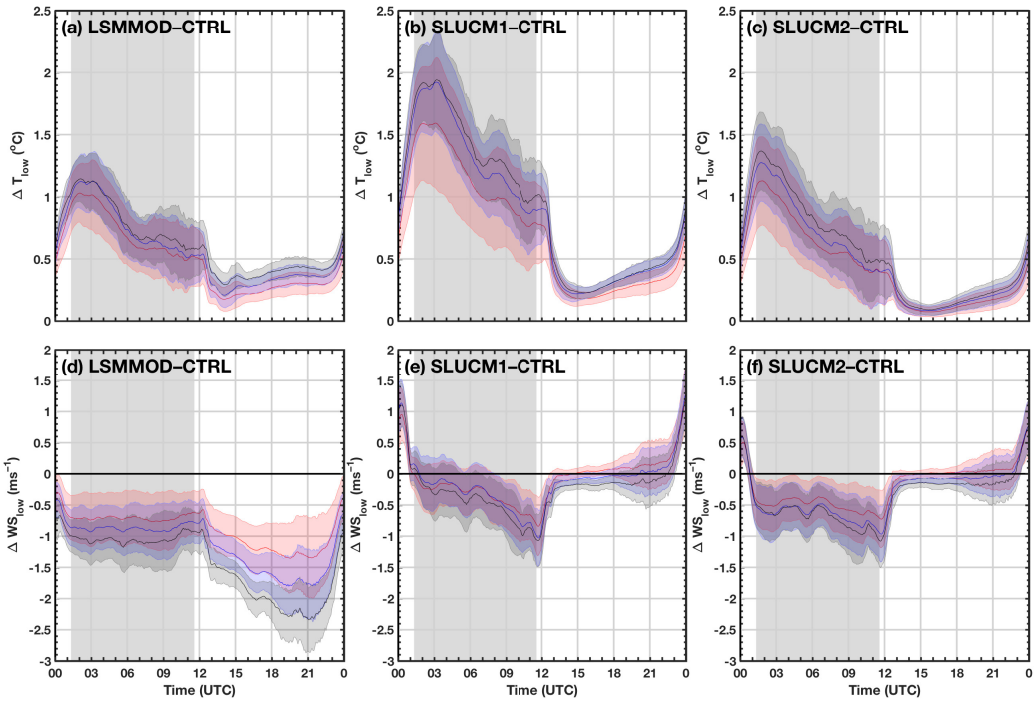

Figure 3.13: (a) Diurnal averages (solid line) and standard deviation (shaded) of first-model-level temperature (^{o}C) averaged over low-intensity residential (blue), high-intensity residential (red), and commercial (black) grid points in box U (Fig. 3.4) for LSMMOD−CTRL. Negative (positive) values denote a greater (lesser) value in the CTRL run. Times from sunset to sunrise are shaded in grey. (b) Same as (a) but for SLUCM1−CTRL. (c) Same as (a) but for SLUCM2−CTRL. (d)−(f) Same as (a)−(c), but for wind speed (m s^{-1}).

times the case. While the distribution means of daytime wind speeds associated with the three urban categories in LSMMOD−CTRL are separated noticeably (Fig. 3.13d), little distinction is present between wind speed differences over the same points in SLUCM−CTRL (Fig. 3.13e) and SLUCM2−CTRL (Fig. 3.13f). In contrast, first-model-level nighttime urban−CTRL temperatures associated with the three urban categories are all very similar in LSMMOD−CTRL (Fig. 3.13a) and SLUCM2−CTRL (Fig. 3.13c), while in SLUCM1−CTRL nighttime temperatures in low-intensity residential areas are cooler than those of the more urbanized categories (Fig. 3.13b). Both of these results corroborate the rel-

atively uniform distribution of SLUCM1−CTRL and SLUCM2−CTRL wind speeds (Fig. 3.12) and LSMMOD temperatures (Fig. 3.11) throughout the day.

3.2.4 Urban modifications of the planetary boundary layer

Urban effects are also seen throughout the PBL. Vertical cross sections of q and potential temperature, θ, near peak heating (2100 UTC), along the north-south line in Fig. 3.7 for LSMMOD−CTRL, SLUCM1−CTRL, and SLUCM2−CTRL are shown in Fig. 3.14. This location was chosen for the cross section because it is aligned along the mean boundary layer wind over the study period, and because it transects the majority of the OKC metro, including downtown OKC. The lowest $\sim$ 1 km of the PBL is drier in each urban run compared to the CTRL simulation, with the drying extending further north and south, and of greater intensity, in LSMMOD and SLUCM1. The drying is also most concentrated over the urban area, as indicated by the trace of run-specific urban fraction below each plot. In addition, SLUCM1 is 0.25 ^{o}C warmer just above the surface, while warmer air extends over a deeper portion of the PBL in LSMMOD, with a few locations of +0.5 ^{o}C air near the ground. The warmer temperatures in the lower portions of the PBL of SLUCM1, and especially in LSMMOD, result in deeper PBLs, denoted by the black (blue) line for the CTRL (urban) run. A higher PBL top leads to moistening and cooling at the PBL top over the city (given that the PBL is typically topped by an inversion), especially in LSMMOD, where the atmosphere is up to 0.5 g kg^{-1} moister and 0.5 ^{o}C cooler. Cross sections across other parts of OKC (not shown) show similar urban-CTRL run differences.

To quantify how each urban parameterization modified the PBL throughout the day, CTRL (Fig. 3.15a,e) and urban−CTRL θ, q, WS, and vertical wind

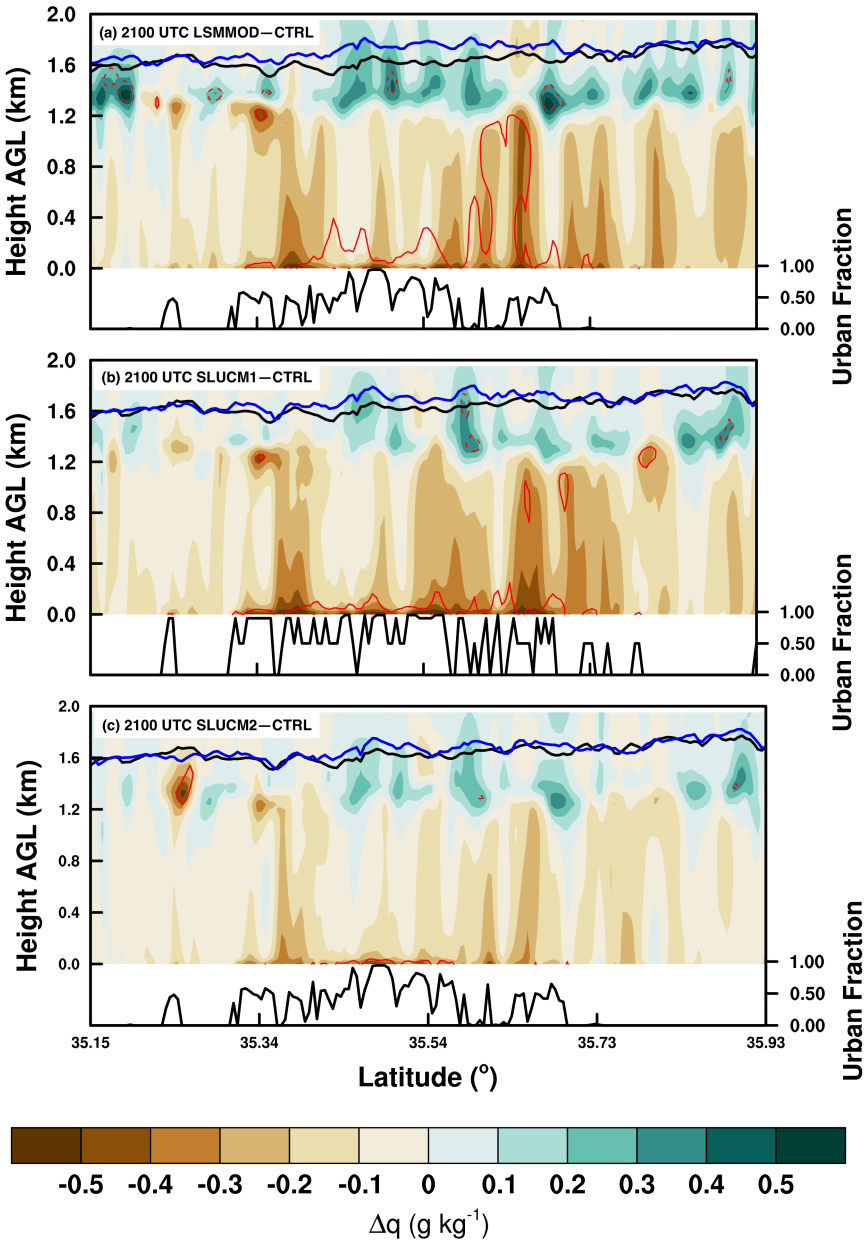

Figure 3.14: Vertical cross section along the line in Fig. 3.7 of average 2100 UTC mixing ratio (filled contours) and potential temperature (red lines ever 0.25 ^{o}C; negative dashed, positive solid, 0 line not shown) for (a) LSMMOD−CTRL, (b) SLUCM1−CTRL, and (c) SLUCM2−CTRL. Negative (positive) values denote a greater (lesser) value in the CTRL run. Also shown in cross section are PBL height of CTRL (black line) and each urban run (blue line) along the cross section line. Plotted below each vertical cross section is urban fraction of each urban run along the line.

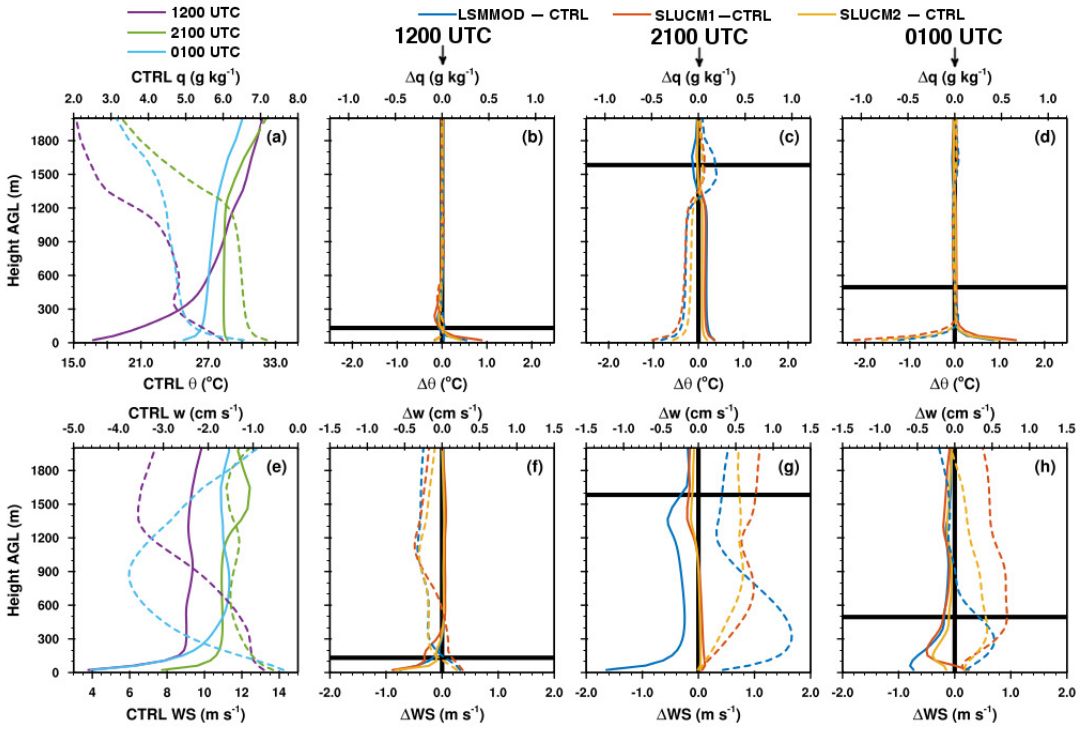

Figure 3.15: (a) Mean CTRL θ (^{o}C; solid) and q (g kg^{-1}; dashed) as a function of height over urban areas in box U (Fig. 3.4) at 1200 UTC (purple), 2100 UTC (light green) and 0100 UTC (light blue). (b) Averages of urban-CTRL run differences in θ (^{o}C; solid) and q (g kg^{-1}; dashed) at 1200 UTC as a function of height, averaged over all urban locations in box U (Fig. 3.4). Negative (positive) values denote a greater (lesser) value in the CTRL run. LSMMOD−CTRL, SLUCM1−CTRL, and SLUCM2−CTRL correspond to the blue, red, and yellow lines. Thick black horizontal line is the average simulated PBL height at this time. (c) Same as (b) but at 2100 UTC. (d) Same as (b) but at 0100 UTC. (e) Same as (a) but for WS (m s^{-1}; solid lines) and w (cm s^{-1}; dashed). (f)−(h) Same as (b)−(d), but for urban–CTRL differences in WS (m s^{-1}; solid lines) and w (cm s^{-1}; dashed).

speed (w), averaged over urban grid points in box U (Fig. 2.1a), are plotted in the lowest 2000 m above urban grid points in box U of Fig. 2.1 at 1200 UTC (Fig. 3.15b,f), 2100 UTC (Fig. 3.15c,g), and 0100 UTC (Fig. 3.15d,h). At 1200 UTC, just after sunrise, all urban runs are 0.5 to 1 ^{o}C warmer just above the surface,

but, owing to minimal nighttime turbulent mixing, this warming does not extend above the shallow PBL (Fig. 3.15b). In addition, due to surface roughness, slower wind speeds are evident in the PBL in all runs, especially nearest the surface (Fig. 3.15f), accompanied by weaker near-surface sinking motion than in CTRL (Fig. 3.15e) because of warmer surface temperatures. Above the PBL, while temperature, moisture, and horizontal wind speed remain relatively unchanged from CTRL, stronger sinking motion is evident just below average daytime PBL height (Fig. 3.15c,g), particularly in LSMMOD and SLUCM2.

Near peak heating at 2100 UTC, the lower urban PBL has dried 0.5–1 g kg^{-1} (Fig. 3.15c) in all runs compared to CTRL (Fig. 3.15a), with somewhat drier air through most of the PBL. The majority of the PBL is also slightly warmer, though not as much so near the surface. As was evident in analysis of first-model-level conditions (Fig. 3.10), the LSMMOD run produces $\sim$ 1.5 m s^{-1} weaker daytime wind speeds near the surface of urban areas, while low-level wind speeds in both SLUCM runs differ little from the CTRL simulation (Fig. 3.15g). The decreased wind speeds in LSMMOD extend through the depth of the PBL, though they are lowest near the surface. Just above the most slowed wind speeds, at $\sim$ 150 m AGL, LSMMOD has weaker sinking motion, nearly neutralizing the downward vertical motions at this height in CTRL (Fig. 3.15e). All runs feature weaker sinking motion near the CTRL PBL top (Fig. 3.15g), particularly in SLUCM1, indicating the increase in PBL height seen in Fig. 3.14.

At sunset (0100 UTC), all runs are $1 - 2^{o}$C warmer and $1 - 1.5$ g kg^{-1} drier than CTRL just above the surface (Fig. 3.15d), in agreement with observations in Fig. 3.10. However, as was the case at sunrise (Fig. 3.15b), these modifications are limited to the air nearest the ground due to lower turbulent mixing than during the day. Wind field deviations near sunset (Fig. 3.15h), however, extend over a larger depth. LSMMOD and SLUCM2 have lower horizontal wind speeds

just above the surface, but reach their maximum difference in speed 50−100 m higher. SLUCM1 also has lower wind speeds $\sim$ 200 m AGL, however SLUCM1's wind speeds nearest the surface are higher than CTRL's, a result echoed in the time series (Fig. 3.10d) of first-model-level SLUCM1 wind speeds. In addition, the daytime weaker sinking motion near the surface evident in LSMMOD (Fig. 3.15g) is now apparent in both SLUCM1 and SLUM2, and extends through the depth of the collapsing PBL. In the SLUCM runs, this weaker sinking motion also continues above the evening PBL, a residual feature from the daytime convective boundary layer (CBL).

3.3 Discussion and Conclusions

This study used the WRF-ARW, run at 500-m horizontal grid spacing with 25-m vertical grid spacing near the ground, to investigate model-simulated urban-atmosphere interactions in Oklahoma City. The CTRL simulation with no urban area served as a comparison point for the urban simulations. These urban runs included the LSM and LSMMOD, using the original and a new, modified version, respectively, of the Noah land surface model to parameterize the urban surface. Also analyzed were two SLUCM simulations using the more complex single-layer urban canopy model parameterization, differing only in their urban fraction values. Simulation SLUCM1 had the default urban fraction values assigned by the urban canopy model, while SLUCM2, through a novel approach, used NLCD 2011 impervious surface data as a proxy for urban fraction, resulting in generally less dense urban areas. The results presented in this study suggested that it is more appropriate to use the modified Noah LSM alone (LSMMOD), instead of the SLUCM-Noah LSM combination, for lower-density cities, which are common in the Great Plains.

The SLUCM1 and LSMMOD runs simulated near surface temperatures in the OKC area reasonably well. First-model-level daily maximum, minimum, and mean temperatures were, on average, $\sim 1^{o}$C warmer over the urban area than nearby rural areas. Both simulations also reproduced the daytime dry urban area seen in observations, although this was not maintained through the night. However, maximum and mean daily temperatures were slightly warmer and mean mixing ratios were drier than observations, biases seen frequently in models using the YSU PBL scheme. Furthermore, given the dry bias of the initialization soil moisture content, future work should investigate how using the high-resolution land data assimilation system (HRLDAS; Chen et al. 2007) to spin up the soil state before WRF simulation, as done by Sharma et al. (2016) and Nemunaitis-Monroe et al. (2016), might improve these results. The SLUCM1 run also was unable to produce weaker winds over urban areas as seen in observations, while LSMMOD's urban wind speeds more closely agreed with observations.

All simulations (LSMMOD, SLUCM1, and SLUCM2) reproduced the nocturnal UHI relatively well, with urban-rural differences ranging from $\sim 1-1.5^{o}$C overnight. However, SLUCM1 produced a more intense, and thus more realistic, nocturnal UHI than LSMMOD and SLUCM2, although the urban fractions in SLUCM1 are less representative of the city. Evaluations of rural and urban observations separately suggest that the models' weak nocturnal UHIIs are a result of a warm bias in rural areas as opposed to a cool bias in urban areas. Results show that while the daytime UHI was accurately reproduced as less intense than the nocturnal UHI, all three urban simulations produced only a slightly warmer ($\sim 0.25^{o}$C) daytime urban area, compared to observations of a $\sim +0.5-1^{o}$C daytime UHI. Owing to lower urban densities in OKC, the SLUCM2 simulation had a weaker nighttime and daytime UHI than in the SLUCM1 run. However,

given the UHI in SLUCM1 was already too weak, the UHI in SLUCM2 had an even greater cool bias.

Additionally, observed wind speeds were lower in the urban area, especially during the day. The biggest difference between the three urban simulations was the failure of either SLUCM run to produce this phenomenon. However, the diurnal cycle of urban-rural differences in wind speed in the LSMMOD simulation agreed well with observations. Wind speeds as a function of urban category were analyzed to investigate the role of surface roughness in producing these differences. While increasingly rough urban surfaces (i.e. higher-intensity urban areas) resulted in progressively slower wind speeds in the LSMMOD run compared to the CTRL run, wind speeds over all urban surfaces were roughly the same in both SLUCM runs, regardless of urban category.

Hu et al. (2016) theorized the cause of the higher near-surface wind speeds in the WRF during the evening to be an imbalance of friction-induced speed reduction and turbulent transport of increased momentum from aloft caused by inadequacies of the PBL scheme. Other investigations have had similar difficulties correctly simulating evening and nocturnal wind speeds with the WRF (e.g. Zhang and Zheng 2004; Lee et al. 2011; Ngan et al. 2013). However, as all of the runs examined here use the same PBL scheme, and the differences in wind speeds are noticeable during the daytime, their theory cannot account for the discrepancies shown here between the SLUCM and LSMMOD simulations. Miao et al. (2009) noted increased wind speeds in the city center of Beijing while using the SLUCM, which they attributed to increased turbulence, however they did not have a simulation using only the LSM to which to compare these findings. It is possible that the core of OKC is not large or aerodynamically rough enough to result in the turbulence-induced acceleration of the winds that Miao et al. (2009) observed in Beijing. Further testing of the SLUCM is needed to

ascertain the cause of these erroneous wind speeds in OKC.

It is troublesome that providing the SLUCM with more accurate surface characteristics would result in a less realistic UHI representation. Contrary to these results, Li et al. (2013) found that using urban fraction computed directly from 30-m NLCD 2006 data (Fry et al. 2011) improved the representation of surface energy balance terms. The SLUCM, designed around the "urban canyon" observations of Nunez and Oke (1977), assumes that all urban areas are covered by closely-spaced buildings with canyon-like streets and alleys in between. Indeed most studies which have used the SLUCM-Noah LSM modeling system to simulate UHIs are performed over large, densely populated cities such as New York City (Holt and Pullen 2007), Taipei (Lin et al. 2008), and Beijing (Miao et al. 2009). Few studies have used the SLUCM to simulate the UHI of cities that are less dense and with greater suburban sprawl. The results herein suggest that the SLUCM may not always be suited for use in less-dense urban areas, particularly if accurate reproduction of urban wind speeds are important. However, a more accurate aerodynamic parameterization for the SLUCM, as suggested by Varquez et al. (2015), could be used to attempt to remedy this problem in future simulations.

Recent developments aimed at eliminating these deficiencies from urban canopy parameterizations have focused on developing multi-layer urban canopy models, particularly the Building Energy Parameterization (Martilli 2002) and Building Energy Model (Salamanca et al. 2010) in the WRF. Studies using these parameterizations have indicated their ability to improve PBL temperatures and wind speeds in urban areas (e.g., Gutiérrez et al. 2015a,b; Sharma et al. 2016). However, both of these parameterization options are incompatible with the non-local YSU PBL scheme, which was chosen for this study because of its suitability for use in severe weather environments (Coniglio et al. 2013;

Clark et al. 2015). However, the local-mixing Mellor-Yamada-Nakanishi-Niino PBL scheme (MYNN; Nakanishi 2000, 2001; Nakanishi and Niino 2004, 2006), which is also appropriate for use in severe weather situations (Coniglio et al. 2013) could be used with the multi-layer urban parameterization options, hence this is an avenue for future investigation.

Chapter 4

Influence on a simulated supercell of the storm-relative location of a large Great Plains urban environment

Now that it has been shown the modified LSM is the most appropriate urban parameterization for use in a great plains urban environment, it will be used to parameterize a large Great Plains urban environment (Dallas-Ft. Worth; DFW) in simulations of an isolated supercell. The interactions between DFW, which is placed in 108 distinct locations within the innermost domain, and the supercell will be analyzed. The goal here is not to reproduce exactly the events of a particular day (in this case, 31 May 2013), but to quantify the effects that DFW has on the strength and evolution of the supercell. Using analyses of simulations grouped based on cluster analysis, this chapter will show that the city has a statistically significant effect on storm strength, and that these modifications vary based on the storm-relative location of the city. Storm inflow differences will be quantified to investigate possible causes of changes in storm strength, and these differences in inflow characteristics will be connected to urban effects.

4.1 Model configuration and simulation descriptions

Simulations are performed using the ARW-WRF Version 3.6.1. Three one-way nested domains (Table 4.1) are used with 4.5 km, 1.5 km, and 0.5 km horizontal grid spacing and domain sizes of 300 x 300, 399 x 399, and 498 x 498, respectively (Fig. 4.1a). All domains have 119 vertical terrain-following grid points, spaced at $\sim$ 50 m near the surface and stretching to $\sim$ 150 m spacing at 800 hPa ($\sim$ 2 km AGL) and above. Approximately 20 vertical levels are within the lowest 1.0 km AGL, providing finer vertical resolution in the convective boundary layer (CBL).

All three domains employ the same parameterization options: Goddard short and long wave radiation schemes (Chou and Suarez 1999; Chou et al. 2001; Matsui and Tao 2007), a modified version of the Noah land surface model (LSM; Chen and Dudhia 2001; Ek 2003), as described in Section 2.2 and used in Chapter 3, the MM5 Monin-Obukhov surface layer (Monin and Obukhov 1954; Paulson 1970; Dyer and Hicks 1970; Webb 1970) and corresponding Yonsei University (YSU) PBL scheme (Noh et al. 2003), and the double-moment NSSL micro-

Table 4.1: Simulation domain and parameterization specifications for the simulations in Chapter 4.

	d01	d02	d03
Horizontal grid size	300 × 300	399 × 399	498 × 498
Grid spacing (km)	4.5	1.5	0.5
Vertical levels		119	
Time steps (s)	6	2	1
Microphysics		NSSL	
LW radiation		New Goddard	
SW radiation		New Goddard	
PBL Scheme		YSU	
Land Surface Scheme		Modified Noah LSM	

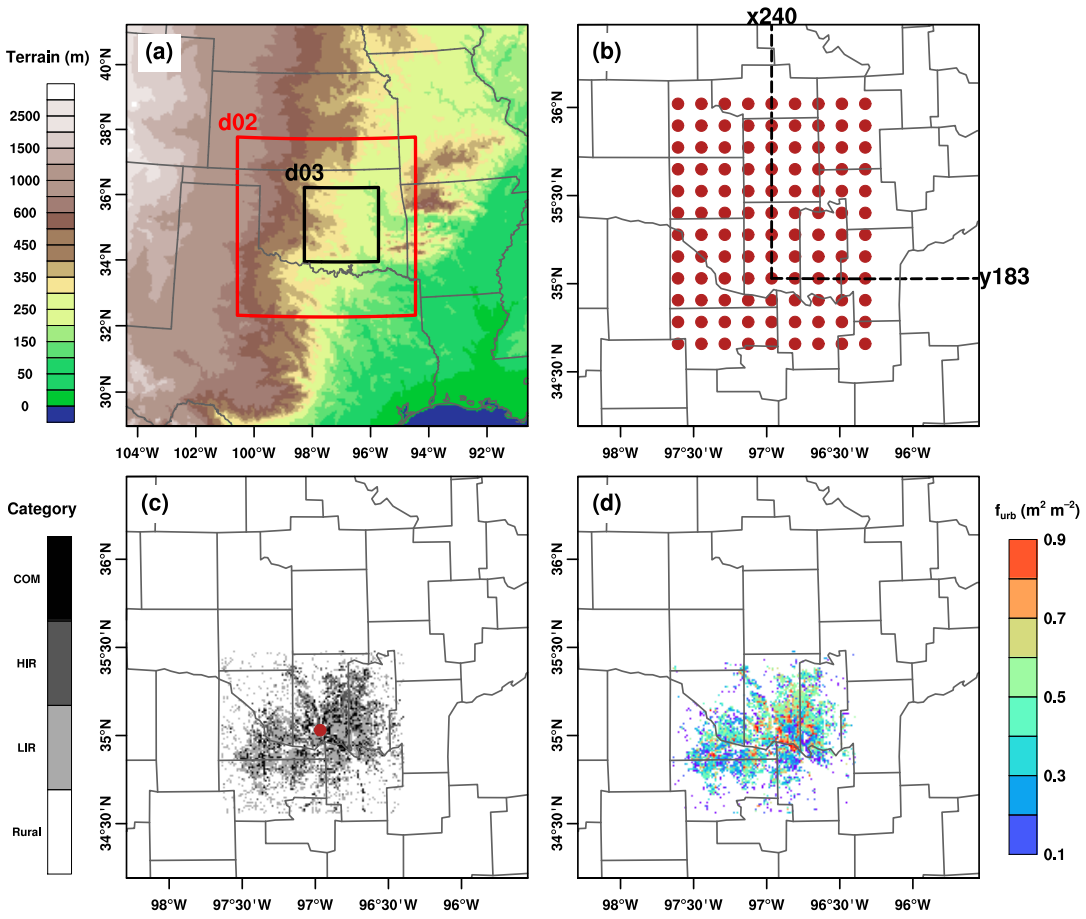

Figure 4.1: (a) Domain locations used for all simulations in Chapter 4. The plotted area is encompassed by d01, and the red and black boxes indicate d02 and d03, respectively. Terrain height is shaded, and state boundaries are in gray. (b) Grid of 108 simulation urban locations (red dots), plotted according to the center of urban fraction mass for each simulation in d03. Oklahoma county lines are in black. (c) Shaded urban land use data for run x240.y183, whose center of mass location (red dot) corresponds to the dashed lines and labels in (b). (d) Same as (c) but for urban fraction.

physics scheme (Mansell et al. 2010), which uses six hydrometeor classes and predicts graupel density. The YSU scheme is selected as it yields PBL properties and depths that agree well with observations, and because it has been shown to perform well in Plains severe weather environments (Coniglio et al. 2013; Clark et al. 2015). An urban canopy model (UCM) is not used to represent urban areas because Chapter 3 shows that the single-layer UCM (SLUCM;

Kusaka et al. 2001; Kusaka and Kimura 2004)—the only explicit UCM available in the WRF that is compatible with the YSU PBL scheme—is not appropriate for use in plains cities, particularly because of its poor prediction of urban wind speeds.

Each simulation is initialized at 0600 UTC (0000 LST) 31 May 2013, with a Rapid Refresh (RAP) analysis, supplemented by offline North American Land Data Assimilation-2 (NLDAS-2) 0.125-degree Noah Model soil moisture and temperature output (Xia et al. 2012), provided by the Goddard Earth Sciences Data and Information Services Center (GES DISC). Simulations are integrated for 21 h to 0600 UTC 01 June 2013 using a time step of 6 s, 2 s, and 1 s for d01, d02, and d03, respectively, with lateral boundary conditions for d01 provided by hourly RAP analyses. In total, 118 separate simulations are performed: one without any urban areas (CTRL); 9 additional simulations without any urban areas but with random, zero-mean normal, small amplitude noise applied to the volumetric soil water content of the top soil layer (CTRLN); and 108 with the Dallas-Fort Worth (DFW) urban area placed in one of 108 regularly-spaced gridded locations (Fig. 4.1b). In addition to removing urban areas from CTRL and CTRLN simulations, the land use type at all grid points of d03 are changed to grassland. For each non-CTRL simulation, three-category urban land use (Fig. 4.1c) and urban fraction (Fig. 4.1d) of DFW, derived from National Land Cover Database (NLCD) land use (Homer et al. 2015) and impervious surface (Xian et al. 2011) data, respectively, are used to represent the characteristics of the DFW urban area. All other areas in d03 remain grassland as in CTRL. The 108 simulations with the land use of DFW are referred to by the location of the mass-weighted center (with urban fraction used as the mass) of DFW relative to the southwest corner of d03 (e.g., the center of DFW in simulation x240.y183 would be 240 grid points (120 km) east and 183 (91.5 km) north of the SW

corner of d03; Fig. 4.1b,c).

The purpose of the CTRLN simulations is to provide an initial-condition ensemble against which to compare variable means across various groups of DFW simulations. If group averages are compared to the single CTRL run, small-scale features from CTRL can dominate the analysis. However, averaging over the CTRLN ensemble makes comparative analyses less dependent on random variability from a single run and better elucidates the dominant signals. Henceforth, the slate of 10 simulations that use the CTRL landuse (i.e., CTRL plus CTRLN) will be referred to as CTRLE, however some analyses will only consider CTRL where appropriate.

This configuration is used to simulate a real meteorological situation interacting with a relatively idealized land use pattern and is not intended to reproduce exactly the events of 31 May 2013. This date, and the events that occurred on it, are irrelevant to the discussions presented here, and this date was chosen purely because the boundary conditions provided by NWP models on this date produced a relatively isolated, long-lived supercell in the chosen WRF configuration. While using the land use of Oklahoma City, instead of DFW, would have been more geographically appropriate, the intention of using the much larger urban area of DFW is to maximize the magnitude and extent of urban effects, while still using the land use pattern of an urban area that is appropriate for the southern Great Plains.

4.2 Results

4.2.1 Event description and CTRL results

On the afternoon of 31 May 2013, surface-based CAPE (SBCAPE) in excess of 4000 J kg^{-1}, negligible surface-based CIN (SBCIN), effective bulk shear from 50–

60 kts, and 0–1-km and 0–3-km storm-relative helicity values of approximately 100 and 200 $m^2\ s^{-2}$, respectively, characterized the unstable warm sector over central OK, east of a surface trough in western OK and south of a stationary front draping across northwestern OK. In other words, all of the ingredients for severe convection (e.g., Johns and Doswell 1992) were present. Conditions within the CTRL simulation's warm sector (Fig. 4.2a–c) generally agree with these observations. Thus, it is no surprise that the model initiates convection over central Oklahoma near the intersection of the dryline and stationary front (Fig. 4.2c) at approximately 2200 UTC.

In d02 of CTRL, simulated convection near this "triple point" intersection in Oklahoma (Fig. 4.3a) propagates eastward off the boundary, and evolves into a long-lived supercell (Fig. 4.3b,c). The simulated supercell produces a mid-level mesocyclone with $\zeta_{max} \geq 0.02\ s^{-1}$ from 2210–0300 UTC as it moves nearly due eastward at $\sim 8\ m\ s^{-1}$. Eventually, this initial supercell dissipates around 0330 UTC, followed by a new area of convection to the north of the supercell (Fig. 4.3d). This convective system organizes into a line of training precipitation cells (Chappell 1986, Fig. 4.3d,e) which remains stationary over east central OK through the end of the model run. The system of training precipitation and the initial supercell result in over 150 mm of rain in some locations (Fig. 4.3f). Simulated convective evolution is similar to reality, though it occurs too far east and convective coverage is more sparse. However, these discrepancies are not germane to the current study since the present goal is to simulate an isolated supercell interacting with different parts of a city, not to reproduce exactly the events of 31 May 2013. The results focus on the initial isolated supercell, from formation at $\sim$ 2130 UTC, to its demise at $\sim$ 0300 UTC. As such, all subsequent simulation details are from d03.

Detailed analysis of d03 results shows that storm initiation occurs at approx-

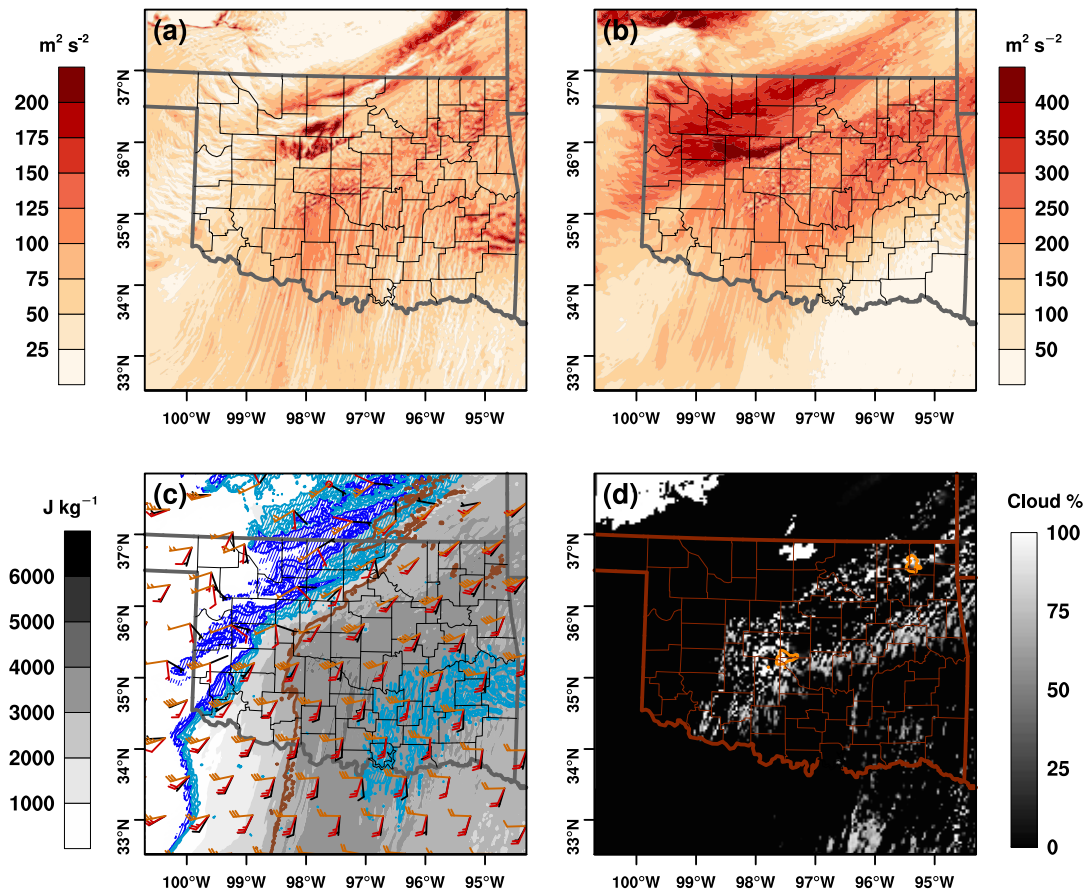

Figure 4.2: (a) Color-filled contours of 0–1-km SRH (m^2 s^{-2}) at 2100 UTC 31 May 2013 for d02 of CTRL. County and state boundaries are outlined in gray. State and county boundaries are outlined in gray. (b) Same as (a), but for 0–3-km SRH. (c) Mesoscale conditions at 2100 UTC 31 May 2013, just prior to convective initiation, taken from d02 of the CTRL run. Color-shaded contours of SBCAPE (J kg^{-1}), dash-filled contours of SBCIN (J kg^{-1}), as well as 10-m (black), 850 mb (red), and wind speed (kts), wind barbs (kts). The 20 °C line is contoured in brown as an approximation for location of the dryline and stationary front. (d) Shaded contours of maximum cloud coverage (%) in the lowest 5 km and contours of 35 dBZ at −10 °C in orange. State and Oklahoma county boundaries are outlined in red.

imately 2135 UTC (Fig. 4.4a), and roughly an hour later a hook echo forms. The hook echo is accompanied by a concentrated region of large values of 2–5-km updraft helicity (UH; e.g., Kain et al. 2008), which indicate mesocyclone location (Fig. 4.4b). Also around this time, a cell forms on the north flank of

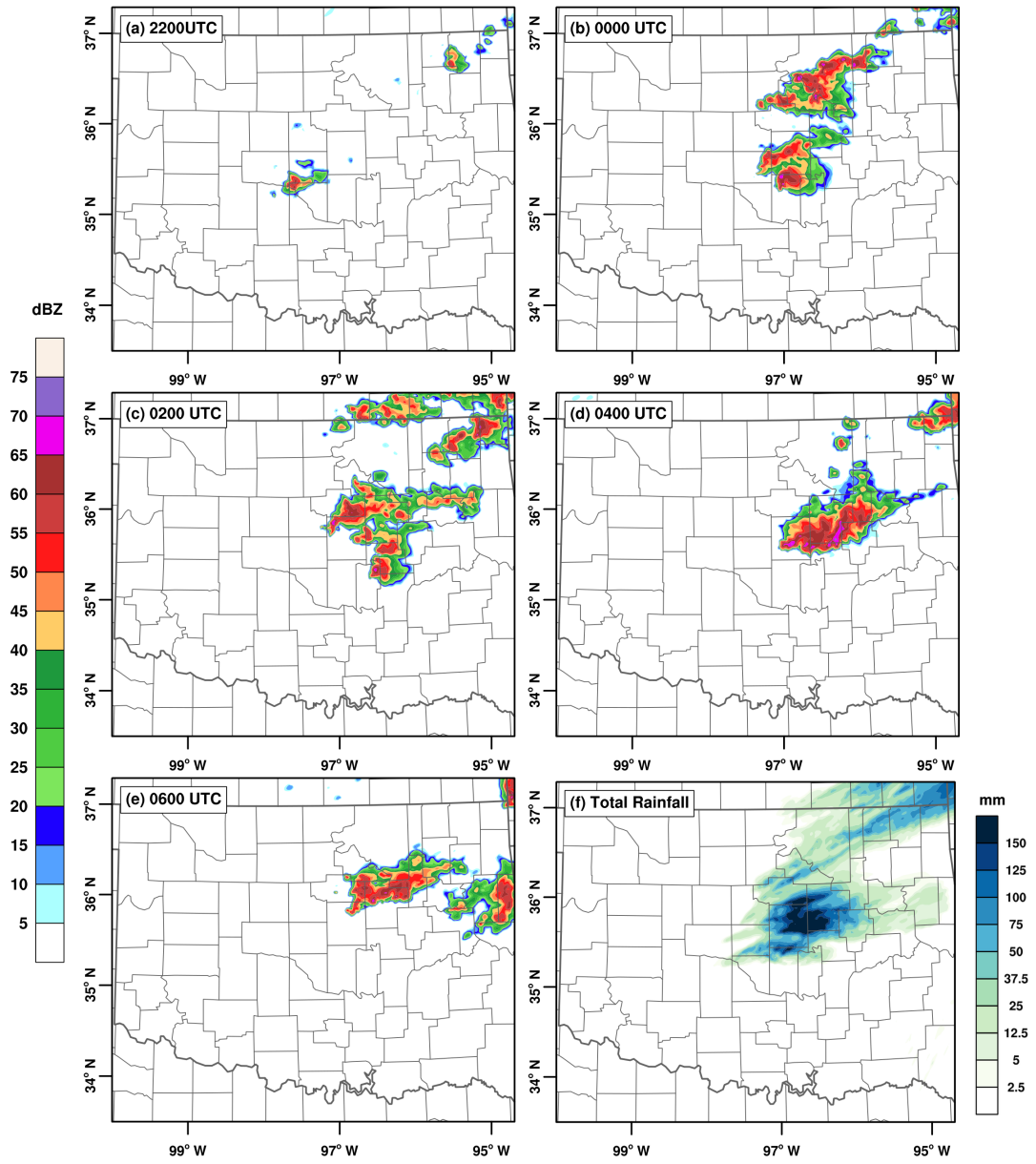

Figure 4.3: Color-filled contours of simulated reflectivity (dBZ) at 1-km AGL from d02 of the CTRL simulation at (a) 2200, (b) 0000, (c) 0200, (d) 0400, and (e) 0600 WRF CTRL d02 simulated REFL at 1 km. (f) Filled contours of d02 CTRL rainfall accumulated from 2100–0600 UTC, State and county boundaries are outlined in black.

the parent supercell. When this cell moves north and away from the main storm, around 2300 UTC, the hook echo becomes more defined and the area of large UH values grows (Fig. 4.4c). Around 2345 UTC (Fig. 4.4d), the initial mesocyclone

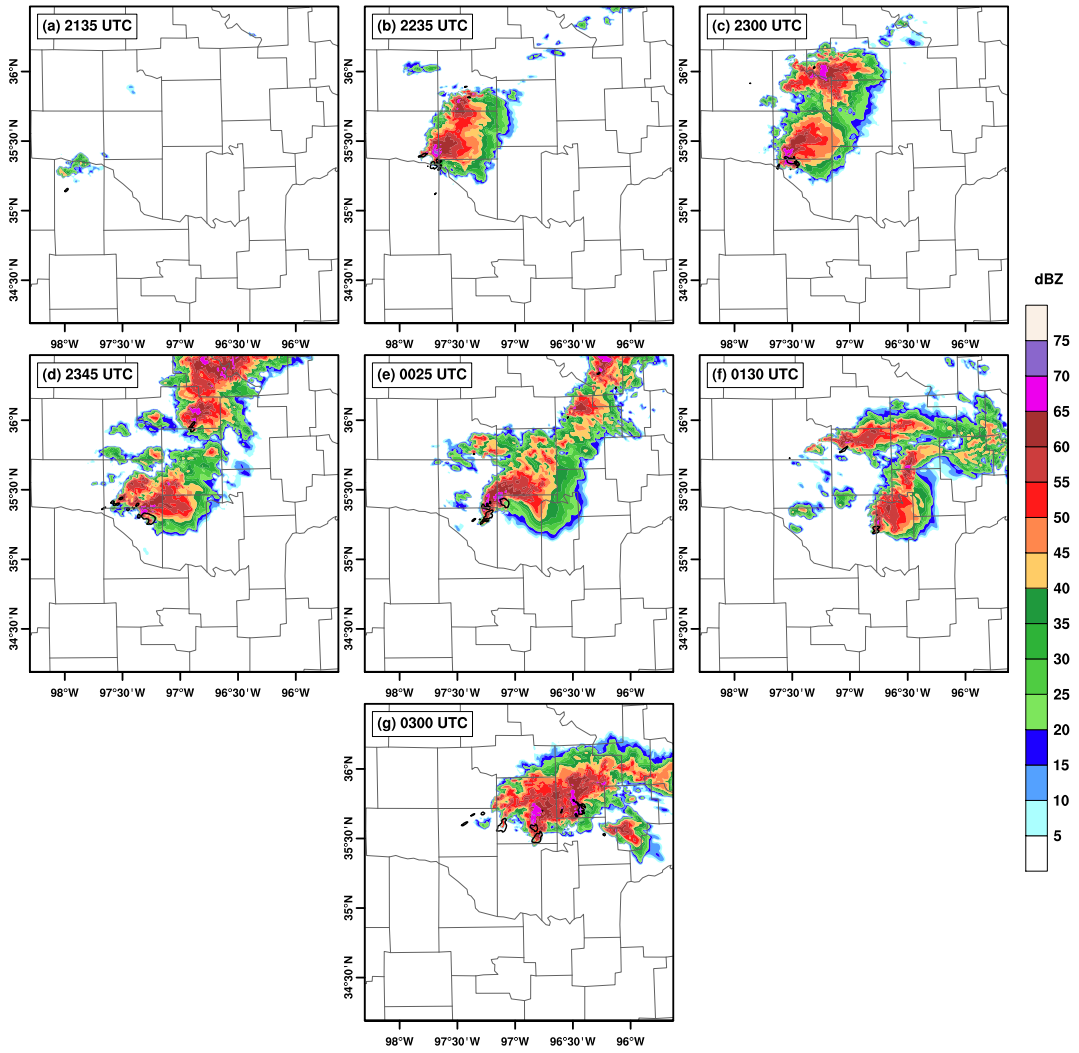

Figure 4.4: Color-filled contours of simulated reflectivity (dBZ) at 1-km AGL and contours of 800 m^2s^{-2} 2–5-km UH (black) from d03 of the CTRL simulation at (a) 2135, (b) 2235, (c) 2300, (d) 2345, (e) 0025, (f) 0130, and (g) 0300 UTC. Oklahoma county boundaries are outlined in gray.

begins to cycle, with a new mesocyclone forming to its west. Additionally, a new cell forms just to the west of the main supercell. This flanking cell strengthens and develops a mesocyclone, eventually undercutting the initial supercell, thus becoming the dominant mesocyclone (Fig. 4.4e). Approximately an hour later, the storm begins to weaken (Fig. 4.4f), and it is almost completely dissipated by 0300 UTC (Fig. 4.4g).

The resulting mesocyclone tracks, computed using a 3D object-tracking algorithm similar to that used by Clark et al. (2012a), depict a complicated evolution as the first supercell moves eastward and is undercut by the second supercell (Fig. 4.5). Mesocyclone tracks, computed similar to the method used by Clark et al. (2012b) indicate that the CTRL storm generally tracks in an easterly direction over its lifetime (Fig. 4.5), moving more south-southeast between 2300 and 0100 UTC (Fig. 4.5b). Near-surface wind speed (Fig. 4.5a) is strongest for the initial

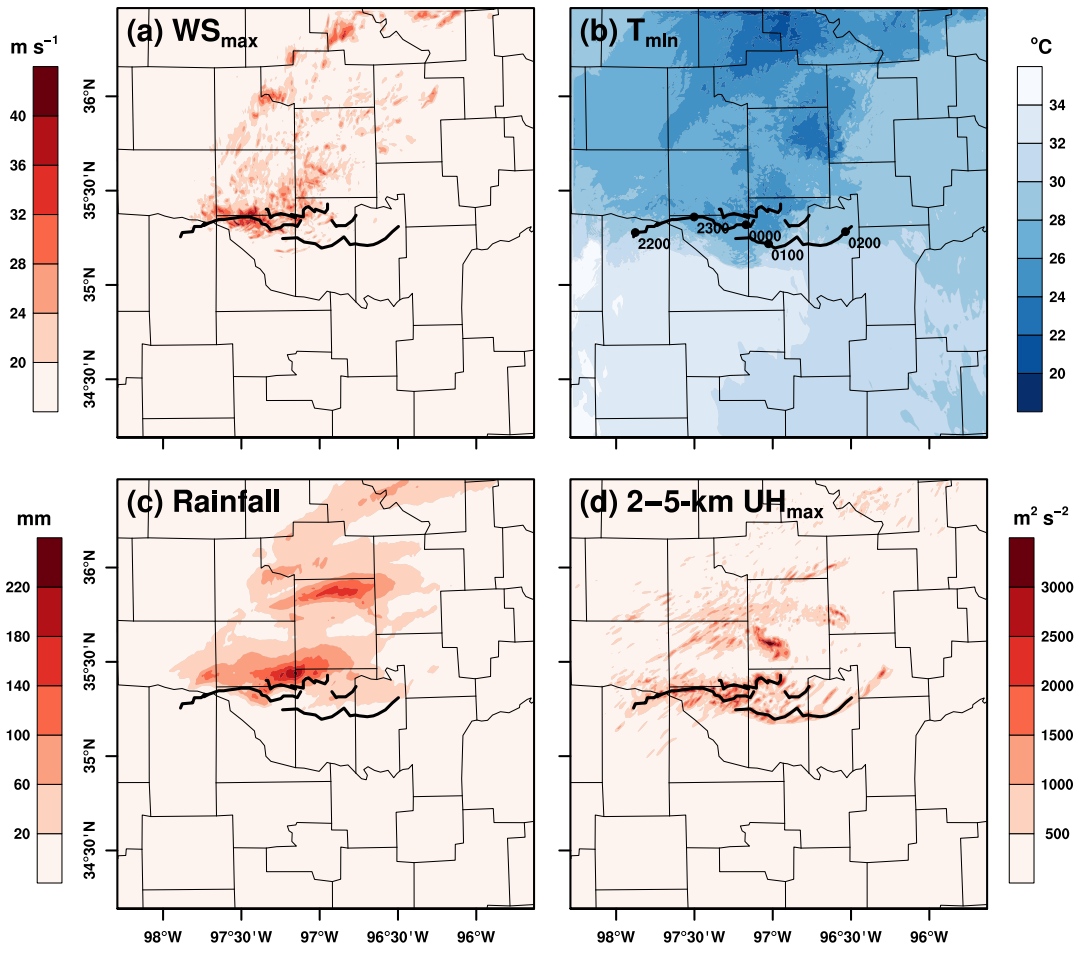

Figure 4.5: Color-filled contours of CTRL d03 time composite (a) maximum near-surface wind speed, (b) minumum near-surface temperature, (c) total rainfall, and (d) maximum 2–5-km UH. Mesocyclone track lines are in black, and the location of the storm at every hour (UTC) is noted in (b) with dots and time labels. Oklahoma counties are outlined in black.

mesocyclone track, with speeds exceeding 35 m s^{-1} in some locations. However, 2–5-km UH remains high for much longer in the storm's lifetime (Fig. 4.5d) until the mesocyclone weakens and takes a more northerly track, beginning just after 0100 UTC. Rainfall is mainly concentrated north of the first track (Fig. 4.5c), as are the cooler near-surface temperatures accompanying the rain-cooled downdraft (Fig. 4.5b).

Time series tracks of mesocyclone-averaged 0–1-km and 2–5-km updraft helicity (Fig. 4.6b) suggest that mid-level mesocyclone strength is greatest from 0000–0130 UTC, as indicated by plateaus of 3-km ζ_{avg} and 2–5-km UH at $\sim 0.02 s^{-1}$ and ~ 4000 m^2 s^{-2}, respectively. While first-model-level ζ_{avg} is also elevated over this time, low-level mesocyclone strength, as determined by 0–1-km UH, is only relatively strong from $\sim 0000-0003$ UTC. The southern-most mesocyclone track starts around this time (Fig. 4.5b), suggesting that the low-level mesocyclone associated with this track is not as strong.

4.2.2 Pre-storm urban environment

It is important to establish that the model is producing reasonable atmospheric urban effects before analyzing any differences in storm strength and evolution among the 108 different urban runs. To illustrate this point, mean differences are shown between simulation x240.y183 (Fig. 4.1c,d) and CTRL in the hour prior to storm initiation ($2030-2130$ UTC; Fig. 4.7). While the magnitudes of these urban effects are not identical across all urban runs, the general nature of the changes remains consistent across all runs, hence pre-storm urban effects are only shown from this simulation.

Near the ground, the urban area is generally warmer (Fig. 4.7a) and drier (Fig. 4.7b) than CTRL, consistent with UHI theory and the replacement of natural with non-evaporative urban surfaces (e.g., Barlow 2014). This warm,

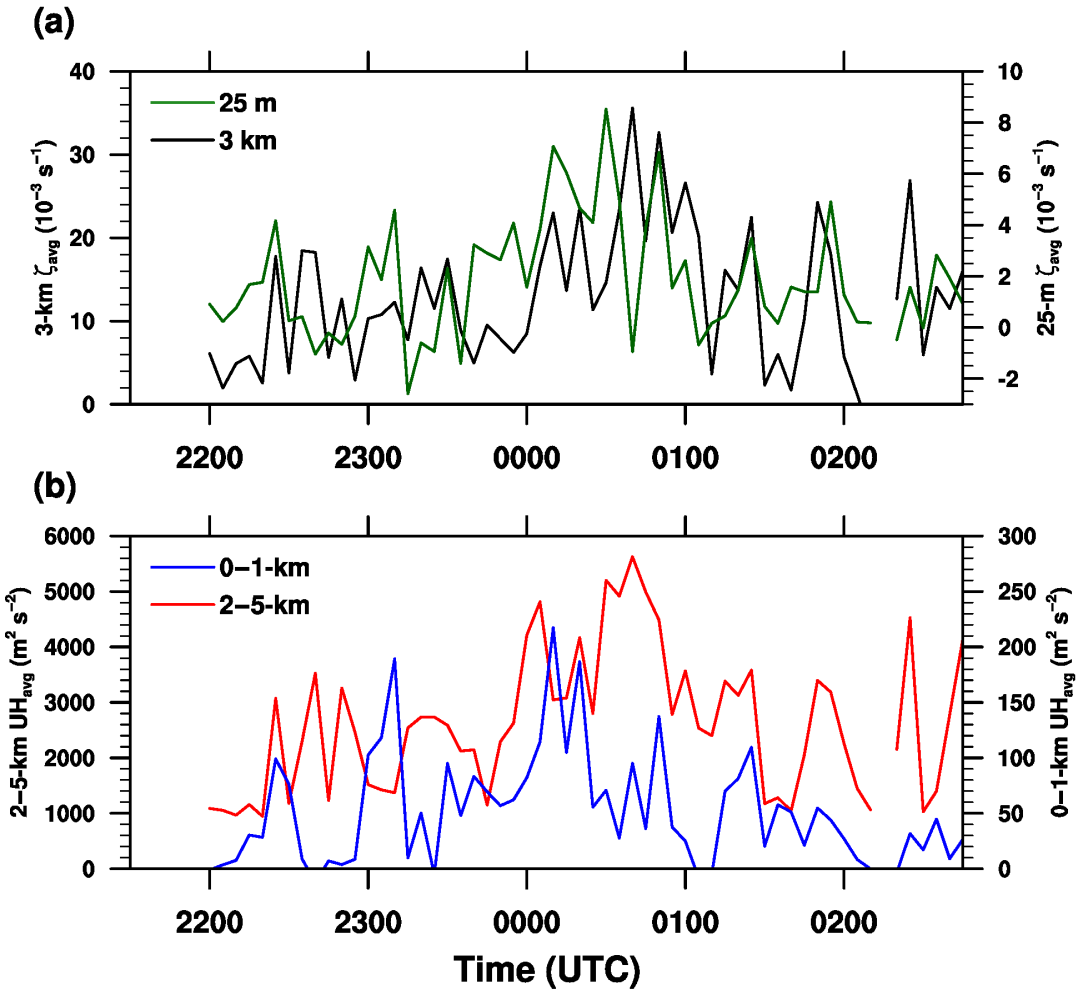

Figure 4.6: CTRL variables averaged over mesocyclone area as a function of time. (a) Vertical vorticity, ζ, at 25 m and 3 km AGL, in black and green, respectively, and plotted against the right and left axes, respectively. (b) 2–5-km UH from 0–1-km in blue and red, respectively, and plotted against the right and left axes, respectively.

dry air also is advected downwind (north and east) of the city. The rough urban surface begets wind speeds that are at least 1.5 m s^{-1} slower than in the CTRL run (Fig. 4.7c), or an approximate 20% decrease, over and downwind of the city. Wind speed decreases of this magnitude have been observed and simulated by previous studies (e.g., Hu et al. 2016, RS17). Winds generally back in the wake of the city (Fig. 4.7d) by 10–15°, however a narrow band of equally veered

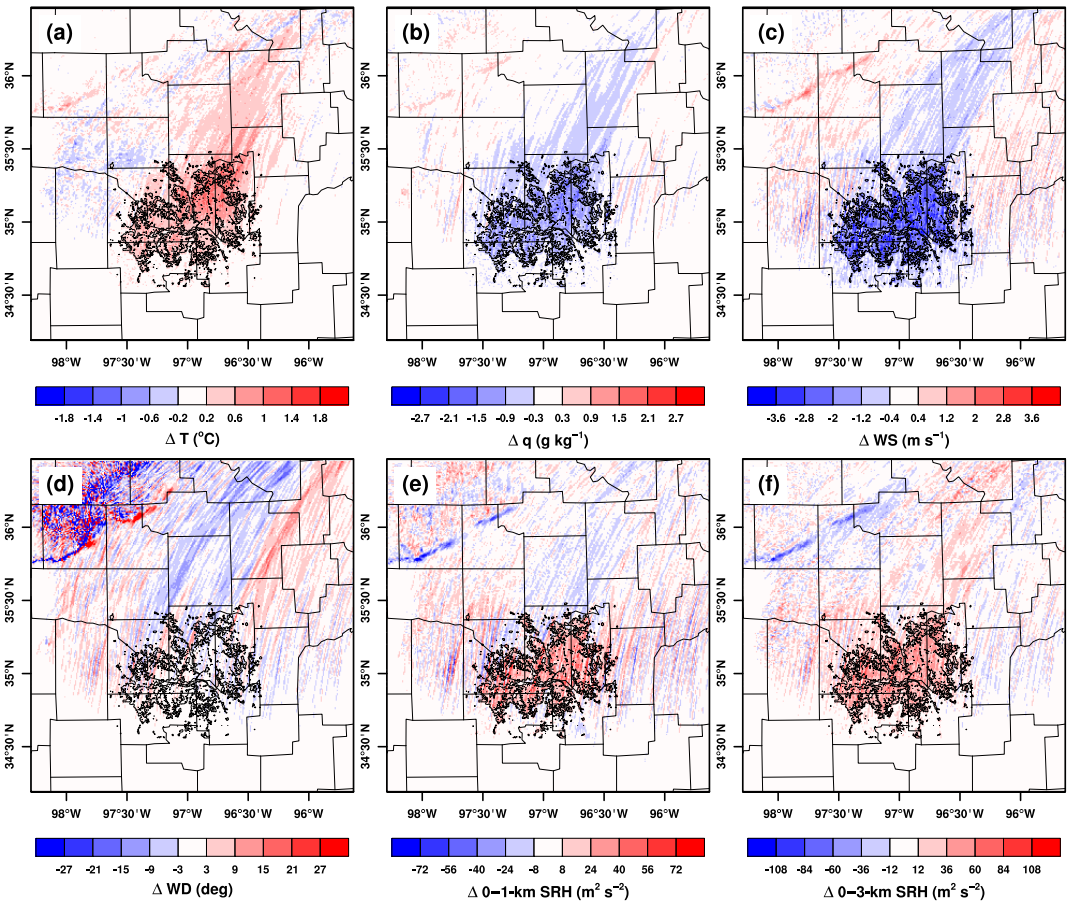

Figure 4.7: Color-filled contours of the 2030-2130 UTC average difference from CTRL of x240.y183 (a) first-model-level temperature (°C), (b) first-model-level mixing ratio, q (g kg^{-1}), (c) first model-level wind speed (m s^{-1}), (d) first-model-level wind direction (degrees),(e) 0–1-km SRH (m^2 s^{-2}), and (f) 0–3-km SRH. Urban fraction of 0.1 is contoured in a thick black line. County boundaries are outlined in gray.

winds exists downwind of the eastern edge of the city. As a consequence of slower near-surface winds, 0–1-km and 0–3-km SRH are $\sim 40-60$ m^2 s^{-2} higher in the vicinity of the urban area, increasing SRH by $\sim 50\%$ and $\sim 25\%$, respectively (Fig. 4.7e,f). As all of these results are generally consistent with theory and observations, we can be confident that the model is simulating reasonable urban-atmosphere interactions.

4.2.3 HCA of DFW simulations

The hierarchical clustering algorithm from Section 2.5 was used on various measures of storm strength and evolution, and the results will be discussed here. Generally, the members in each 2–5-km UH HCA group (Fig. 4.8) do not have

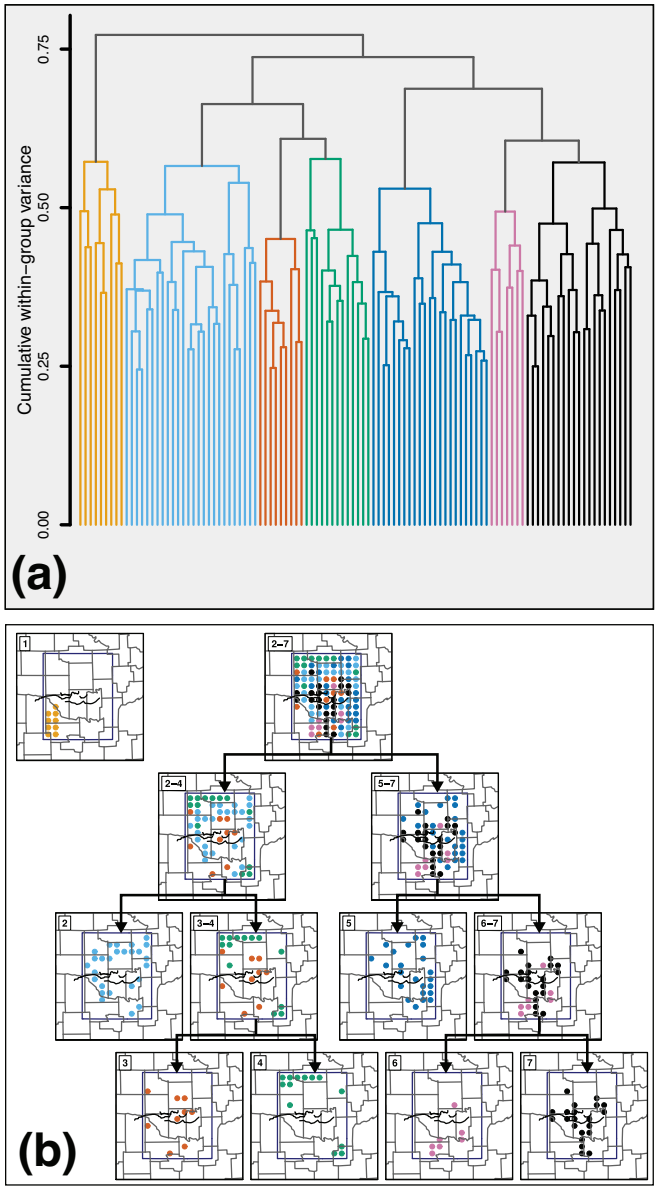

Figure 4.8: (a) Dendrogram of 2–5-km UH HCA results and (b) the resulting city-center locations by group. Oklahoma county boundaries are outlined in gray. Colored dendrogram groups in (a) correspond to similarly-colored dots in (b).

city locations that are geographically collocated. Likewise, member city locations are similarly scatted in the HCA results for rainfall (Fig. 4.9). These findings suggest that city location is not the primary reason for member differences in 2–5-km UH and storm-total rainfall.

In contrast, the HCA results for 0–1-km UH (Fig. 4.10), near-surface wind speed (Fig. 4.11), and near-surface temperature (Fig. 4.12) suggest that differ-

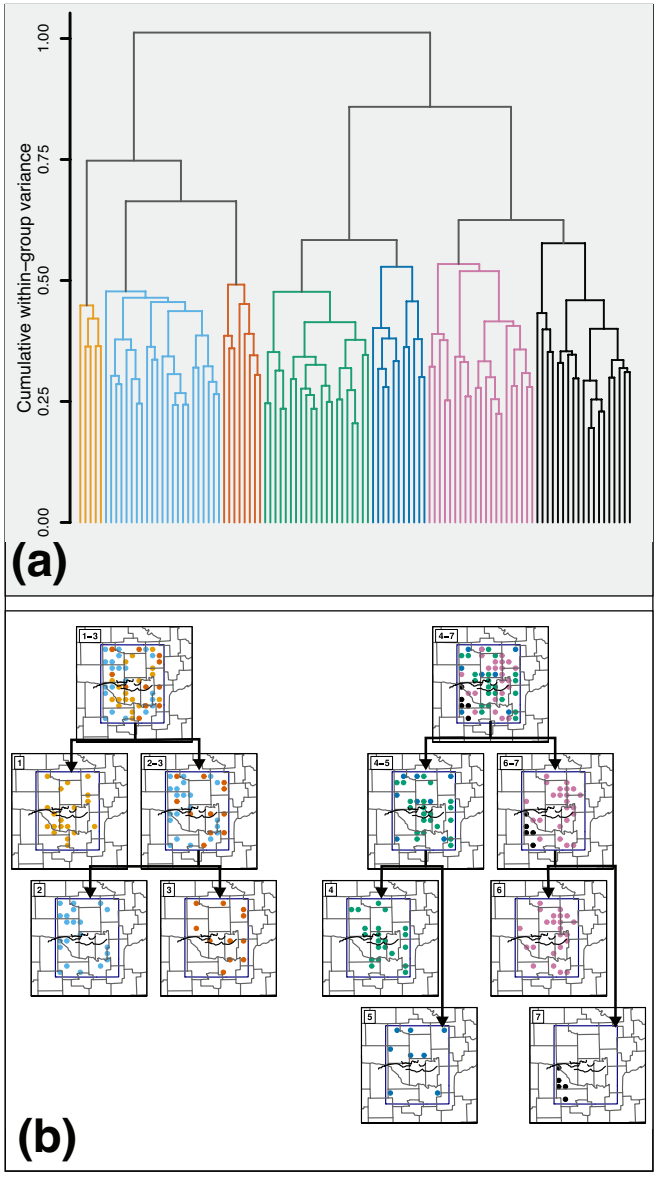

Figure 4.9: Same as Fig. 4.8 but for storm-total precipitation.

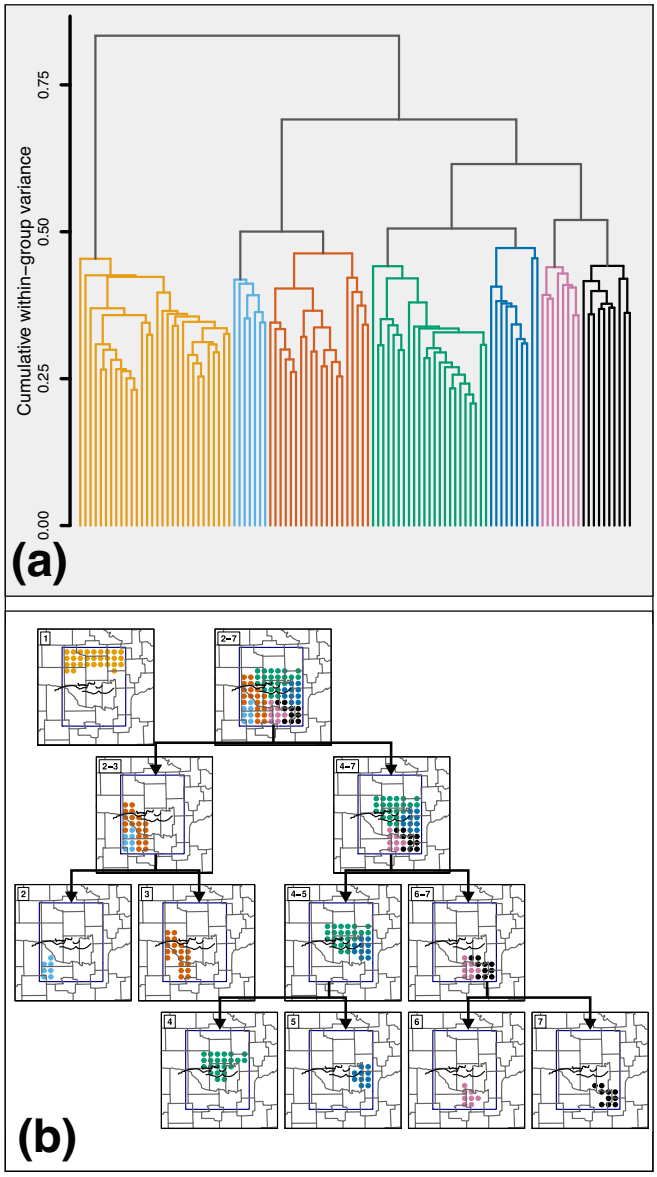

Figure 4.10: Same as Fig. 4.8 but for 0–1-km UH.

ences in low-level storm characteristics are dependent on city location. At the highest grouping (i.e., groups with the greatest within-group variance), members with city centers south of and directly under the storm path (e.g., group 2–7 in Fig. 4.10) are grouped separately from those with centers north of the storm path (e.g.,group 1 in Fig. 4.10). Below that, each group generally bifurcates into eastern and western groups (e.g., groups 2–3 and 4–7 in Fig. 4.10), followed

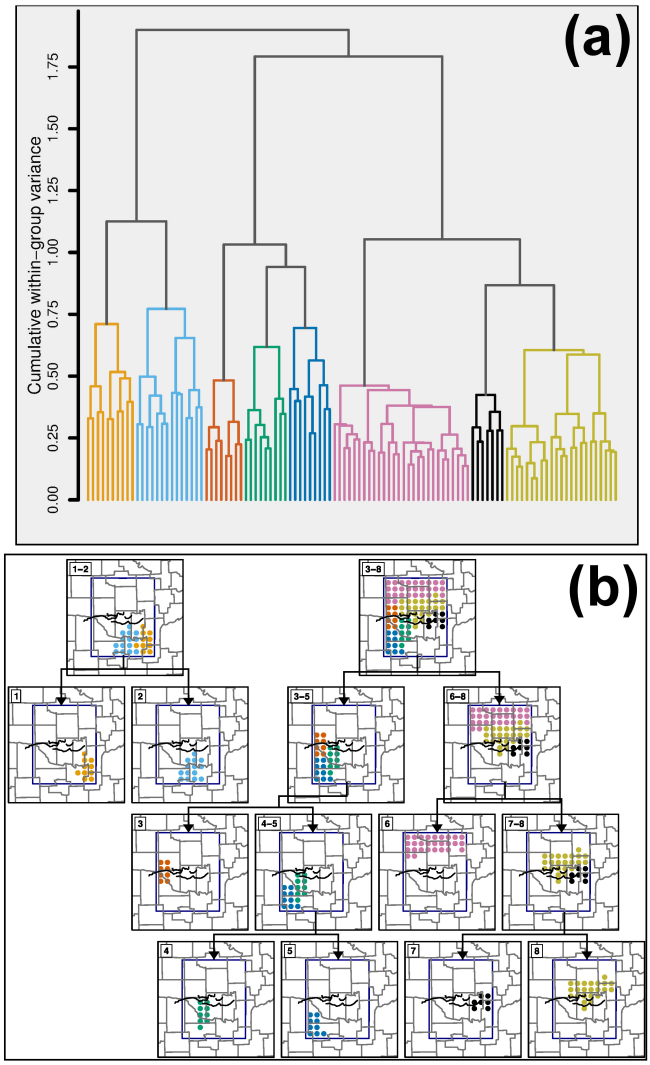

Figure 4.11: Same as Fig. 4.8 but for low-level wind speed.

by another set of north-south and (in some cases) east-west splits. The members group first (e.g., the bottom-most groups) by east-west city location, and then subsequently by north-south location, suggesting that members with similar east-west locations are generally more alike than those with similar north-south locations.

While the HCA groupings for 0–1-km UH, near-surface wind speed, and near-surface temperature are generally similar, some noticeable differences do exist. For example, in the 0–1-km UH groupings, simulations with city locations in

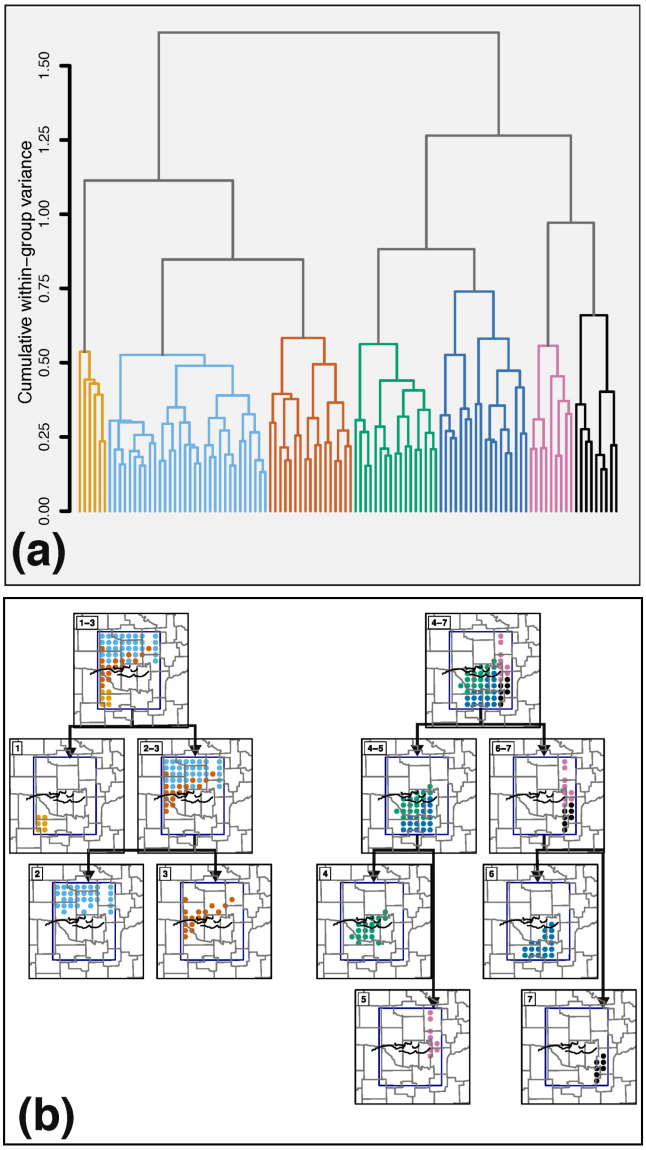

Figure 4.12: Same as Fig. 4.8 but for low-level temperature.

the northern third of the domain (group 1 in Fig. 4.10) are quite different from those in the southern two-thirds of the domain (groups 2–7), as indicated by the large increase in within group variance (> 0.25) when group 1 is combined with the rest. A similarly large increase in variance (≈ 0.5) occurs when the group of northern city locations from the low-level wind speed HCA (group 6 in Fig. 4.11) are combined with simulations with city locations in the middle third of the domain (groups 7 and 8). However, variance increases by an even *larger* amount

when groups 6–8 are combined with 3–5 (≈ 0.75). This difference between 0–1-km UH and near-surface wind speed HCA grouping structures indicates that while the final groups may differ little, the order of similarity between the groups can change. The main reason for these differences is that near-surface temperature and wind speeds are modified by the urban area before (and regardless of if) the storm interacts with the city. In other words, temperature and wind speed changes are not directly tied to the presence of the storm, but UH is a property of the storm itself, and not just the underlying surface. Hence, it is possible that the HCA groupings for near-surface variables are dominated by non-storm modifications of the near-surface environment.

To understand how the various groups differ, we can examine difference fields for several variables that are related to storm strength and evolution. The groupings are selected from a single HCA result to simplify interpretation. Since the HCA results of 0–1-km UH, near-surface temperature, and near-surface wind speed each provide grouping structures that are nearly identical, selecting the groups from any of these three variables should provide similar results. Hence, we will analyze difference fields based on the groupings from the 0–1-km UH HCA. Furthermore, to avoid representativeness issues caused by small sample size or large within-group variance, the 4 groupings with merging heights of ~ 0.5 (Fig. 4.10a) will be examined. These groupings, or groups 1, 2–3, 4–5, and 6–7 in Fig. 4.10, will be referred to as the N, SW, E, and SE groups, where the directional names correspond to the location of the city relative to the general storm track in each group.

Regardless of city location, all simulations with an urban area generally have greater low- and mid-level UH than the CTRLE simulations (Fig. 4.13) along the southern-most mesocyclone track (Fig. 4.7). This difference is most pronounced and consistent when the city center is in the southern and eastern portions of

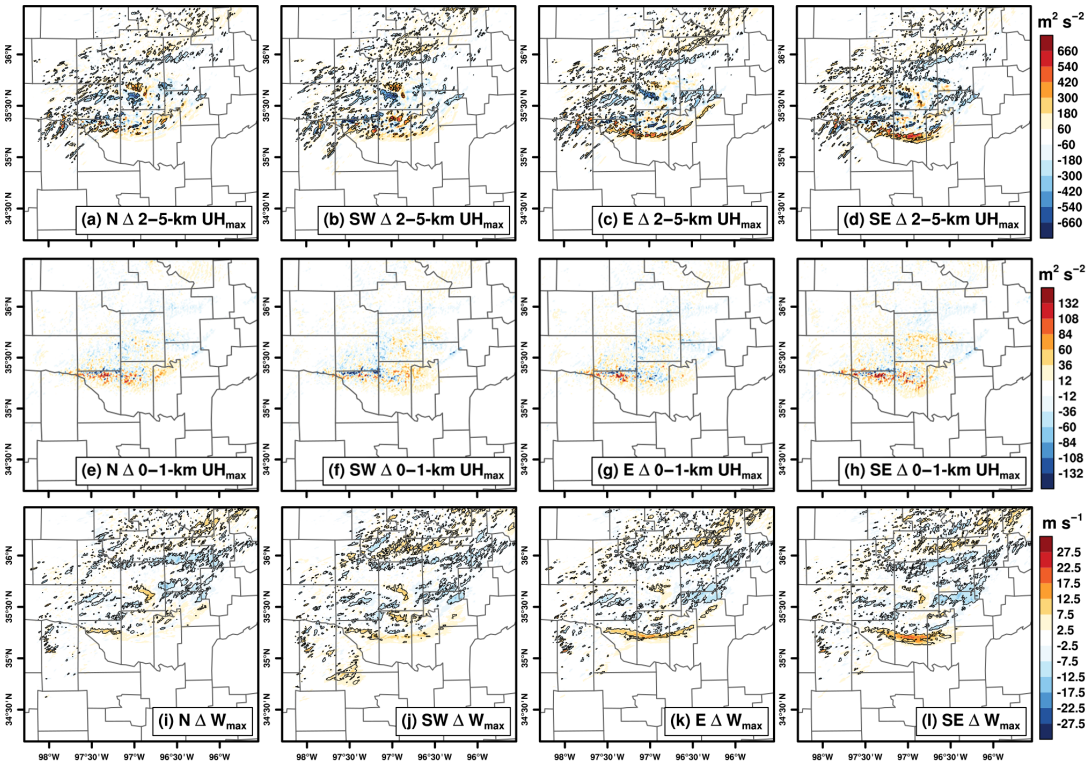

Figure 4.13: (a) Color-filled contours of group-averaged differences of group N from CTRL in time-composite maximum 2–5-km UH. Also, contoured in black are differences that are significant at $\alpha = 95\%$, as computed from permutation testing with 10,000 permutations. Oklahoma counties are outlined in gray. (b)–(d) Same as (a), but for groups SW, E, and SE, respectively. (e)–(h) Same as (a)–(d) but for 0–1-km UH.
n

the domain (groups SW, E and SE; Fig. 4.13b–d,f–h). However, UH values near the initial, western-most mesocyclone are diminished by the presence of the city to the south, particularly in the SW group (Fig. 4.13b,f). Some of these apparent differences in mesocyclone strength can explained by a more southerly storm track in the SW, E, and SE groups (Fig. 4.14). The more southerly track of the mesocyclone is clear when comparing reflectivity and 2–5-km UH contours of one member from these groups (x327.y156) to a CTRLN simulation (Fig. 4.15). However, if the mesocyclones simply track further south, but are of similar strength, we should in each case see an additional swath of nearly equal

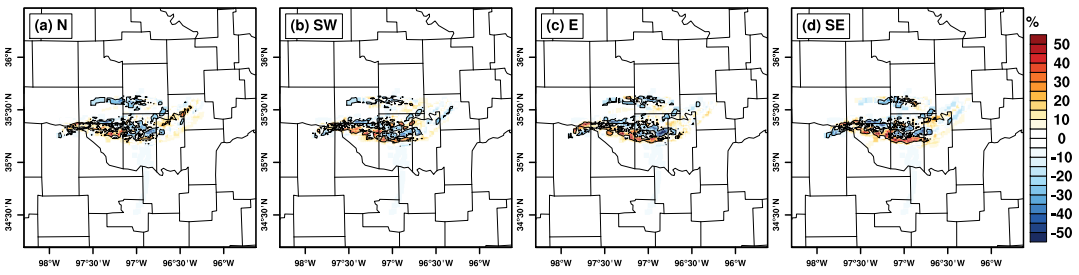

Figure 4.14: Color-filled contours of differences between groups and CTRLE of the percentage of members in each group that have a mesocyclone track in a 3x3 box centered at each grid point. Contours of differences that are significant at $\alpha = 95\%$ are contoured in black. Oklahoma counties are outlined in gray.

magnitude UH change, but of opposite sign. In the case of both the increased UH values of the southern-most storm track for groups SW, SE, and E (Fig. 4.13b–d,f–h), as well as the decreased UH near the initial mesocyclone in the SW group (Fig. 4.13b–d,f–h), this kind of pattern is not present. This indicates that the strength of the southern-most mesocyclone is indeed increased, and significantly so in the E and SE groups, while the initial mesocyclone is weakened significantly in the SW group.

The most prominent, low-magnitude signals in minimum near-surface temperature (Fig. 4.16a–d) and maximum near-surface wind speed (Fig. 4.16e–h) group differences from CTRLE are first order effects of the urban area. Over and downwind of the general location of the urban areas in each group, maximum wind speeds are slower while minimum temperatures are higher, caused by increased friction and the UHI effect, respectively. These effects are particularly evident for the SW (Fig. 4.16b,f) and SE (Fig. 4.16d,h) groups, where the city locations are furthest from precipitation effects.

Temperature and wind speed differences also are apparent near the storm. The minimum temperature south of the southern-most mesocyclone track, likely within the storm's rear-flank downdraft (RFD), is over 0.5 °C cooler than

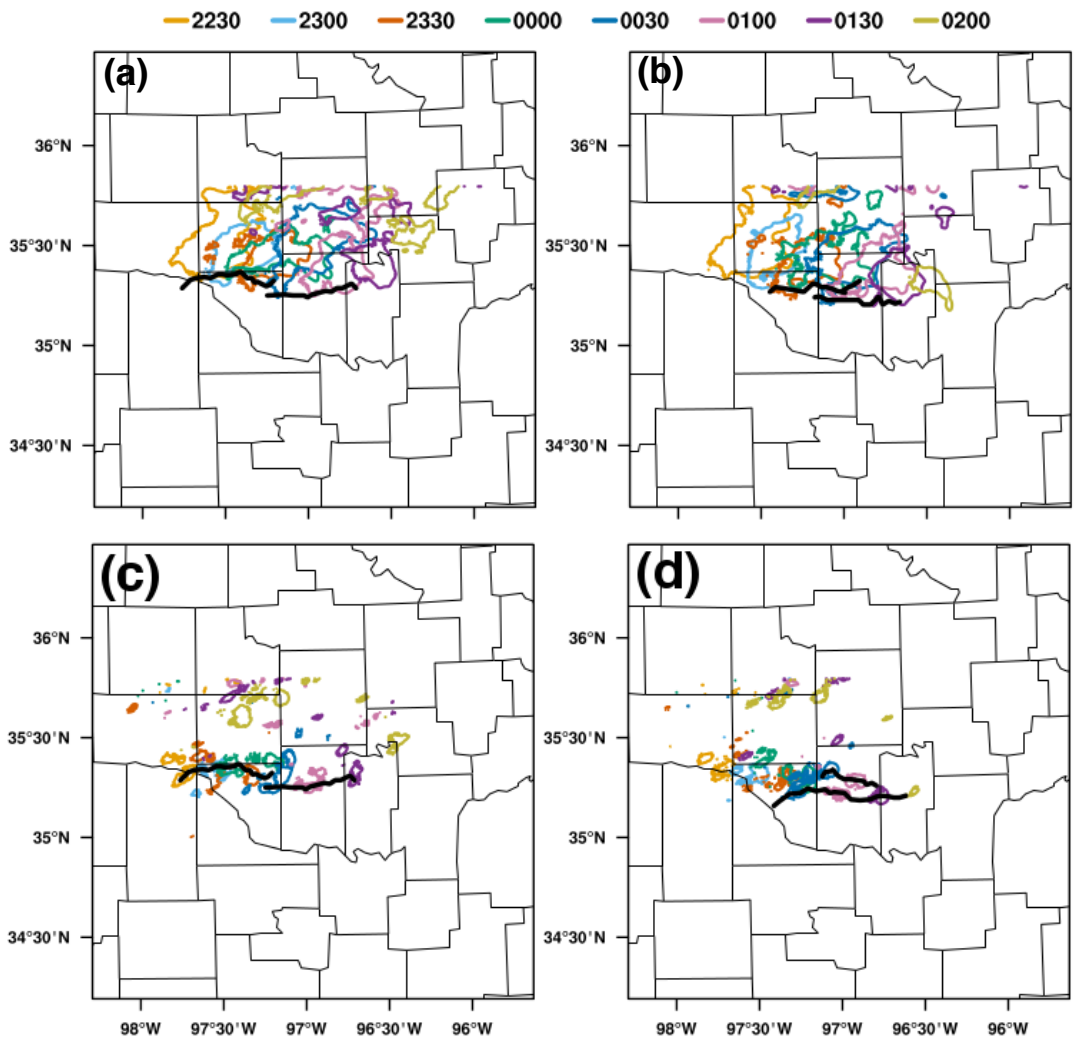

Figure 4.15: (a) Simulated reflectivity from CTRLN member 1 contoured at 45 dBZ at every 30 minutes starting at 2230 UTC. Mesocyclone tracks for the two mesocyclones that achieved the southernmost location are in black. County lines are in gray. (b) Same as (a) but for urban simulation x327.y156. (c), (d) Same as (a) and (b) but for 2–5-km UH contoured at 500 m^2 s^{-2}.

CTRLE for the SW (Fig. 4.16b) and E (Fig. 4.16c) groups. Members in the SE group (Fig. 4.16d). have significantly cooler RFDs with $T_{min} \geq 1$ °C cooler than the CTRLE group. Near-surface wind speeds in the vicinity of the storm are generally higher than CTRLE when the storm passes south of the city (Fig. 4.16e), however in groups SW (Fig. 4.16f) and E (Fig. 4.16g) the urban-induced

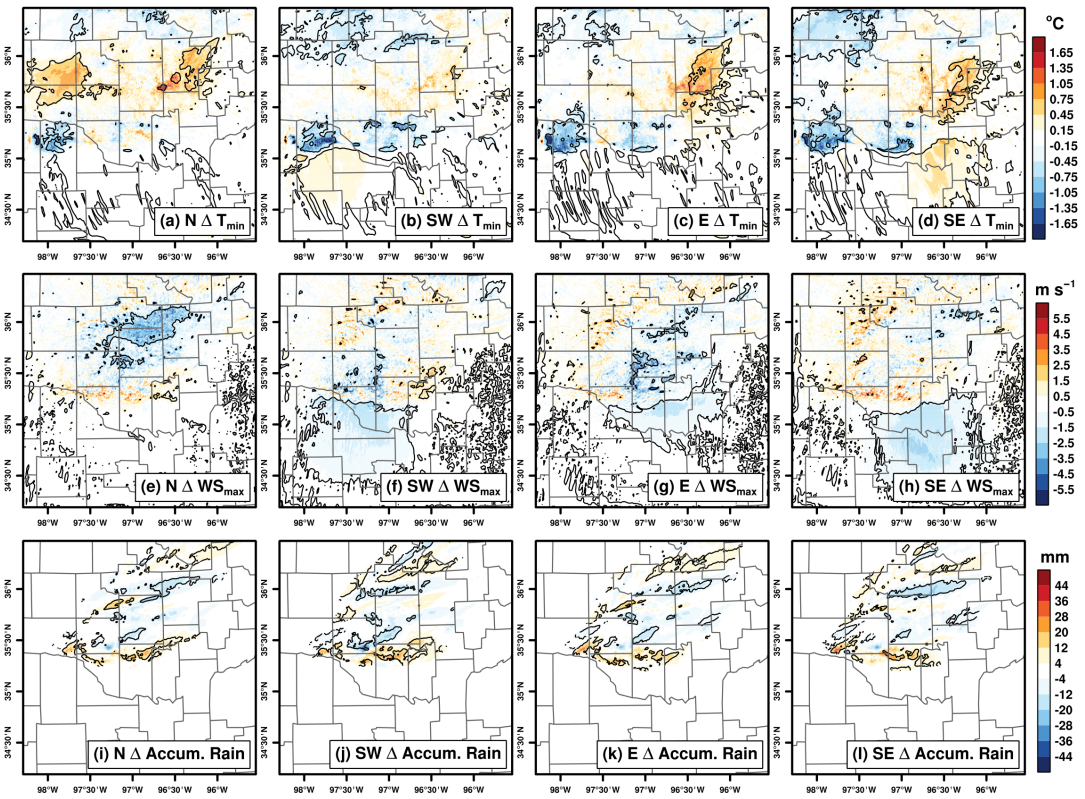

Figure 4.16: Same as Fig. 4.13 but for (a)–(d) difference in time-composite minimum near-surface temperature (T_{min}; °C), (e)–(h) difference in time-composite maximum near-surface wind speed ($\mathrm{WS_{max}}$; m $\mathrm{s^{-1}}$), and (i)–(l) total accumulated rainfall (mm).

friction negates these effects over some portions of the storm track. This is not the case, though, for the SE group (Fig. 4.16h) which experiences stronger near-surface winds over the entire storm track, even when it approaches the urban area, though this increase is only significant in isolated locations. All urban simulations have areas of significant increase in precipitation (Fig. 4.16i–l) particularly near the beginning and end of the storm track. The SW group also has a large region of significantly less precipitation near the midpoint of the storm's tracks (Fig. 4.16).

Evaluating mesocyclone characteristics as a function of time provides insight about timing and strength differences regardless of location within the domain.

Cumulative differences in mesocyclone-average 2–5-km UH of the 4 groups from CTRLE (Fig. 4.17a) supports the observation from Fig. 4.13a–d that the all urban runs have generally higher 2–5-km UH than CTRLE, particularly for the southern-most mesocyclone (which forms around 0025 UTC; Fig. 4.4e) and for the SE group. This difference is particularly evident in the peak for the SW, E, and SE groups from 0000–0100 UTC, which is strongest for the SE group. However, while the SW, E, and SE groups' mesocyclones are weakening in comparison to CTRLE near the end of the simulation ($\sim$ 0200 UTC), those in the N group begin to strengthen. Though they are in line with earlier analyses, these modifications to mid-level mesocyclone strength are small ($\sim 2-3\%$) compared to mesocyclone strength in CTRLE. Low-level mesocyclone strength (Fig. 4.17b) and near-surface vertical vorticity (Fig. 4.17c) for the N group follow a similar strengthening trend near the end of the simulation, accumulating approximately 30% more 0–1 UH than the CTRLE group by the end of the simulation. Although not categorized by a strong CTRLE-relative strengthening trend near the end of the simulation, the E and SE simulations end with $\sim$ 20%

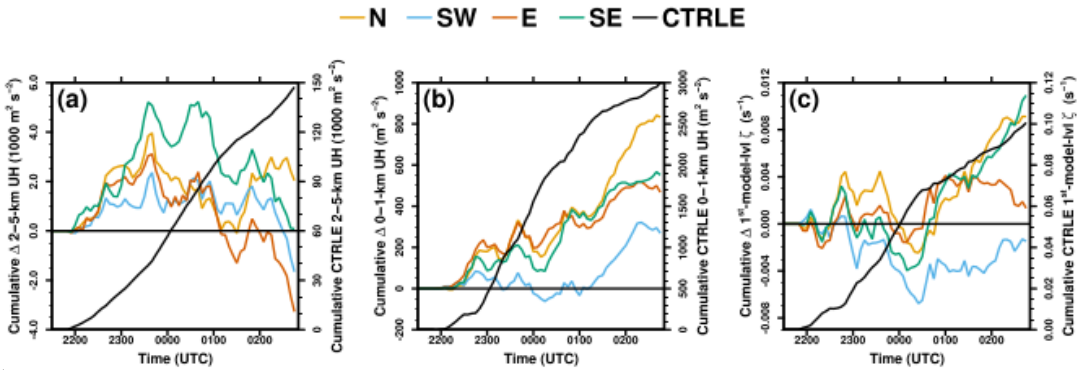

Figure 4.17: Cumulative CTRLE group average (black) and accumulated difference from CTRLE of N (yellow), SW (blue), E (red), and SE (green) groups of mesocyclone-average (a) 2–5-km UH, (b) 0–1-km UH, and (c) first-model-level ζ as a function of time.

more accumulated 0–1-km UH and $\sim$ 10% greater accumulated near-surface vertical vorticity, with these accumulated differences acquired steadily over the entire lifetime of the storm. Across these measures of storm strength, the SW group generally has the weakest mid- and low-level mesocyclone strength, and correspondingly weak near-surface vorticity, particularly from 2200–0000 UTC, trends that are not apparent from Fig. 4.13.

4.2.4 Storm inflow differences

To diagnose possible inflow differences among the groups that may result in the storm modifications discussed in the previous section, we analyze meridional averages of inflow characteristics as a function of time and longitude, computed over box I in Fig. 4.7 (Fig. 4.18 and 4.19). The western (eastern) half of the inflow region is warmer (Fig. 4.18a–d) and drier (Fig. 4.18e–h) than in CTRLE before the storm passes due to the presence of the city in the southwestern (eastern and southeastern) portion of the domain. These warm and dry conditions result in higher LCL heights (Fig. 4.18i–l) and lower CAPE (Fig. 4.18m–p) near the city location, but these differences are generally neutralized as the storm approaches. Air behind the CTRL track is also cooler for the SW, E, and SE groups (Fig. 4.18b–d) because of the more southerly track of the mesocyclone in these groups.

Winds are generally slower in the inflow region when the city is south or east of the storm (Fig.4.19a–d). In agreement with the wind direction changes north of the city prior to storm formation (Fig. 4.7d), inflow-region, near-surface winds are generally veered when the city is to the east (Fig. 4.19g) or southeast (Fig. 4.19h) of the storm, but backed when the city is to the southwest (Fig. 4.19f) of the supercell. This is particularly evident during the latter half of the mesocyclone track for the SW group (Fig. 4.19h). These near-surface wind

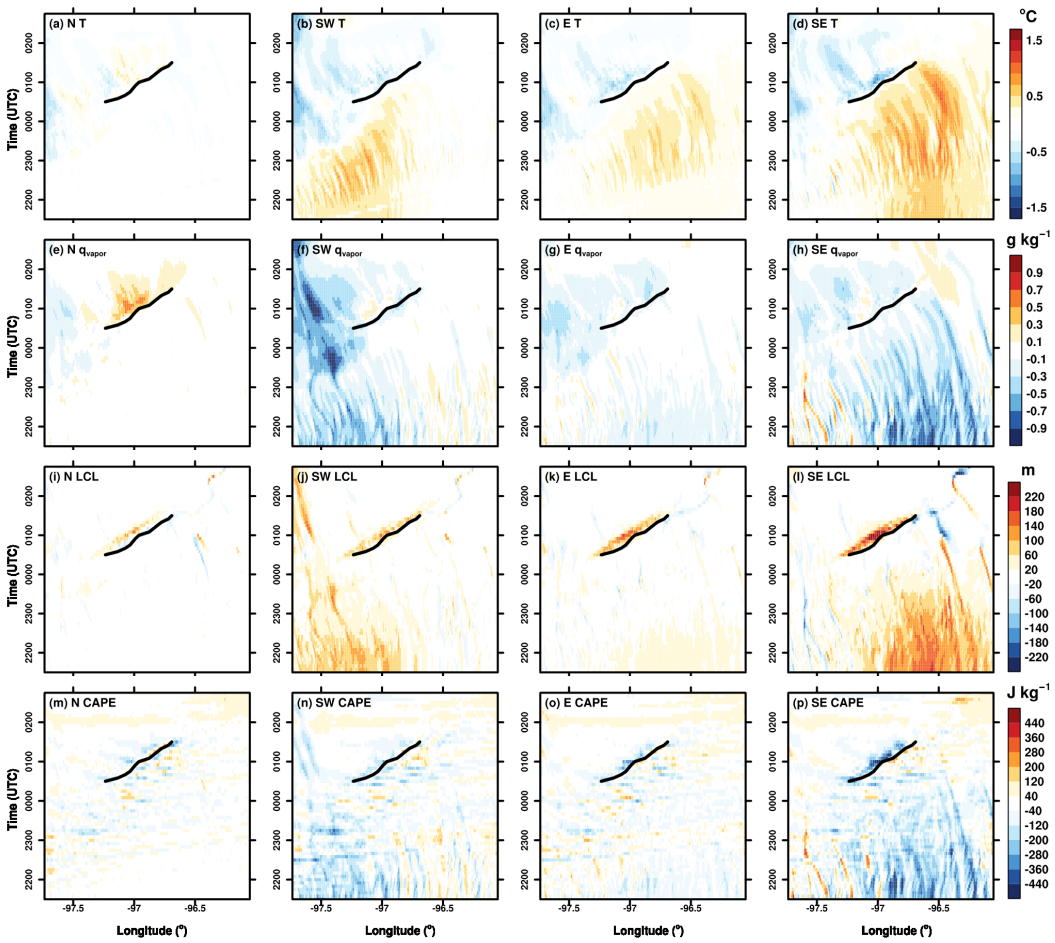

Figure 4.18: (a) Hovmöller diagram of meridionally-averaged first-model-layer differences in group N T (°C) from CTRLE computed over box I (Fig. 4.13e–h), with time (UTC) on the ordinate and longitude (degrees) on the abscissa. The thick black line represents the southern-most CTRL storm mesocyclone track in longitude-time space. (b)–(d) Same as (a) but for groups SW, E, and SE, respectively. (e)–(h) Same as (a)–(d) but for differences in first-model-level water vapor mixing ratio (q; g kg^{-1}). (i)–(l) Same as (a)–(d) but for differences in LCL height (m). (m)–(p) Same as (a)–(d) but for differences in CAPE (J kg^{-1}).

vector modifications result in higher inflow 0–1-km SRH (Fig. 4.19i–l), 0–500-m bulk shear (Fig. 4.19m–p), and first-model-level streamwise vorticity (ζ_{sw}; Fig. 4.19q–s).

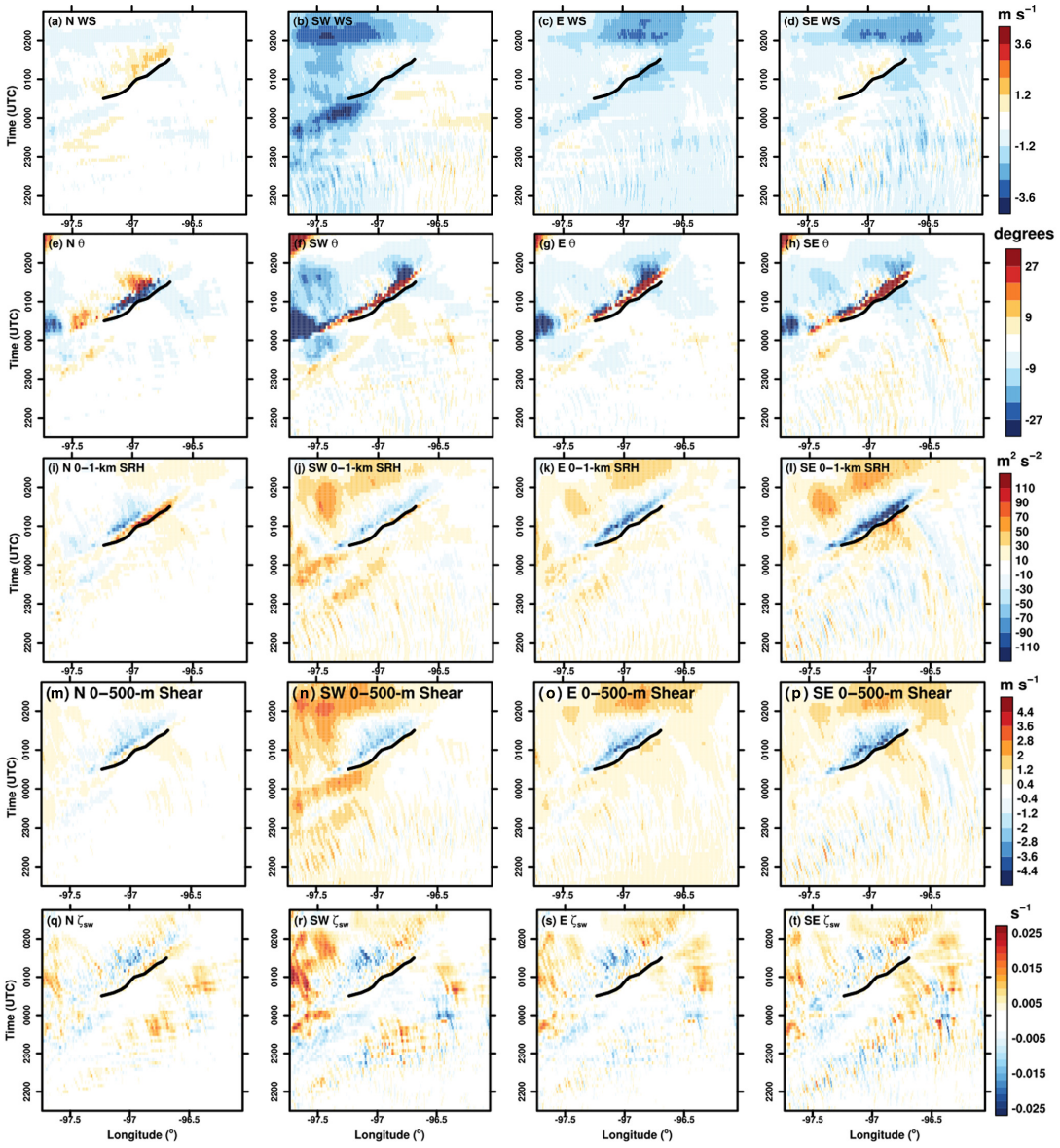

Figure 4.19: Same as Fig. 4.18 but for differences in (a)–(d) first-model-level WS (m s^{-1}); (e)–(h) first-model-level wind direction (θ; degrees); (i)–(l) 0–1-km SRH (m^2 s^{-1}); (m)–(p) 0–500-m bulk shear (m s^{-1}); and (q)–(t) first-model-level streamwise vorticity (ζ_{sw}; s^{-1}).

4.3 Summary and conclusions

In this study, we used the WRF to analyze the effect of a large southern Plains urban area (DFW) on an isolated supercell. To investigate how urban-storm

interactions change with varying city-relative storm tracks, DFW was placed in 108 systematically-chosen locations, resulting in 108 unique simulations. Hierarchical clustering analysis was used to determine which simulation members were most similar to each other, providing groups of simulations which were compared to each other.

HCA analyses indicated that 2–5-km updraft helicity, which indicates mid-level updraft strength, and storm-total rainfall were not statistically dependent upon city location. The latter finding stands in contrast to observational and modeling studies that have found increased rainfall in the vicinity of urban areas under synoptically benign conditions (e.g., Shepherd et al. 2010b; Li et al. 2011; Niyogi et al. 2011), but is in agreement with those that have considered strongly-forced precipitation events (e.g., Yang et al. 2014a). However, HCA of 0–1-km UH, near-surface wind speed, and near-surface temperature showed that lower-level storm characteristics vary with changing city location. Simulations with city locations of similar east-west location generally were more alike than those with similar north-south locations. This order of similarity suggest that low-level supercell characteristics are most sensitive to the north-south location of a city relative to the storm path.

First-order urban effects were clear during the lifetime of the storm in fields of group-mean differences from CTRLE. Results indicated warmer and drier air near the surface over and downwind of the general urban area in each group, and slower near-surface wind speeds in the vicinity of the city. In the SW and E groups, the latter effect also appeared to result in weaker storm-induced wind speeds when the storm traversed the city, though these deviations from the non-urban simulations were not significant.

Indicators of storm strength and evolution were also modulated by the city. Total accumulated rainfall generally increased across all urban simulations, re-

gardless of city location. However, no discernible pattern differences in precipitation changes were evident, echoing the failure of HCA to group simulation rainfall by geographic location of the city relative to the storm. Storm mesocyclones tracks differed significantly from those of the non-urban simulations, tracking further south in simulations where the storm moved over and/or north of the city, especially in the second half of the storm's lifetime. However, this southward deviation was not necessarily accompanied by a stronger mesocyclone, with large swaths of significantly-increased maximum mid-level UH only observed in simulations where the storm interacted with the city late in its life cycle. Low-level updraft strength was also higher in these groups, as well as those simulations with the city to the north of the storm track, though there were few clear spatial differences among these groups.

Time series analyses suggested that mesocyclones of these simulations with city locations to the north, southeast, and east of the storm track also accumulated $\sim 15\%$ more 0–1-km UH than CTRLE by the end of the CTRL supercell's lifetime. While differences between simulations with city locations south and east of the storm stopped accumulating additional 0–1-km UH after this time, those with cities to the north of the main supercell storm continued to accumulate more 0–1-UH after $\sim$ 0200 UTC, and ended with $\sim 30\%$ more accumulated 0–1-km UH. Given that the main supercell in CTRL has nearly dissipated by 0200 UTC, this increase in mesocyclone strength at the end of the simulation is likely associated with the significant increase in mesocyclone tracks east of the eastern-most CTRL track (Fig. 4.7). Accumulated near-surface vertical vorticity in these simulations where the storm tracks south of the city, as well as in those where the storm tracked to the north of the city late in its lifetime, followed a similar increasing trend near the end of the simulation, resulting in $\sim 10\%$ more total accumulated vorticity than in CTRLE. Contrary to these

results, simulations where the supercell tracked north of or over the city early in its lifetime had the smallest increase in mid- and low-level mesocyclone strength, and had weaker near-surface rotation, compared to CTRLE.

Analyses of atmospheric properties in the storm's inflow region indicated warmer, slower near-surface inflow for simulations with city locations to the south of the storm track. The inflow is also more sheared in the lowest 1 km AGL for these simulations. In simulations with the city in the eastern and south-eastern portion of the domain, inflow was also more backed, and had stronger stream-wise vorticity, compared to CTRLE, particularly near the end of the storm track. Although these inflow differences are not robust enough to make direct connections between inflow properties and storm strength, they make a case that warmer, more sheared inflow induced by the city modifies storm-scale strength and processes when the storm tracks north of the city. Further work could involve parcel trajectory analyses to determine exactly how the storm's inflow is modified by the urban area.

Previous studies that evaluate the effect of urban areas on precipitation patterns show that, while the UHI increases precipitation downwind of cities, increased urban surface roughness causes precipitation to bifurcate around the city. In other words, both thermal and roughness properties of the urban are are important in modifying convection. The present work does not evaluate these effects separately, therefore we cannot determine exactly which aspects of the urban area are causing storm modifications. Future work will involve a factor separation approach to address this question. Additional work should also include analyses of the affect of urban aerosols on simulated storms, as studies have proposed that urban aerosols can modulate storm microphysical properties, of which one consequence may be the induction of lightning maxima over and downwind of cities (e.g., Orville et al. 2001; Rose et al. 2008; Kar et al. 2009;

Coquillat et al. 2013; Tan et al. 2016; Kawecki et al. 2016).

Chapter 5

Factor Separation Analysis

The previous chapter indicated that the presence of the city in the vicinity of the supercell changed the storm's strength and evolution, and that these modifications varied based on the city's location relative to the storm path. Storm inflow analyses suggested that the city resulted in a warmer, more sheared inflow when the city was south of the storm, and storms in these simulations had the strongest low-level mesocyclones. However, the simulation configuration in the previous chapter was not designed to determine which of these urban effects (i.e., thermodynamic vs. shear-induced) made the largest impact on the supercell. To investigate this, the present chapter will use a factor separation approach, whereby simulations of the same supercell as in Chapter 4 are run with only roughness aspects of the urban area parameterized, and an equal number of simulations with only thermodynamic properties of the city included, and the results from these various simulations will be compared. For these simulations, four city locations have been chosen from both the SW and E groups (so 8 unique city locations in total) that were used for analyses in the previous chapter. The analyses discussed here will show that urban surface roughness, and interactions between urban surface roughness and thermodynamic properties, play an important role in modifying storm strength and evolution. Also, it will be shown that the individual contributions of the various factors change based on when the storm interacts with the city, hence attribution of storm changes

to the various factors is complicated.

5.1 Simulation configuration

Model configuration (i.e., domain locations, parametrization choices, etc.) is identical to that used in Chapter 4 (Fig. 5.1a). A total of 34 simulations are

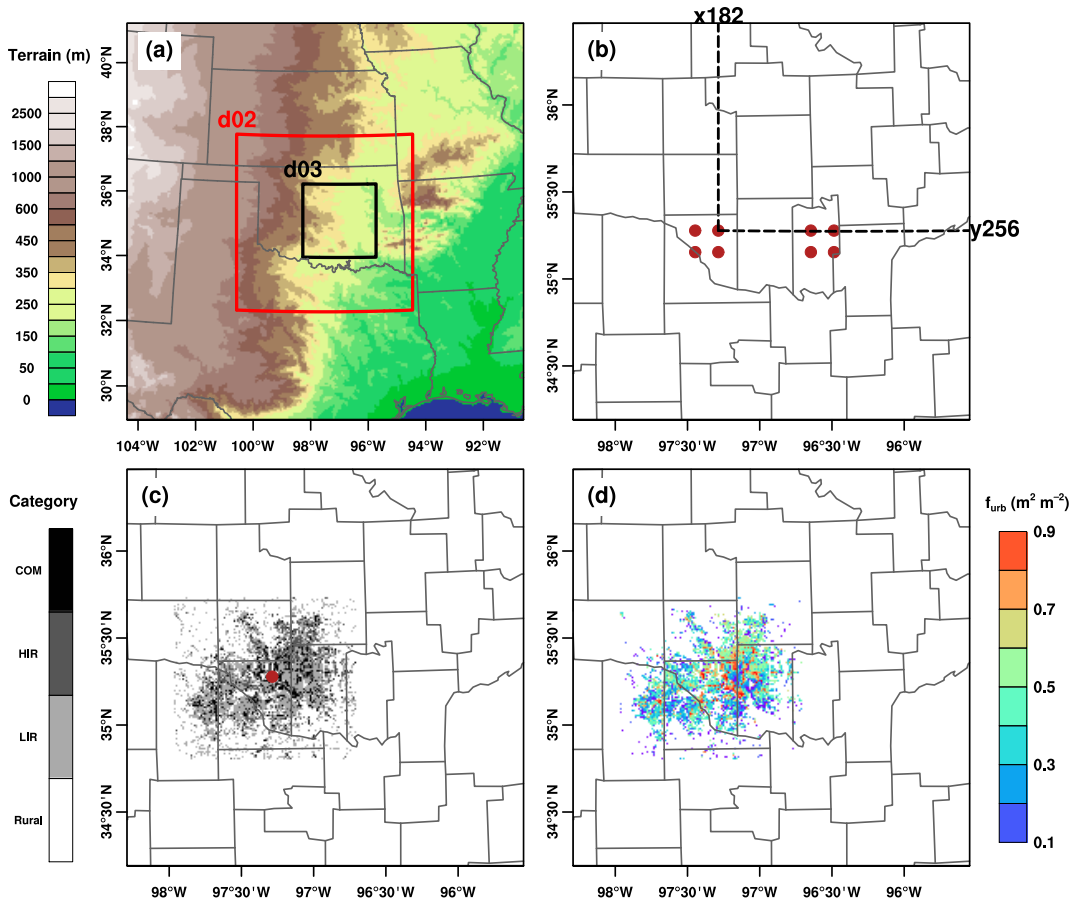

Figure 5.1: (a) Domain locations used for all simulations in Chapter 5. The plotted area is encompassed by d01, and the red and black boxes indicate d02 and d03, respectively. Terrain height is shaded, and state boundaries are in gray. These domain locations are the same as those in Chapter 4. (b) Location of the 8 simulation urban locations (red dots), plotted according to the center of urban fraction mass for each simulation in d03. Oklahoma county lines are in black. (c) Shaded urban land use data for run x182.y256, whose center of mass location (red dot) corresponds to the dashed lines and labels in (b). (d) Same as (c) but for urban fraction.

performed (Table 5.1) with 9 different land use patterns: 10 simulations without any urban areas (CTRLE; same as in Chapter 4), 12 with the LU pattern of DFW located in 4 unique locations in the west-central portion of d03 (West), and 12 additional simulations with DFW in 4 different locations in the east-central portion of d03 (East).

Table 5.1: Names and descriptions of the simulations used in Chapter 5.

Name	# Members	Land Use	Urban Parameterization
CTRLE	10	Grassland Only	N/A
WestF	4	West-central city locations	Full
WestT	4		Thermodynamic only
WestR	4		Roughness only
EastF	4	East-central city locations	Full
EastT	4		Thermodynamic only
EastR	4		Roughness only

For each West and East simulation, three-category urban land use (Fig. 5.1c) and urban fraction (Fig. 5.1d) of DFW, as described in Section 2.1 and used in Chapter 4, are used to represent the various urban areas, while all other areas in d03 remain grassland as in the CTRLE simulations. This land use modification process follows that of Chapters 3 and 4. The 8 urban areas were selected from two separate groups chosen from heirarchical clustering analysis (HCA; Anderberg 1973; Alhamed et al. 2002) in Chapter 4 (4 from each of groups 3 and 8). These groups were chosen as they represent urban-storm interactions during the early (SW) and late (E) stages of the storm's life cycle, and because urban differences from CTRLE were quite different for the two groups. For each DFW land use pattern, 3 simulations are performed with the urban areas parameterized using: the full suite of urban land surface differences from natural vegetation (WestF, EastF); surface roughness only (WestR, EastR); and thermo-

dynamic characteristics only (WestT, EastT). These simulations facilitate the factor separation approach that is the focus of this study.

5.2 Results

5.2.1 Pre-storm Urban Effects

To ensure that the urban-atmosphere interactions are being reasonably simulated, and to frame future discussions of urban effects on a simulated supercell, we will first analyze differences of the West simulations from CTRLE prior to storm formation ($2030-2130$ UTC). Though they won't be explicitly presented, the differences from CTRLE of East are similar to those discussed here for West but displaced to the east.

Increased surface roughness in WestR resulted in $1-2$ m s^{-2} ($\sim 20-40\%$) slower wind speeds over and downwind of the city (Fig. 5.2a) compared to CTRLE, while WestT simulations had slightly stronger winds (~ 0.5 m s $^{-1}$, or $\sim 5\%$) in the urban area (Fig. 5.2b), likely a result of increased turbulence caused by warmer near-surface temperatures (Fig. 5.3b). However, the differences in WestR are much greater in magnitude than those in WestT, and interactions between the two also result in slightly slower wind speeds (Fig. 5.2c), thus effects of surface friction dominate wind speed differences in WestF (Fig. 5.2d). Coherent differences in wind direction directly over the city are not present in any West group (Fig. 5.2e–h), though all but the contribution of the interactions term (Fig. 5.2g) have veering winds downstream of the western edge of the city and backed winds downstream of the city's eastern edge compared to CTRLE. Generally, areas with weaker winds have higher 0–1-km SRH (Fig. 5.2i–l), resulting in $\sim 40-50$ m^2 s^{-2} ($\sim 40-50\%$) more 0–1-km SRH over the city in WestR and WestF.

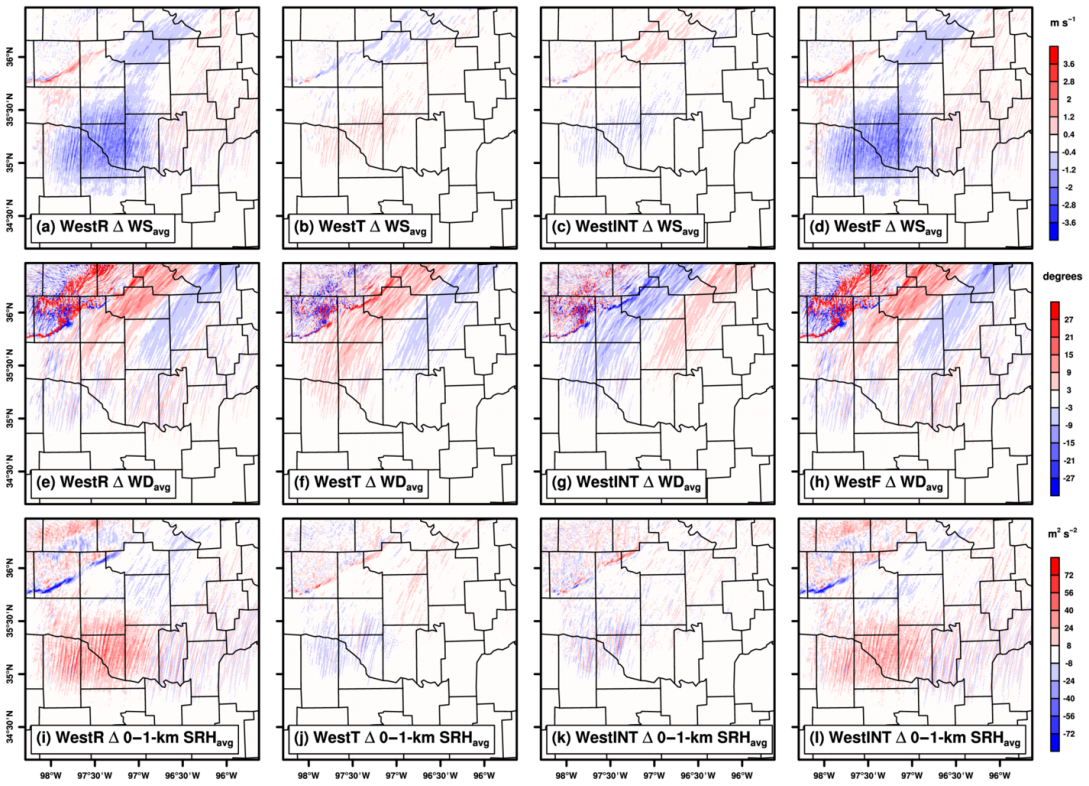

Figure 5.2: (a)–(d) Color-filled contours of the 2030-2130 UTC average difference from CTRL of first model-level wind speed (WS_{avg};m s^{-1}), simulations WestR, WestT, WestINT (i.e. the interactions contribution), and WestF, respectively. Oklahoma counties are outlined in black. (e)–(h) Same as (a)–(d) but for first-model-level wind direction (WS; degrees). (i)–(l) Same as (a)–(d) but for 0–1-km SRH (m^2 s^{-2}).

While surface roughness effects appear to dominate wind-related differences, thermal properties of the urban surface clearly are the main driver for thermodynamic differences from CTRLE (Fig. 5.3). As parameterized by the LSM (Table 2.3), increased stomatal resistance, along with lower surface emissivity and albedo in the urban area result in warmer, drier near-surface air over and downwind of the urban area in WestT (Fig. 5.3b,f), and these differences are dominant in WestF as well (Fig. 5.3d,h). As warming and drying air near the surface tends to raise the LCL, CAPE also decreases by $\sim 200 - 300$ J kg^{-1}

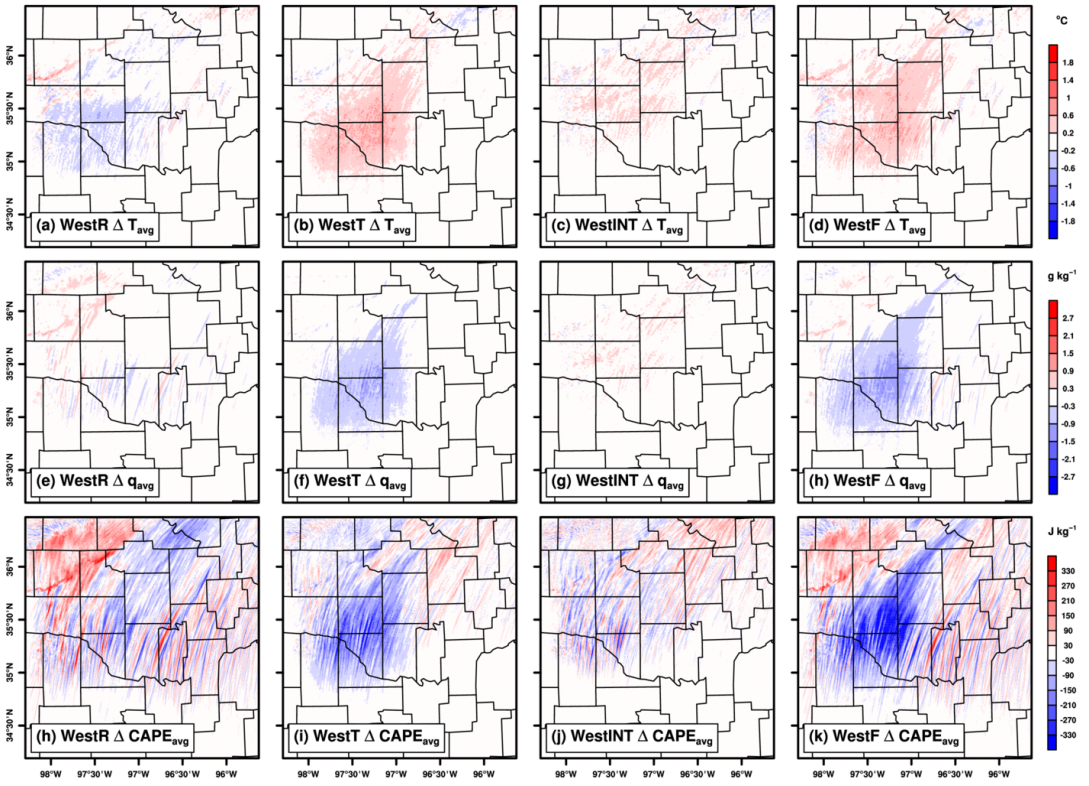

Figure 5.3: Same as Fig. 5.2, but for (a)–(d) first-model-level temperature (T_{avg}; °C), (e)–(f) first-model-level water vapor mixing ratio (q_{avg}; g kg^{-1}), and (h)–(k) CAPE (J kg^{-1}).

($\sim 5-10\%$) over and downstream of the urban area in WestT and WestF (Fig. 5.3,j,l). The interactions term does not contribute to the differences in WestF in a coherent manner for any of these thermal properties (Fig. 5.3c,g,j).

Stronger winds (Fig. 5.2a) and lower 0–1-km SRH (Fig. 5.2i) in the vicinity of the surface stationary front in WestR suggest that the presence of the city as a roughness element resulted in the stationary front being slightly further north. Opposite changes for WestT (Fig. 5.2b,j) indicates that the front was slightly further south in these simulations. These observations about the location of the front are supported by slightly warmer temperatures in the general frontal location in WestR (Fig. 5.3b).

Wind speed modifications on the order simulated here have been observed in previous studies (e.g., Hu et al. 2016, RS17b). Additionally, the simulation of a warm, dry urban area is consistent with theory for and observations of the results from replacing natural vegetation with man-made surfaces (e.g., Barlow 2014). Given that our results generally agree with theory and observations, we are confident that the simulated urban-atmosphere interactions presented here are reasonable.

5.2.2 Factor separation results

Factor separation variables are computed for each of the 8 urban locations according to the procedure described in Section 2.8. Surface roughness in WestR results in a significant southerly shift in storm-total rainfall (Fig. 5.4b). Approximately 25–45 mm more rain falls south of the main CTRLE maximum in precipitation (Fig. 5.4a), but similarly less rain falls in the vicinity of the CTRLE maximum. Although thermal properties (WestT) of the western urban areas don't result in any significant rainfall differences (Fig. 5.4c), large-magnitude interactions between thermal and roughness properties (Fig. 5.4) are frequently of opposite sign of the changes caused by surface roughness. These effects combine in the full-physics urban parameterization (WestF; Fig. 5.4e), resulting in few significant rainfall deviations from CTRLE. For East simulations, only spotty differences exist (Fig. 5.4f–i), suggesting that urban interactions late in the storm life cycle don't significantly modify rainfall patterns.

WestR simulations have a large area of significantly stronger updraft velocities (W_{max}; Fig. 5.5b) south of the swath of increased rainfall (Fig. 5.4b). Much of this region, particularly that with significant increases, falls south of the highest CTRLE updraft velocities (Fig. 5.5a). Unlike with the region of greater rainfall, the region of stronger vertical motions in WestR is not accom-

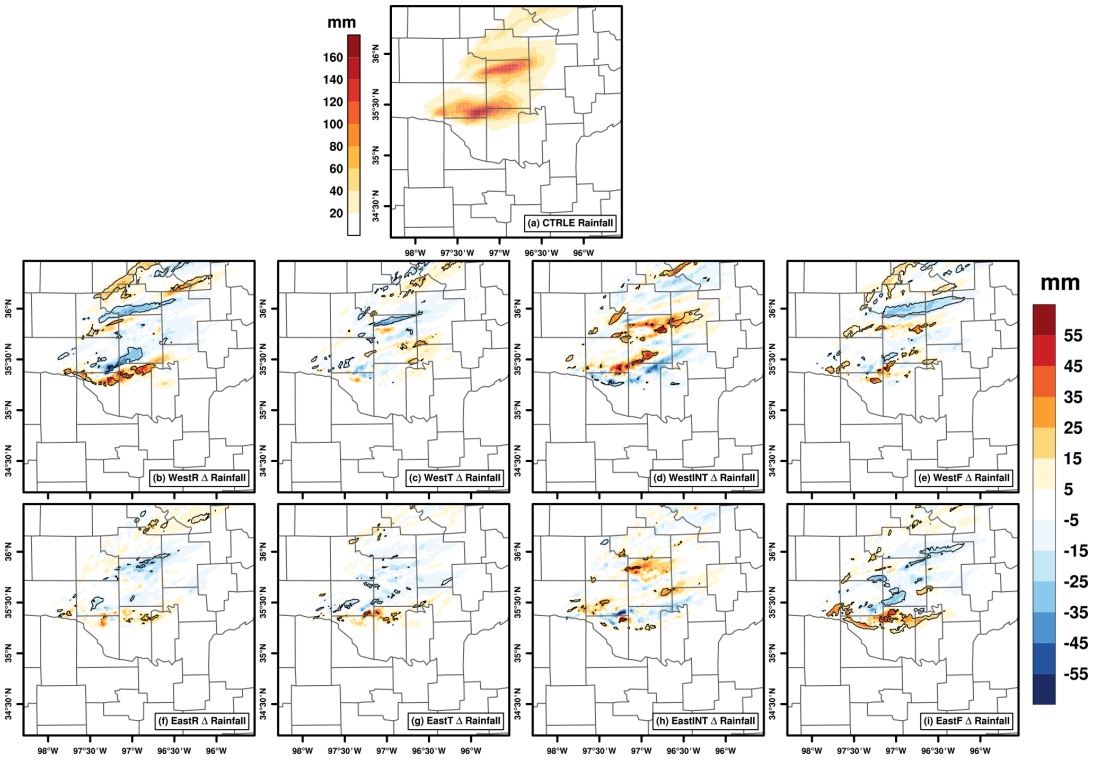

Figure 5.4: l(a) Color-filled contours of CTRLE-averaged storm-total rainfall (mm) (b)–(e) Color-filled contours of differences from CTRLE in storm-total accumulated rainfall (mm) for simulations WestR, WestT, WestINT (i.e. the interactions contribution), and WestF, in that order. (f)–(l) Same as (b)–(e) but for EastR, EastT, EastINT, and EastF, in that order.

panied by an additional nearby area of equally slower updraft speeds. Hence, this does not appear to be a simple southward change in storm track. A small area of significantly stronger vertical velocities is present in EastR (Fig. 5.5f), but it is not as large, or displaced as far south from the CTRLE maximum, as in WestR. As with rainfall changes, few significant updraft strength differences results from the thermal aspects of the urban area (Fig. 5.5c,g), though there are a few locations of stronger vertical motion near the end of the storm track when the city is in the eastern portion of the domain (Fig. 5.5g). Although the contribution to vertical velocity changes by interactions between surface roughness and thermodynamic properties (Fig. 5.5d,h) are generally opposite in sign

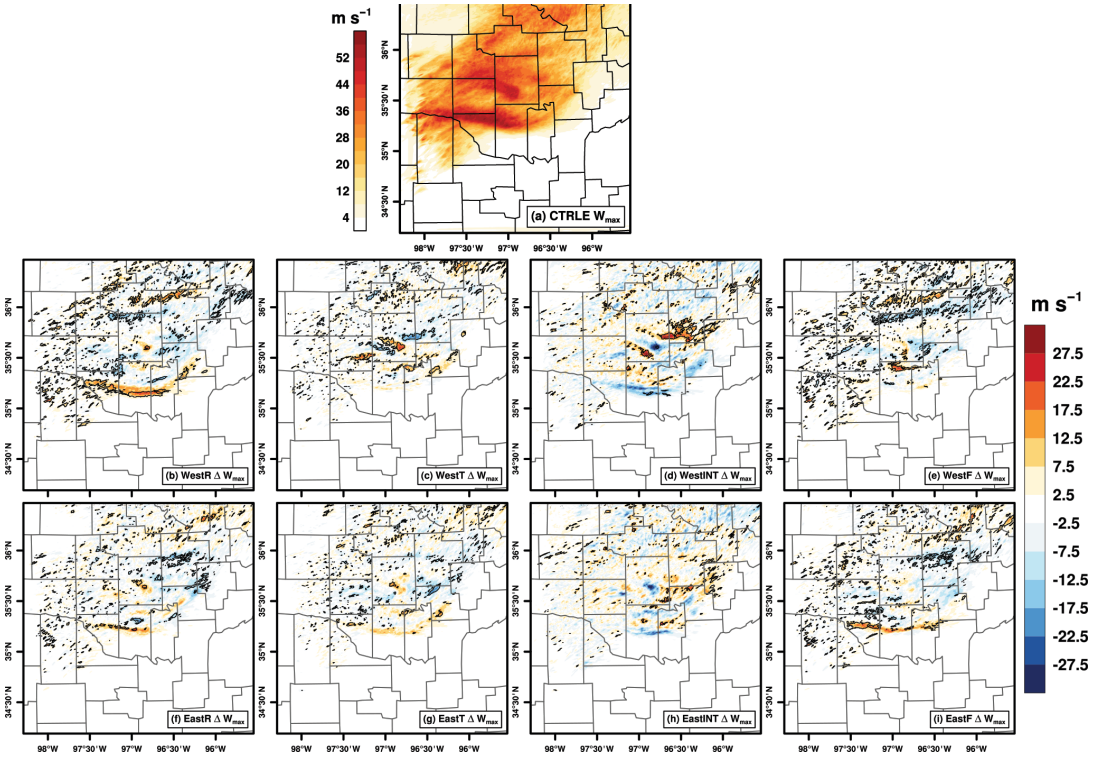

Figure 5.5: Same as Fig. 5.4 but for time-composite maximum updraft speed (w_{max}; m^2 s^{-1}).

to the two contributions individually, as they were for modifications in rainfall, they only mask these signals in West simulations (Fig. 5.5e), but not in East members (Fig. 5.5i). Thus, though the roughness contribution to changes in vertical motion is much larger, and over a broader area, in the WestR simulations than in EastR, interactions between the two processes obscure this change in WestF. All of the spatial patterns associated with vertical velocity are echoed in those of time composite 2–5-km UH (Fig. 5.6), reinforcing that faster (slower) updraft velocities are associated with a stronger (weaker) mid-level mesocyclone.

Slower maximum near-surface wind speeds (WS_{max}) due to surface roughness are the most obvious feature in the spatial distribution of maximum wind speed in WestR and EastR (Fig. 5.7b,f). Surface roughness does not appear to affect the winds associated with the storm's rear flank downdraft (RFD), which are

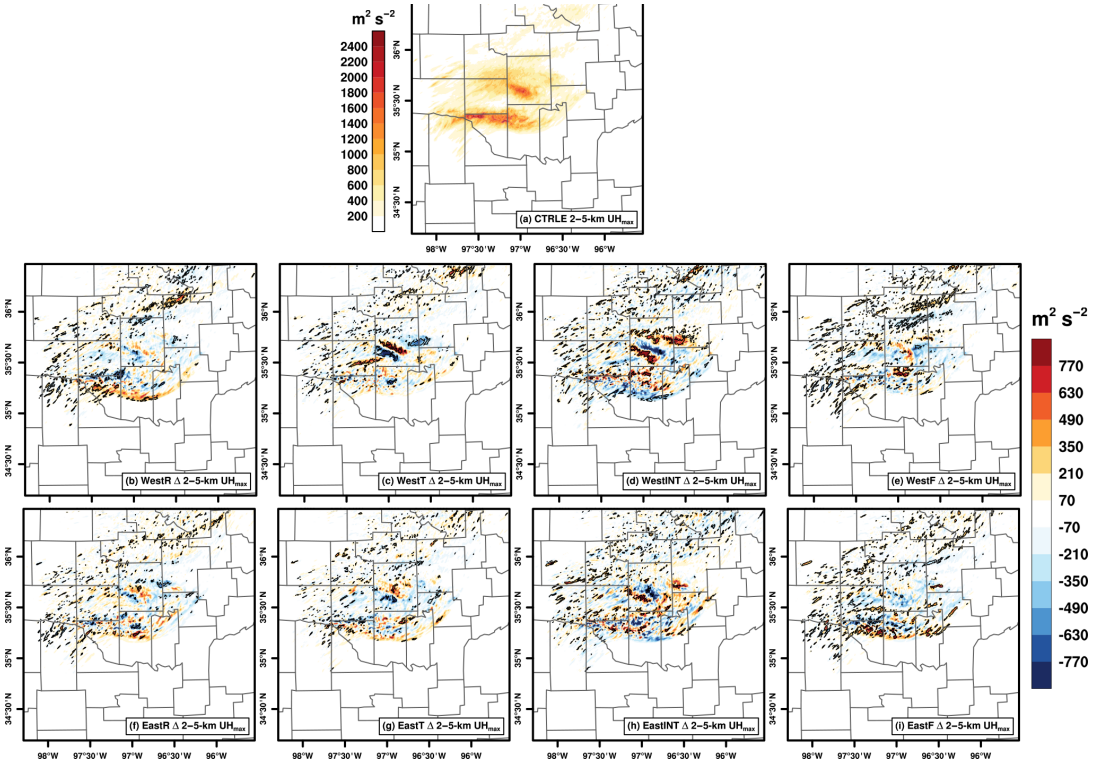

Figure 5.6: Same as Fig. 5.4 but for time-composite maximum 2–5-km UH (m^2 S^{-2}).

the strongest winds produced by the storm (Fig. 5.7a), though the forward flank downdraft (FFD) winds are significantly slower in WestR (Fig. 5.7b). Few large areas of enhanced wind speeds near the storm exist in any of the factor plots (Fig. 5.7b–d,f–h), though in EastF the three components combine to result in generally increased wind speeds in the RFD region in the first half ot the storm's lifecycle (Fig. 5.7i), particularly just before it reaches the western edge of the urban area. This is not the case in WestF (Fig. 5.7e) as the storm is interacting with the city over nearly its entire lifetime and the differences are dominated by those caused by roughness (WestR; Fig. 5.7b).

Near-surface minimum temperature (T_{min}) generally decreases due to surface roughness (Fig. 5.8b,f), particularly for WestR (Fig. 5.8b). Similar to the pattern of differences of W_{max} (Fig. 5.5) and 2–5-km UH_{max} (Fig. 5.6), this

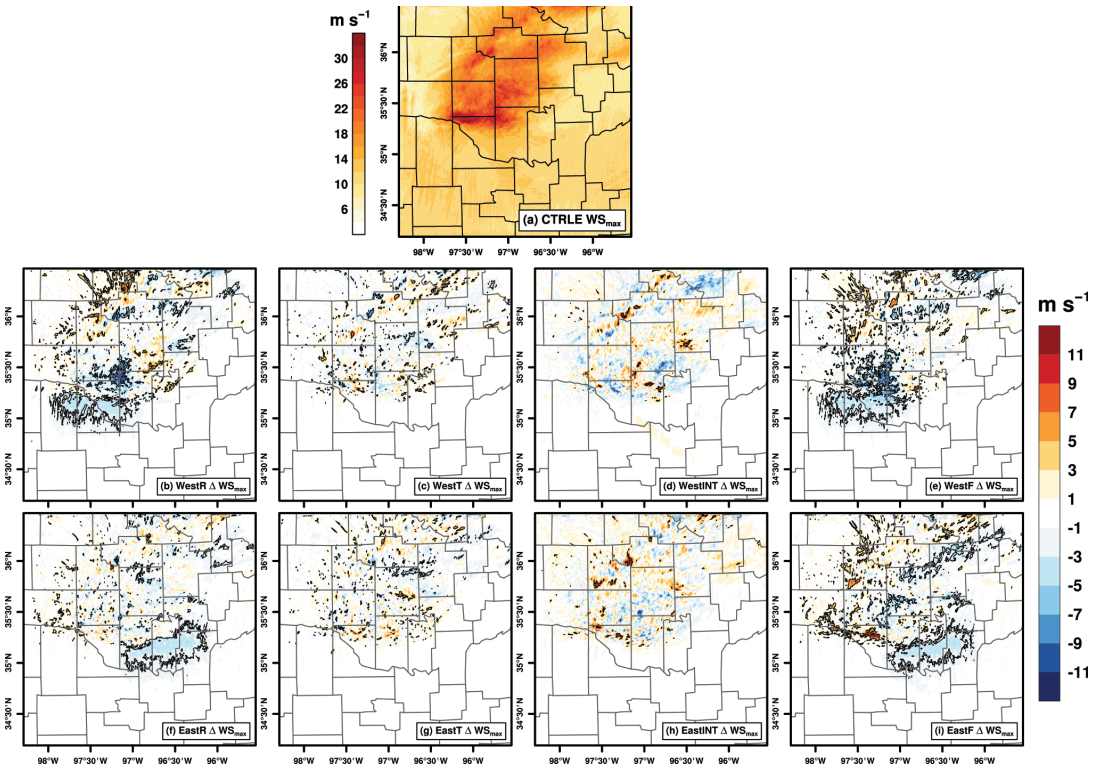

Figure 5.7: Same as Fig. 5.4 but for time-composite maximum first-model-level wind speed (WS_{max}; m s^{-1}).

area of colder temperatures is generally south of the coldest temperatures in the CTRLE run. Urban-induced warming near the surface is clear in both WestT (Fig. 5.8c) and EastT (Fig. 5.8g). Though this warm area is apparently negated by the storm passing over the urban area later in the storm's lifetime in EastT, air is much warmer near the surface near the beginning of the storm track in WestT. Although factor interactions result in large magnitude changes in T_{min} (Fig. 5.8d,h), none of these differences from CTRLE are significant. The resulting T_{min} field in the full-physics simulations (Fig. 5.8e,i) shows generally cooler temperatures near the latter part of the storm track, particularly in EastF (Fig. 5.8i), where all three factors are of the same relative sign (cooler than CTRLE) in this area.. However, the significant cooling south of the CTRLE

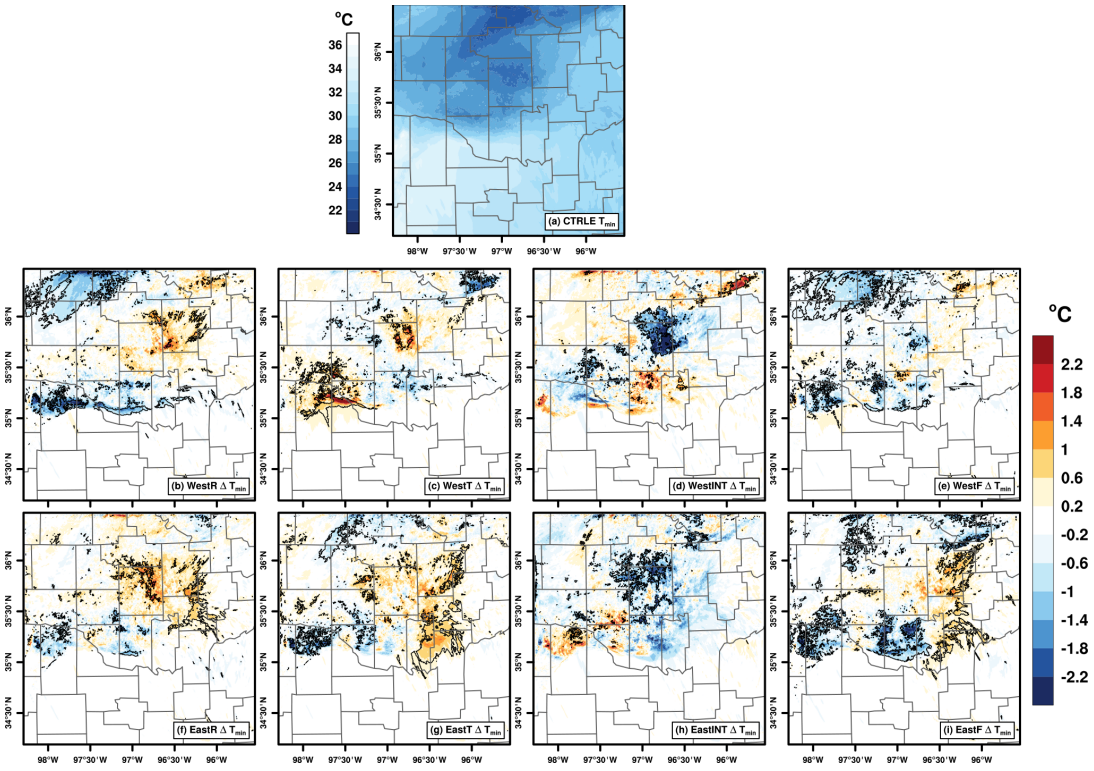

Figure 5.8: Same as Fig. 5.4 but for time-composite minimum first-model-level temperature (T_{min}; °C).

track present in WestR (Fig. 5.8b) is not clear in WestF due to the warmer T_{min} caused by the thermal and interaction terms.

To evaluate storm characteristics regardless of location, we can examine time series of accumulated variables related to mesocyclone strength and storm evolution. Although spatial analysis of 2–5-km $\mathrm{UH_{max}}$ (Fig. 5.6) and W_{max} (Fig. 5.5) suggested regions of increased mesocyclone strength, time series analyses of difference from CTRLE in group-averaged, mesocyclone-averaged 2–5-km UH indicate minimal deviations of all urban simulations from CTRLE (Fig. 5.9a,e), except near the very end of the storm's lifetime. However, large differences are present in a similar analysis of 0–1-km UH (Fig. 5.9b,f). While surface roughness and thermal properties of the urban area alone generally have little affect on 0–1-km UH in West, the interaction of the two results in a weaker

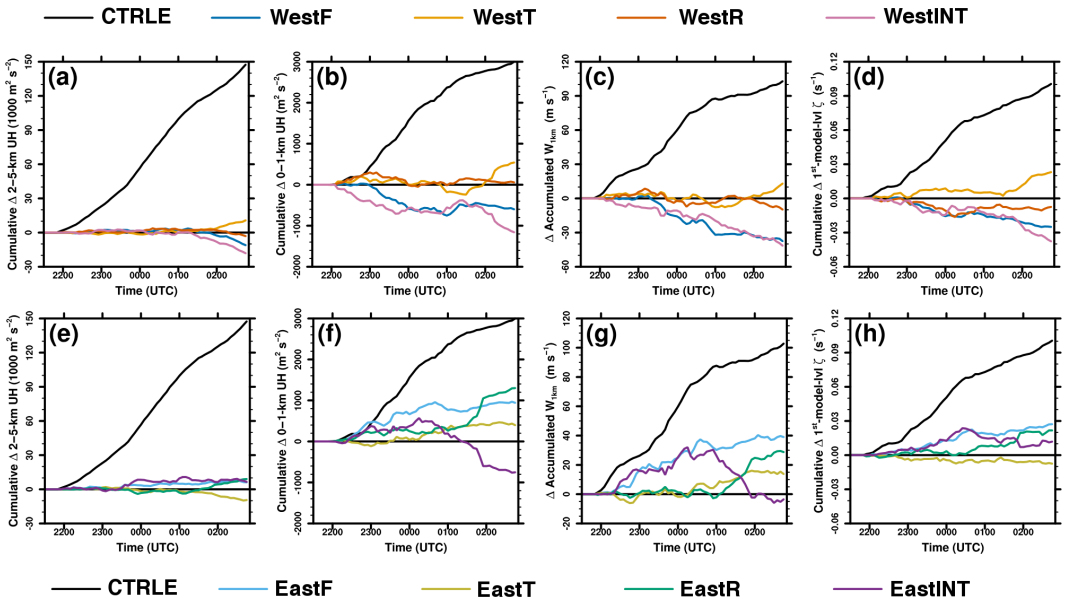

Figure 5.9: Cumulative CTRLE group average (black) and accumulated difference from CTRLE of WestR (red), WestT (yellow), WestINT (pink), and WestF(blue) simulations of mesocyclone-averaged (a) 2–5-km UH, (b) 0–1-km UH, (c) column-maximum updrat speed, and (d) first-model-level ζ as a function of time. (e)–(f) Same as (a)–(d) but for EastR (green), EastT (yellow-green), EastINTER (purple), and EastF (light blue).

low-level meoscyclone, particularly in the early stages of the storm's lifetime, and these interactions dominate the time series for the full-physics simulation. The result is WestF mesocyclones averaging $\sim$ 20% less 0–1-km UH by the end of the storm's life. The interactions term also dominates the increased 0–1-km UH in East early in its lifetime (Fig. 5.9f), however the thermal and roughness contributions generally are generally positive as well. As the storm approaches the center of eastern city locations, the thermal and roughness contributions increase, most notably the roughness contribution after $\sim$ 0200 UTC. Together, these factors result in EastF having $\sim$ 33% more 0–1-km UH than CTRLE. The contributions of the various factors to the total full-physics simulation of mesocyclone-averaged w at 1 km AGL ()w_{1km}; Fig. 5.9c,g) and first-model-level vertical vorticity (ζ_{max}; Fig. 5.9d,h) are generally vary similar to those of 0–1-

km UH. Particularly important in these results is that, in addition to the 40% increase in 0–1-km UH, W_{1km} and first-model-level vertical vorticity increased by approximately 40% and 30%, respectively, for the full-physics simulations with the urban area on the eastern side of the domain.

5.3 Discussion and Conclusions

This study used the WRF to evaluate the individual contributions of urban surface roughness and thermodynamic characteristics to the modifications of a supercell caused by the Dallas-Ft. Worth metropolitan area. A total of 34 unique simulations were used for this analysis. Of these, 10 were CTRL simulations (CTRLE) with no urban areas, and grassland throughout the smallest domain. Additionally, the land use of DFW was inserted in to this domain in 8 unique locations, and 3 simulations performed for each unique city location: full urban physics, urban roughness effects only, and urban thermodynamic effects only . Thus a total of 24 simulations with urban areas were used. Following the work of Stein and Alpert (1993), and using these simulations, we carried out a factor separation analysis to determine which properties of the urban area result in the greatest differences from the non-urban CTRLE simulations.

Urban effects on the pre-storm environment were generally as expected based on theory. When the urban area was parameterized only as an area with increased surface roughness, winds near the surface were $\sim 15-20\%$ lower in the urban simulations. Additionally, parameterizing the urban area only with thermal differences results in near-surface ~ 1 ^{o}C warming and ~ 0.5 g kg^{-1} lower water vapor mixing ratio over and downwind of the urban area. Beyond these obvious effects, surface roughness also contributed to some slight cooling near the surface, perhaps due to increased turbulent mixing and thus greater downward

turbulent transport of cooler air. Furthermore, thermodynamic effects lead to patchy, small magnitude increases in wind speed over the urban area, likely due to increased downward turbulent transport of higher momentum (Wang et al. 2007; Hu et al. 2013). However, these changes were quite small in comparison to those induced by urban surface roughness. This result suggests that surface roughness is the dominant factor in controlling near-surface wind speeds in the urban area in these simulations, a finding that agrees with observations of Hu et al. (2016) and those presented in Chapter 3.

The most significant contributor to differences from CTRLE in the spatial distribution of storm characteristics was surface roughness in simulations with DFW in the western locations. In these WestR simulations, rainfall and maximum updraft speed increased and minimum near-surface temperatures decreased to the south of the southernmost CTRL storm track, but cumulative mesocyclone-averaged vertical wind speed is relatively unchanged. These findings indicate that the mid-level mesocyclone of the southern storm, and the attendant RFD, moved further south in the WestR simulations, though mesocyclone strength remained relatively unchanged. This southward deviation is not apparent in the full-physics urban simulations typically because the contributions of the interaction term (or those of thermodynamics in the case of minimum near-surface temperatures) are frequently of the same magnitude, but of opposite sign, in corresponding location. The result is that few spatial characteristics of storm strength and evolution are significantly different from CTRLE in simulations where the storm interacts with the urban area earlier in its lifetime. Contrary to this result for WestF, few individual factor contributions to spatial differences in simulations with eastern-located urban areas (East) are large or significant individually. However, the contributions of thermal, roughness, and interactions between the two are generally the same sign in similar

locations, resulting in full-physics simulations with spatial fields that vary significantly from CTRLE. The summation of these three factors provides EastF simulations that, similar to WestR, depict southward movement of the southernmost mesocyclone. Additionally, low-level mesocylone and near-surface circulation are generally higher ($\sim 30-40\%$ accumulated) in the EastF simulation compared to CTRLE, with the interactions term contributing the most to this difference, though roughness and thermodynamic properties generally bolster these changes.

One of the most important finding from these results is that increased shear as induced by the urban area can have a noticeable effect on supercell evolution and dynamics. While low-level shear has certainly been a focus for investigations of supercellular dynamics over the past decade (e.g., Esterheld and Giuliano 2008; Togstad et al. 2011; Nowotarski and Jensen 2013; Markowski et al. 2012; Markowski and Richardson 2014), is it typically only a secondary focal point for urban studies as most research focuses on UHI effects. Additionally, modeling studies involving the urban area frequently neglect to analyze the accuracy of wind speed predictions, often because their study periods feature synoptically-weak regimes (i.e., ideal conditions for heat waves). Given that the results presented in this study suggest that supercell modifications by frictionally slowed wind speeds in the urban area can be important, future urban research should focus both on properly reproducing urban winds in numerical simulations, as well as the mechanisms by which these changes can effect supercellular evolution.

Regardless of city location, the contribution of interactions between thermodynamic and roughness characteristics of the urban area to differences between urban and non-urban simulations is frequently of similar magnitude (if not larger) than the individual contributions of either effect. However, the contribution of these interactions to pre-storm differences in the urban area was

not large, making interpretations of this result difficult and inconclusive. To elucidate the processes by which these complicated interactions modify storm dynamics, future work could involve performing factor separation simulations for all 108 simulations and running the hierarchical clustering algorithm on the thermodynamic and roughness runs separately. If these simulations group differently than the full-physics runs, this could make clearer the mechanisms of storm modification by the various factors.

Chapter 6

Summary

The analyses presented here used the ARW-WRF to determine the most appropriate urban parameterization for a Great Plains supercell simulation, and then analyze the effects of an urban area, parameterized using the chosen scheme, on the strength and evolution of a supercell. These analyses were based on the novel approach of using hierarchical clustering (HCA) on supercell simulations with cities placed in various locations to create natural groupings of similar simulations. The HCA clusters guided the intercomparison of groups of urban simulations with cities in proximal locations. A unique application of the factor separation procedure was also used to determine which aspects of the urban environment had the greatest effect on supercell strength and evolution. The most important conclusions from these investigations were:

- **The modified Noah land surface model provides the most accurate representation of urban-atmosphere interactions for a city typical of the Great Plains.** The oft-used SLUCM reproduces a more appropriate nocturnal UHI, when the UHI is strongest. However, by late-afternoon (the time period of most interest for a severe weather simulation), both the SLUCM and the Noah LSM produce similar UHIs. The most significant difference between the two is that the Noah LSM significantly outperforms the SLUCM in simulating appropriately-slow urban wind speeds. SLUCM winds were **faster** in urban areas than over rural

land. As near-surface winds can play an important role in supercell dynamics, it is important that the chosen urban parameterization properly reproduce of slower wind speeds in the urban area. Hence, a modified version of the Noah LSM bulk urban scheme was chosen for use in the subsequent simulations.

- **Low-level storm properties are more dependent on city location than measures of mid-level storm strength.** Hierarchical clustering analysis of full-physics urban simulations indicated that simulations with proximal city locations produce storms with similar low-level evolution, such as 0–1-km updraft helicity and near-surface temperature. Similar geographical clusters were not produced for variables such as storm-total rainfall and 2–5-km updraft helicity. This does not mean that the city had *no effect* on the storm's mid-level structure, but that city location was not the primary cause of urban-induced differences in the full-physics runs.

- **In full-physics urban simulations, storm interactions when the urban area was generally south of the storm track, and the interaction occurred early in the storm's lifetime, resulted in minimal differences in low-level storm strength.** Low-level mesocyclone strength in simulations with the urban area south of the track and in the western half of the domain (resulting in early-lifetime, longterm interactions) differed little from that of the non-urban simulations for most of its lifetime, and the near-surface vertical vorticity in these simulations was upwards of 10% less than in non-urban simulations midway through the simulation.

- **When the full-physics city was in non-southwesterly locations within the domain, low-level mesocyclone strength and near-**

surface vertical vorticity were consistently higher than in non-urban simulations. In particular, simulations where the city was either north of the storm or when the storm passed north of the city late in its lifetime accumulated $\sim 20 - 30\%$ more 0–1-km updraft helicity and $\sim 10\%$ more near-surface rotation. Though mid-level mesocyclone strength changed very little for any of these simulations, the mesocyclone (and its attendant RFD) took a more significantly more southerly track during the second half of the storm life cycle for those simulations in which the city was in the eastern half of the domain.

- **Urban surface roughness and the interactions between urban thermal and surface roughness properties properties are significant contributors to urban storm modification.** Most investigations of near-surface urban properties and urban-storm interactions focus on the impact of the UHI, but the results presented here argue for a greater focus on the implications of urban surface roughness. Unlike in the full-physics simulations, those simulations with the city parameterized only as a roughness element, and with a long urban-storm interaction, resulted in the largest differences from non-urban simulations of any of the factor separation analyses. The mid-level mesocyclone traveled further south in the second half of the storm's lifetime, as did the attendant low-level mesocyclone and rear-flank downdraft, although low-level storm strength generally decreased. Even for those simulations where the storm interacted with the urban area later, and for a less protracted time, surface roughness provided large contributions, most notably for mesocyclone strength.

While HCA has been used previously for attribution of variations in synoptic and mesoscale fields to various factors, this is the first time it has been used to

analyze storm-scale modifications. Given their large scale of motion, synoptic and mesoscale phenomena are generally more predictable than severe storms, thus few simulations are required to prove attribution of large-scale field variations to modifications in boundary conditions and parameterization options. However, to perform attribution of small-scale effects to various factors in a real data simulation, a large number of simulations are required to ensure that the simulated changes are significant. The general hindrance to such an analysis is the significant computational requirement. However, as computational power continues to improve, such barriers are removed. Given the successful use of HCA in the present work, future investigations of cause-and-effect relationships in small-scale phenomena are encouraged to use such a technique. For example, some recent research (e.g., Bosart et al. 2006; Markowski and Dotzek 2011) has investigated the effect of complex terrain on tornadogenesis and tornado maintenance, with the results suggesting that terrain effects are quite complex. Such a problem could be further investigated by performing HCA on a large number of fine-grid simulations. These kinds of investigations are also pertinent to the Warn-on-Forecast (Stensrud et al. 2009) effort as correctly predicting fine-scale interactions could prove critical to forecasting a storm's severe potential.

In comparison to studies on the effects of the urban area on weakly-forced convection (i.e., Bornstein and Lin 2000; Shepherd et al. 2002, 2010a; Niyogi et al. 2011), precipitation patterns in the simulations presented in this dissertation were not well-correlated with urban location, as suggested by the highly varied HCA group city locations. This finding does agree, though, with those of studies that consider convective systems in synoptically active regimes that negligible large scale differences are found to be associated with the presence of urban areas (Yang et al. 2014a; Yeung et al. 2015; Ryu et al. 2016). Combined with these previous findings, the results presented here suggest that organized convective

processes are less susceptible, on a large scale, to the effects of urban areas, but that storm-scale deviations (e.g., mesocyclone strength and track) can be modified by a large urban area.

Chapter 3 provided evidence that the simulation configuration used here produced realistic near-surface urban effects that compared well to observations. It is also important that these simulations produce realistic properties over the entire boundary layer. However, the analyses of boundary layer properties presented here were not compared to observations as no such observational data exist. Field studies that collect data over the entire PBL across an urban area could provide a comparison point, hence campaigns of this sort would prove useful. These observations could also be supported by large eddy simulations (LESs) to improve understanding of the evolution of boundary layer properties over an urban area.

Comparing the results presented here to LES simulations and observations should help determine how much effect the horizontal grid scale (500 m) used in these simulations may have on the results presented here. Wyngaard (2004) first noted that when model horizontal scale, Δx, approaches the scale of turbulent eddies, ℓ (i.e., $\ell/\Delta x \sim 1$), the horizontal grid size is too small to meet the assumptions implicit in Reynolds-averaged Navier-Stokes modeling (i.e., the assumption that turbulent quantities are horizontally homogeneous across the grid cell), but too large to explicitly resolve individual eddies (as in LES simulations). He termed this horizontal scale the "terra incognita". At these scales, PBL parameterizations produced ensemble-mean fluxes by subgrid-scale motions that theoretically should include scales on the same order as grid-scale circulations. The outcome is the production of modeled fields in the convective boundary layer whose horizontal scale, growth rate, and peak intensity are dependent on both horizontal grid size and PBL scheme choice. The horizontal grid cell, 500

m, used in the simulations presented here falls squarely within the "terra ingonita", hence there may be grid-cell dependent circulations present in some of the simulations. However, the non-local YSU scheme was used here, in part because it has been shown to perform well in severe weather environments (Coniglio et al. 2013; Clark et al. 2015), but also because it generally suppresses spurious turbulent circulations at "terra incognita" scales (Ching et al. 2014). Hence, though extraneous, grid-cell dependent circulations may be produced by the simulations presented here, use of the YSU PBL scheme should minimize their effect. If simulated PBL properties presented here agree with those of LES simulations and observations, this would further increase confidence in the realism of the urban-storm interactions simulated here.

The ultimate goal of this line of research is to provide guidance for city planning. Currently, the only way to reduce loss of life from severe storms is to encourage proper sheltering procedures, while property losses are unavoidable. However, if research can suggest that storm modification is possible with urban planning procedures, strategies to minimize loss of life and property could become more varied and perhaps effective as it would remove the unpredictable element of personal sheltering choices. While the research presented in this dissertation is only a very preliminary step along this path, hopefully it will encourage more research in this area.

Towards this goal, the next step should be performing factor separation analyses on more simulations, and then using hierarchical clustering analysis on the individual factor results as opposed to only on the full-physics simulations. The results presented in Chapter 5 suggested that the individual contributions of urban surface roughness and thermal qualities may not resemble the full-physics simulations on which HCA was used. In simulations where urban-storm interactions occurred very early in the storm's lifetime, surface roughness resulted

in considerable southerly deviations in storm track, though this modification to storm track was not evident in the full-physics simulations as the changes caused by roughness were often countered by thermal or interaction contributions. In contrast, while few significant differences were evident in the individual contributions of the various factors when urban-storm interactions occurred later, the contributions were typically of the same sign in corresponding locations, and hence combined to result in significant full-physics deviations from non-urban simulations. These contrasting results suggest that the contributions of surface roughness and thermodynamic properties do not vary together as the location of the city changes, and thus HCA of the factor results separately should allow for proper attribution of supercell modifications to various aspects of the urban environment.

Future simulations should also be configured for parcel trajectory analysis (i.e., very short history output intervals). While HCA may provide information on which simulations are most similar to each other, and suggest which aspects of the urban area are most important for storm modification, they provide minimal evidence for *how* these changes in surface properties modify storm characteristics. Computing vorticity and buoyancy budgets along parcel trajectories that enter a storm's mesocyclone could elucidate how the urban surface modulates low- and mid-level mesocyclone strength and evolution.

The analyses in Chapters 4 and 5 used only one set of urban parameters (e.g., surface roughness) to simulate one urban area interacting with one storm in particular. To broaden the scope of this research and arrive at a more general conclusion about urban modification of severe storms, future simulations should include a wide array of variations on the simulation design presented here. Simulating different storm modes (e.g., mesoscale or linear convective systems) could illuminate urban effects on severe convection with different storm dynamics, as

could simulating a different supercell. Additionally, using various urban areas of different sizes, roughness values and distributions, shapes, and thermal properties in simulations could provide suggestions for the best hazard-mitigating urban planning strategies. It would also be important to investigate how urban-storm interactions change under varied UHII conditions, such as the weaker (or sometimes negative) UHII conditions when rural soil moisture dries out during drought or early fall conditions. This could be simulated by artificially decreasing rural soil moisture values.

To verify findings from the present work and future investigations concerning urban modification of convection, observations of severe storms in the vicinity of urban areas would prove useful. Candidate cases could be simulated, both with and without the urban area, and compared to observations. In contrast to the current research and the avenues presented above, these simulations would attempt to reproduce reality. However any of the methods suggested above (e.g. modifying urban properties, trajectory analyses, etc.) could be used to investigate these simulations more thoroughly. If investigations of this kind can supply evidence of urban modification in real storm data, this would provide the most compelling argument for using urban planning to mitigate life and property losses from severe storms.

References

Aase, J. K. and F. H. Siddoway, 1982: Evaporative flux from wheat and fallow in a semiarid climate. *Soil Sci. Soc. Am. J.*, **46** (3), 619 pp. doi:10.2136/sssaj1982.03615995004600030034x.

Adachi, S. A., F. Kimura, H. Kusaka, M. G. Duda, Y. Yamagata, H. Seya, K. Nakamichi, and T. Aoyagi, 2014: Moderation of summertime heat island phenomena via modification of the Urban form in the Tokyo metropolitan area. *J. Appl. Meteor. Climatol.*, **53**, 1886–1900. doi:10.1175/JAMC-D-13-0194.1.

Alfieri, J. G., D. Niyogi, H. Zhang, M. A. LeMone, and F. Chen, 2009: Quantifying the spatial variability of surface fuxes using data from the 2002 International H2O Project. *Bound. Layer Meteorol.*, **133**, 323–341. doi:10.1007/s10546-009-9406-2.

Alhamed, A., S. Lakshmivarahan, and D. J. Stensrud, 2002: Cluster analysis of multimodel ensemble data from SAMEX. *Mon. Wea. Rev.*, **130**, 226–256. doi:10.1175/1520-0493(2002)130<0226:CAOMED>2.0.CO;2.

Alonso, M., M. Fidalgo, and J. Labajo, 2007: The urban heat island in Salamanca (Spain) and its relationship to meteorological parameters. *Clim. Res.*, **34** (1), 39–46,. doi:10.3354/ cr034039.

Anderberg, M. R., 1973: *Cluster Analysis for Applications.* Academic Press, 359 pp.

Arnfield, A. J., 2003: Two decades of urban climate research: A review of turbulence, exchanges of energy and water, and the urban heat island. *Int. J. Climatol.*, **23** (1), 1–26. doi:10.1002/joc.859.

Baik, J.-J., Y.-H. Kim, J.-J. Kim, and J.-Y. Han, 2007: Effects of boundary-layer stability on urban heat island-induced circulation. *Theor. Appl. Climatol.*, **89**, 73–81. doi:10.1007/s00704-006-0254-4.

Barlow, J. F., 2014: Progress in observing and modelling the urban boundary layer. *Urban Clim.*, **10**, 216–240. doi:10.1016/j.uclim.2014.03.011.

Basara, J. B., P. K. Hall, A. J. Schroeder, B. G. Illston, and K. L. Nemunaitis, 2008: Diurnal cycle of the Oklahoma City urban heat island. *J. Geophys. Res.*, **113** (D20). doi:10.1029/2008JD010311.

——, H. G. Basara, B. G. Illston, and K. C. Crawford, 2010: The impact of the urban heat island during an intense heat wave in Oklahoma City. *Adv. Meteor.*, **2010**, 10 pp. doi:10.1155/2010/ 230365.

——, and Coauthors, 2011: The Oklahoma City Micronet. *Meteorol. Appl.*, **18** (3), 252–261. doi:10.1002/met.189.

Benjamin, S. G., and Coauthors, 2004: An hourly assimilation-forecast cycle: The RUC. *Mon. Wea. Rev.*, **132**, 495–518. doi:10.1175/1520-0493(2004)132<0495:AHACTR>2.0.CO;2.

Bornstein, R. D. and D. S. Johnson, 1977: Urban-rural wind velocity differences. *Atmos. Environ.*, **11** (7), 597–604. doi:10.1016/0004-6981(77)90112-3.

Bornstein, R. and Q. Lin, 2000: Urban heat islands and summertime convective thunderstorms in Atlanta: three case studies. *Atmos. Environ.*, **34** (3), 507–516. doi:10.1016/S1352-2310(99)00374-X.

Bosart, L. F., A. Seimon, K. D. LaPenta, and M. J. Dickinson, 2006: Supercell tornadogenesis over complex terrain: The Great Barrington, Massachusetts, tornado on 29 May 1995. *Wea. Forecasting*, **21**, 897–922. doi:10.1175/WAF957.1.

Branković, Č., B. Matjačić, S. Ivatek-Šahdan, and R. Buizza, 2008: Downscaling of ECMWF ensemble forecasts for cases of severe weather: Ensemble statistics and cluster analysis. *Mon. Wea. Rev.*, **136**, 3323–3342. doi:10.1175/2008MWR2322.1.

Brock, F. V., K. C. Crawford, R. L. Elliott, G. W. Cuperus, S. J. Stadler, H. L. Johnson, and M. D. Eilts, 1995: The Oklahoma Mesonet: A technical overview. *J. Atmos. Oceanic Technol.*, **12**, 5–19. doi:10.1175/1520-0426(1995)012<0005.

Burian, S. J., W. S. Han, and M. J. Brown, 2005: Morphological analyses using 3D building databases: Oklahoma City, Oklahoma. Los Alamos National Laboratory Rep. LA-UR-05-1821, 63 pp.

Changnon, S. A., 1979: Rainfall changes in summer caused by St. Louis. *Science (80-.).*, **205** (4404), 402–404.

——, 2003: Urban modification of freezing-rain events. *J. Appl. Meteor.*, **42** (6), 863–870. doi:10.1175/1520-0450(2003)042<0863.

——, R. T. Shealy, and R. W. Scott, 1991: Precipitation changes in fall, winter, and spring caused by St. Louis. *J. Appl. Meteor. Climatol.*, **30**, 126–134. doi:10.1175/1520-0450(1991)030<0126.

Chappell, C. F., 1986: Quasi-Stationary Convective Events. *Mesoscale Meteorol. Forecast.*, American Meteorological Society, 289–310.

Chen, F. and J. Dudhia, 2001: Coupling an advanced land surface-hydrology model with the Penn State-NCAR MM5 modeling system. Part I: Model implementation and sensitivity. *Mon. Wea. Rev.*, **129**, 569–585. doi:10.1175/1520-0493(2001)129<0569.

Chen, F., and Coauthors, 2007: Description and evaluation of the characteristics of the NCAR high-resolution land data assimilation system. *J. Appl. Meteor. Climatol.*, **46**, 694–713. doi:10.1175/JAM2463.1.

——, S. Miao, M. Tewari, J.-W. Bao, and H. Kusaka, 2011: A numerical study of interactions between surface forcing and sea breeze circulations and their effects on stagnation in the greater Houston area. *J. Geophys. Res.*, **116.** doi:10.1029/2010JD015533.

Chen, F., X. Yang, and W. Zhu, 2014: WRF simulations of urban heat island under hot-weather synoptic conditions: The case study of Hangzhou City, China. *Atmos. Res.*, **138**, 364–377. doi:10.1016/j.atmosres.2013.12.005.

Chen, L., M. Zhang, and Y. Wang, 2015: Model analysis of urbanization impacts on boundary layer meteorology under hot weather conditions: A case study of Nanjing, China. *Theor. Appl. Climatol.*, 1–16. doi:10.1007/s00704-015-1535-6.

Ching, J., R. Rotunno, and M. LeMone, 2014: Convectively induced secondary circulations in fine-grid mesoscale numerical weather prediction models. *Mon. Wea. Rev.*

Chou, M. D. and M. J. Suarez, 1999: A solar radiation parameterization for atmospheric studies. NASA Tech. Rep. Series on Global Modeling and Data Assimilation, NASA/TM-1999- 104606, Vol. 15, 38 pp. [Available online at http://gmao.gsfc.nasa.gov/pubs/docs/Chou136.pdf.]

——, ——, X. Z. Liang, and M. M. H. Yan, 2001: A thermal infrared radiation parameterization for atmospheric studies. NASA Tech. Rep. Series on Global Modeling and Data Assimilation, NASA/TM-2001-104606, Vol. 19, 68 pp. [Available online at http://ntrs.nasa.gov/archive/nasa/casi.ntrs.nasa.gov/20010072848.pdf.]

Clark, A. J., and Coauthors, 2012a: An overview of the 2010 Hazardous Weather Testbed experimental forecast program spring experiment. *Bull. Amer. Meteor. Soc.*, **93**, 55–74. doi:10.1175/BAMS-D-11-00040.1.

——, J. S. Kain, P. T. Marsh, J. Correia, M. Xue, and F. Kong, 2012b: Forecasting tornado pathlengths using a three-dimensional object identification algorithm applied to convection-allowing forecasts. *Wea. Forecasting*, **27**, 1090–1113. doi:10.1175/WAF-D-11-00147.1.

——, M. C. Coniglio, B. E. Coffer, G. Thompson, M. Xue, and F. Kong, 2015: Sensitivity of 24-h forecast dryline position and structure to boundary layer parameterizations in convection-alowing WRF model simulations. *Wea. Forecasting*, **30**, 613–638. doi:10.1175/WAF-D-14-00078.1.

Coniglio, M. C., J. Correia, P. T. Marsh, and F. Kong, 2013: Verification of convection-allowing WRF model forecasts of the planetary boundary layer using sounding observations. *Wea. Forecasting*, **28**, 842–862. doi:10.1175/WAF-D-12-00103.1.

Coquillat, S., M.-i. Boussaton, M. Buguet, D. Lambert, J.-F. Ribaud, and A. Berthelot, 2013: Lightning ground flash patterns over Paris area between 1992 and 2003: Influence of pollution? *Atmos. Res.*, **122**, 77–92. doi:10.1016/j.atmosres.2012.10.032.

Craven, J. P., H. E. Brooks, and J. A. Hart, 2004: Baseline climatology of sounding derived parameters associated with deep, moist convection. *Natl. Wea. Dig*, **28**, 13–24.

Cui, Y. Y. and B. Foy de, 2012: Seasonal variations of the urban heat island at the surface and the near-surface and reductions due to urban vegetation in Mexico City. *J. Appl. Meteor. Climatol.*, **51**, 855–868. doi:10.1175/JAMC-D-11-0104.1.

Dou, J., Y. Wang, R. Bornstein, and S. Miao, 2015: Observed spatial characteristics of Beijing urban climate impacts on summer thunderstorms. *J. Appl. Meteor. Climatol.*, **54**, 94–105. doi:10.1175/JAMC-D-13-0355.1.

Dyer, A. J. and B. B. Hicks, 1970: Flux-gradient relationships in the constant flux layer. *Q. J. R. Meteorol. Soc.*, **96** (410), 715–721. doi:10.1002/qj.49709641012.

Ek, M. B., 2003: Implementation of Noah land surface model advances in the National Centers for Environmental Prediction operational mesoscale Eta model. *J. Geophys. Res.*, **108** (D22), 8851 pp. doi:10.1029/2002JD003296.

Esterheld, J. M. and D. J. Giuliano, 2008: Discriminating between Tornadic and Non-Tornadic Supercells: A New Hodograph Technique. *E-Journal Sev. Storms Meteorol.*, **3** (2), 1–50.

Fairall, C. W., E. F. Bradley, D. P. Rogers, J. B. Edson, and G. S. Young, 1996: Bulk parameterization of air-sea fluxes for Tropical Ocean-Global Atmosphere Coupled-Ocean Atmosphere Response Experiment. *J. Geophys. Res. Ocean.*, **101** (C2), 3747–3764. doi:10.1029/95JC03205.

Fry, J., and Coauthors, 2011: Completion of the 2006 national land cover database for the conterminous united states. *Photogramm. Eng. Remote Sensing*, **77** (9), 858–864.

Ganeshan, M., R. Murtugudde, and M. L. Imhoff, 2013: A multi-city analysis of the UHI-influence on warm season rainfall. *Urban Clim.*, **6**, 1–23. doi:10.1016/j.uclim.2013.09.004.

Gedzelman, S. D., S. Austin, R. Cermak, N. Stefano, S. Partridge, S. Quesenberry, and D. A. Robinson, 2003: Mesoscale aspects of the urban heat island around New York City. *Theor. Appl. Climatol.*, **75**, 29–42. doi:10.1007/s00704-002-0724-2.

Grachev, A. A., C. W. Fairall, and E. F. Bradley, 2000: Convective profile constants revisited. *Bound. Layer Meteor.*, **94** (3), 495–515. doi:10.1023/A:1002452529672.

Grant, L. D. and S. C. Heever van den, 2014: Aerosolcloudland surface interactions within tropical sea breeze convection. *J. Geophys. Res. Atmos.*, **119** (13), 8340–8361. doi:10.1002/2014JD021912.

Grimmond, C. S. B. and T. R. Oke, 1986: Urban water balance. II: Results from a suburb of Vancouver, B.C. *Water Resour. Res.*, **22** (10), 1404–1412. doi:10.14288/1.0041948.

Grossman-Clarke, S., J. A. Zehnder, T. Loridan, C. Sue, and B. Grimmond, 2010: Contribution of land use changes to near-surface air temperatures during recent summer extreme heat events in the Phoenix metropolitan area. *J. Appl. Meteor. Climatol.*, **49**, 1649–1664. doi:10.1175/2010JAMC2362.1.

Gutiérrez, E., A. Martilli, J. L. Santiago, and J. E. González, 2015a: A mechanical drag coefficient formulation and urban canopy parameter assimilation technique for complex urban environments. *Bound. Layer Meteor.*, **157** (2), 333–341. doi:10.1007/s10546-015-0051-7.

Gutiérrez, E., J. E. González, A. Martilli, R. Bornstein, and M. Arend, 2015b: Simulations of a heat-wave event in New York City using a multilayer urban parameterization. *J. Appl. Meteor. Climatol.*, **54**, 283–301. doi:10.1175/JAMC-D-14-0028.1.

Holt, T. and J. Pullen, 2007: Urban canopy modeling of the New York City metropolitan area: A comparison and validation of single- and multilayer parameterizations. *Mon. Wea. Rev.*, **135**, 1906–1930. doi:10.1175/MWR3372.1.

Homer, C., C. Huang, L. Yang, B. Wylie, and M. Coan, 2004: Development of a 2001 National Land-Cover Database for the United States. *Photogramm. Eng. Remote Sens.*, **70** (7), 829–840. doi:10.14358/PERS.70.7.829.

——, and Coauthors, 2015: Completion of the 2011 National Land Cover Database for the conterminous United States - Representing a decade of land cover change information. *Photogramm. Eng. Remote Sensing*, **81** (5), 346–354. doi:10.14358/PERS.81.5.345.

Howells, P. A. C., R. Rotunno, and R. K. Smith, 1988: A comparative study of atmospheric and laboratory-analogue numerical tornado-vortex models. *Q. J. R. Meteorol. Soc.*, **114**, 801–822. doi:10.1002/qj.49711448113.

Huff, F. A. and S. A. Changnon, 1973: Precipitation modification by major urban areas. *Bull. Amer. Meteor. Soc.*, **54**, 1220–1232. doi:10.1175/1520-0477(1973)054<1220:PMBMUA>2.0.CO;2.

Husain, S. Z., S. Bélair, and S. Leroyer, 2014: Influence of soil moisture on urban microclimate and surface-layer meteorology in Oklahoma City. *J. Appl. Meteor. Climatol.*, **53**, 83–98. doi:10.1175/JAMC-D-13-0156.1.

Hu, X.-M. M., P. M. Klein, M. Xue, J. K. Lundquist, F. Zhang, and Y. Qi, 2013: Impact of low-level jets on the nocturnal urban heat island intensity in Oklahoma city. *J. Appl. Meteor. Climatol.*, **52**, 1779–1802. doi:10.1175/JAMC-D-13-0256.1.

Hu, X.-M. and M. Xue, 2016: Influence of synoptic sea breeze fronts on the urban heat island intensity in Dallas-Fort Worth, Texas. *Mon. Wea. Rev.*, **144**, 151015110409008 pp. doi:10.1175/MWR-D-15-0201.1.

——, J. W. Nielsen-Gammon, and F. Zhang, 2010: Evaluation of three planetary boundary layer schemes in the WRF model. *J. Appl. Meteor. Climatol.*, **49**, 1831–1844. doi:10.1175/2010JAMC2432.1.

——, P. M. Klein, M. Xue, A. Shapiro, and A. Nallapareddy, 2013: Enhanced vertical mixing associated with a nocturnal cold front passage and its impact on near-surface temperature and ozone concentration. *J. Geophys. Res. Atmos.*, **118** (7), 2714–2728. doi:10.1002/jgrd.50309.

——, M. Xue, P. M. Klein, B. G. Illston, and S. Chen, 2016: Analysis of urban effects in Oklahoma City using a dense surface observing network. *J. Appl. Meteor. Climatol.*, **55**, 723–741. doi:10.1175/JAMC-D-15-0206.1.

Jacquemin, B. and J. Noilhan, 1990: Sensitivity study and validation of a land surface parameterization using the HAPEX-MOBILHY data set. *Bound. Layer Meteor.*, **52** (1-2), 93–134. doi:10.1007/BF00123180.

Jiménez, P. a., J. Dudhia, J. F. González-Rouco, J. Navarro, J. P. Montávez, and E. García-Bustamante, 2012: A revised scheme for the WRF surface layer formulation. *Mon. Wea. Rev.*, **140**, 898–918. doi:10.1175/MWR-D-11-00056.1.

Johnson, A., X. Wang, F. Kong, and M. Xue, 2011a: Hierarchical cluster analysis of a convection-allowing ensemble during the Hazardous Weather Testbed 2009 Spring Experiment. Part I: Development of the object-oriented cluster analysis method for precipitation fields. *Mon. Wea. Rev.*, **139**, 3673–3693. doi:10.1175/MWR-D-11-00015.1.

——, ——, M. Xue, and F. Kong, 2011b: Hierarchical cluster analysis of a convection-allowing ensemble during the Hazardous Weather Testbed 2009 Spring Experiment. Part II: Ensemble clustering over the whole experiment period. *Mon. Wea. Rev.*, **139**, 3694–3710. doi:10.1175/MWR-D-11-00016.1.

Johns, R. H. and C. A. Doswell III, 1992: Severe Local Storms Forecasting. *Wea. Forecasting*, **7**, 588–612. doi:10.1175/1520-0434(1992)007<0588:SLSF>2.0.CO;2.

Journel, A. G. and C. J. Huijbrgts, 2004: *Mining Geostatistics.* The Blackburn Press, 600 pp.

Kain, J. S., and Coauthors, 2008: Some practical considerations regarding horizontal resolution in the first generation of operational convection-allowing NWP. *Wea. Forecasting*, **23**, 931–952. doi:10.1175/WAF2007106.1.

Kamal, S., H.-P. Huang, and S. W. Myint, 2015: The influence of urbanization on the climate of the Las Vegas metropolitan area: A numerical study. *J. Appl. Meteor. Climatol.*, **54**, 2157–2177. doi:10.1175/JAMC-D-15-0003.1.

Kar, S., Y.-A. Liou, and K.-J. Ha, 2009: Aerosol effects on the enhancement of cloud-to-ground lightning over major urban areas of South Korea. *Atmos. Res.*, **92** (1), 80–87. doi:10.1016/j.atmosres.2008.09.004.

Kawecki, S., G. M. Henebry, and A. L. Steiner, 2016: Effects of urban plume aerosols on a mesoscale convective system. *J. Atmos. Sci.*, **73**, 4641–4660. doi:10.1175/JAS-D-16-0084.1.

Klein, P. M., 2012: Metropolitan effects on atmospheric patterns: Important scales. *Metropolitan sustainability: Understanding and Improving the Urban Environment*, Zeeman, F., Ed., Woodhead Publishing, 173–204.

—— and J. M. Galvez, 2014: Flow and turbulence characteristics in a suburban street canyon. *Environ. Fluid Mech.*, **15** (2), 419–438. doi:10.1007/s10652-014-9352-5.

Kusaka, H. and F. Kimura, 2004: Thermal effects of urban canyon structure on the nocturnal heat island: Numerical experiment using a mesoscale model coupled with an urban canopy Model. *J. Appl. Meteor.*, **43** (12), 1899–1910. doi:10.1175/JAM2169.1.

——, H. Kondo, Y. Kikegawa, and F. Kimura, 2001: A simple single-layer urban canopy model for atmospheric models: Comparison with multi-layer and slab models. *Bound. Layer Meteor.*, **101** (3), 329–358. doi:10.1023/A:1019207923078.

Lacke, M. C., T. Mote, and J. M. Shepherd, 2009: Aerosols and associated precipitation patterns in Atlanta. *Atmos. Environ.*, **43**, 4359–4373.

Lee, S.-H. H., and Coauthors, 2011: Evaluation of urban surface parameterizations in the WRF model using measurements during the Texas Air Quality Study 2006 field campaign. *Atmos. Chem. Phys.*, **11** (5), 2127–2143. doi:10.5194/acp-11-2127-2011.

Lewellen, W. S., 1993: Tornado vortex theory. *Tornado Its Struct. Dyn. Predict. Hazards*, Vol. 79, *Geophys. Monogr.*, Amer. Geophys. Union, 19–39.

Li, D., E. Bou-Zeid, M. L. Baeck, S. Jessup, and J. A. Smith, 2013: Modeling land surface processes and heavy rainfall in urban environments: Sensitivity to urban surface representations. *J. Hydrometeor.*, **14**, 1098–1118. doi:10.1175/JHM-D-12-0154.1.

Lin, C.-Y., F. Chen, J. Huang, W.-C. Chen, Y.-A. Liou, W.-N. Chen, and S.-C. Liu, 2008: Urban heat island effect and its impact on boundary layer development and landsea circulation over northern Taiwan. *Atmos. Environ.*, **42** (22), 5635–5649. doi:10.1016/j.atmosenv.2008.03.015.

Liu, Y., F. Chen, T. Warner, and J. B. Basara, 2006: Verification of a mesoscale data-assimilation and forecasting system for the Oklahoma City area during the joint urban 2003 field project. *J. Appl. Meteor. Climatol.*, **45**, 912–929. doi:10.1175/JAM2383.1.

Li, W., S. Chen, G. Chen, W. Sha, C. Luo, Y. Feng, Z. Wen, and B. Wang, 2011: Urbanization signatures in strong versus weak precipitation over the Pearl River Delta metropolitan regions of China. *Environ. Res. Lett.*, **6.** doi:10.1088/1748-9326/6/3/034020.

Loose, T. and R. D. Bornstein, 1977: Observations of mesoscale effects on frontal movement through an urban area. *Mon. Wea. Rev.*, **105**, 563–571. doi:10.1175/1520-0493(1977)105<0563:OOMEOF>2.0.CO;2.

Loridan, T. and C. S. B. Grimmond, 2012: Multi-site evaluation of an urban land-surface model: Intra-urban heterogeneity, seasonality and parameter complexity requirements. *Q. J. R. Meteorol. Soc.*, **138** (665), 1094–1113. doi:10.1002/qj.963.

Loveland, T. R., B. C. Reed, J. F. Brown, D. O. Ohlen, Z. Zhu, L. Yang, and J. W. Merchant, 2000: Development of a global land cover characteristics database and IGBP DISCover from 1 km AVHRR data. *Int. J. Remote Sens.*, **21** (6-7), 1303–1330. doi:10.1080/014311600210191.

Mansell, E. R., C. L. Ziegler, and E. C. Bruning, 2010: Simulated electrification of a small thunderstorm with two-moment bulk microphysics. *J. Atmos. Sci.*, **67**, 171–194. doi:10.1175/2009JAS2965.1.

Markowski, P. M. and N. Dotzek, 2011: A numerical study of the effects of orography on supercells. *Atmos. Res.*, **100** (4), 457–478. doi:10.1016/j.atmosres.2010.12.027.

—— and Y. P. Richardson, 2014: The influence of environmental low-level shear and cold pools on tornadogenesis: Insights from idealized simulations. *J. Atmos. Sci.*, **71**, 243–275. doi:10.1175/JAS-D-13-0159.1.

——, J. M. Straka, and E. N. Rasmussen, 2002: Direct surface thermodynamic observations within the rear-flank downdrafts of nontornadic and tornadic supercells. *Mon. Wea. Rev.*, **130**, 1692–1721. doi:10.1175/1520-0493(2002)130<1692.

——, and Coauthors, 2012: The pretornadic phase of the Goshen County, Wyoming, supercell of 5 June 2009 intercepted by VORTEX2. Part II: Intensification of low-level rotation. *Mon. Wea. Rev.*, **140**, 2916–2938. doi:10.1175/MWR-D-11-00337.1..

Martilli, A., 2002: Numerical study of urban impact on boundary layer structure: Sensitivity to wind speed, urban morphology, and rural soil moisture. *J. Appl. Meteor.*, **41** (12), 1247–1266. doi:10.1175/1520-0450(2002)041<1247:NSOUIO>2.0.CO;2.

Matsui, T. and W. K. Tao, 2007: Goddard radiation and aerosol direct effect in Goddard WRF. *NASA/UMD WRF Work.*, College Park, Maryland, NASA and University of Maryland, College Park, 12 pp. [Available online at http://www.atmos.umd.edu/%5Ctextasciitilde%7B%7Dmartini/wrfchem/ppt/WRF_Toshi.ppt.]

McPherson, R. A., and Coauthors, 2007: Statewide monitoring of the mesoscale environment: A technical update on the Oklahoma Mesonet. *J. Atmos. Oceanic Technol.*, **24**, 301–321. doi:10.1175/JTECH1976.1.

Mercer, L. D., and Coauthors, 2011: Comparing universal kriging and land-use regression for predicting concentrations of gaseous oxides of nitrogen (NOx) for the Multi-Ethnic Study of Atherosclerosis and Air Pollution (MESA Air). *Atmos. Environ.*, **45** (26), 4412–4420. doi:10.1016/j.atmosenv.2011.05.043.

Miao, S., F. Chen, M. a. LeMone, M. Tewari, Q. Li, and Y. Wang, 2009: An observational and modeling study of characteristics of urban heat island and boundary layer structures in Beijing. *J. Appl. Meteor. Climatol.*, **48**, 484–501. doi:10.1175/2008JAMC1909.1.

——, ——, Q. Li, and S. Fan, 2011: Impacts of urban processes and urbanization on summer precipitation: A case study of heavy rainfall in Beijing on 1 August 2006. *J. Appl. Meteor. Climatol.*, **50**, 806–825. doi:10.1175/2010JAMC2513.1.

Monin, A. S. and A. M. Obukhov, 1954: Basic laws of turbulent mixing in the surface layer of the atmosphere. *Contrib. Geophys. Inst. Acad. Sci. USSR*, **24** (151), 163–187.

Moore, N. and S. Rojstaczer, 2002: Irrigation's influence on precipitation: Texas High Plains, U.S.A. *Geophys. Res. Lett.*, **29** (16), 2–1–2–4. doi:10.1029/2002GL014940.

Mote, T. L., M. C. Lacke, and J. M. Shepherd, 2007: Radar signatures of the urban effect on precipitation distribution: A case study for Atlanta, Georgia. *Geophys. Res. Lett.*, **34** (20). doi:10.1029/2007GL031903.

Murtagh, F. and P. Legendre, 2014: Ward's hierarchical agglomerative clustering method: Which algorithms implement Ward's criterion? *J. Classif.*, **31** (3), 274–295. doi:10.1007/s00357-014-9161-z.

Nakaegawa, T. and M. Kanamitsu, 2006: Cluster analysis of the seasonal forecast skill of the NCEP SFM over the PacificNorth America sector. *J. Climate*, **19**, 123–138. doi:10.1175/JCLI3609.1.

Nakanishi, M., 2000: Large-eddy simulation of radiation fog. *Bound. Layer Meteor.*, **94** (3), 461–493. doi:10.1023/A:1002490423389.

——, 2001: Improvement of the Mellor-Yamada turbulence closure model based on large-eddy simulation data. *Bound. Layer Meteor.*, **99** (3), 349–378. doi:10.1023/A:1018915827400.

—— and H. Niino, 2004: An improved Mellor-Yamada level-3 model with condensation physics: Its design and verification. *Bound. Layer Meteor.*, **112** (1), 1–31. doi:10.1023/B:BOUN.0000020164.04146.98.

—— and ——, 2006: An improved Mellor-Yamada level-3 model: Its numerical stability and application to a regional prediction of advection fog. *Bound. Layer Meteor.*, **119** (2), 397–407. doi:10.1007/s10546-005-9030-8.

Nemunaitis-Monroe, K. L., P. M. Klein, J. B. Basara, and E. Fedorovich, 2016: Sensitivity of predictions of the urban surface energy balance and heat island to variations of urban canopy parameters in simulations with the WRF model (In review, J. Appl. Meteor. Climatol.).

Ngan, F., H. Kim, P. Lee, K. Al-Wali, and B. Dornblaser, 2013: A study of nocturnal surface wind speed overprediction by the WRF-ARW model in southeastern Texas. *J. Appl. Meteor. Climatol.*, **52**, 2638–2653. doi:10.1175/JAMC-D-13-060.1.

Niyogi, D., P. Pyle, M. Lei, S. P. Arya, C. M. Kishtawal, M. Shepherd, F. Chen, and B. Wolfe, 2011: Urban modification of thunderstorms: An observational storm climatology and model case study for the Indianapolis urban region. *J. Appl. Meteor. Climatol.*, **50**, 1129–1144. doi:10.1175/2010JAMC1836.1.

Noh, Y., W. G. Cheon, S. Y. Hong, and S. Raasch, 2003: Improvement of the k-profile model for the planetary boundary layer based on large eddy simulation data. *Bound. Layer Meteor.*, **107** (2), 401–427. doi:10.1023/A:1022146015946.

Nowotarski, C. J. and A. A. Jensen, 2013: Classifying proximity soundings with self-organizing maps toward improving supercell and tornado forecasting. *Wea. Forecasting*, **28**, 783–801. doi:10.1175/WAF-D-12-00125.1.

Nunez, M. and T. R. Oke, 1977: The energy balance of an urban canyon. *J. Appl. Meteor.*, **16** (1), 11–19. doi:10.1175/1520-0450(1977)016<0011.

Oke, T. R., 1976: The distinction between canopy and boundary-layer urban heat islands. *Atmosphere (Basel).*, **14** (4), 268–277. doi:10.1080/00046973.1976.9648422.

——, 1981: Canyon geometry and the nocturnal urban heat island: Comparison of scale model and field observations. *J. Climatol.*, **1** (3), 237–254. doi:10.1002/joc.3370010304.

——, 1982: The energetic basis of the urban heat island. *Q. J. R. Meteorol. Soc.*, **108** (455), 1–24. doi:10.1002/qj.49710845502.

——, 1987: *Boundary Layer Climates.* Academic Press, 345 pp.

——, G. T. Johnson, D. G. Steyn, and I. D. Watson, 1991: Simulation of surface urban heat islands under 'ideal' conditions at night. Part 2: Diagnosis of causation. *Bound. Layer Meteor.*, **56** (4), 339–358. doi:10.1007/BF00119211.

Orville, R. E., and Coauthors, 2001: Enhancement of cloud-to-ground lightning over Houston, Texas. *Geophys. Res. Lett.*, **28** (13), 2597–2600. doi:10.1029/2001GL012990.

Paulson, C. A., 1970: The mathematical representation of wind speed and temperature profiles in the unstable atmospheric surface layer. *J. Appl. Meteor.*, **9**, 857–861. doi:10.1175/1520-0450(1970)009<0857:TMROWS>2.0.CO;2.

Pitman, E., 1937: Significance tests which may be applied to samples from any populations: III. The analysis of variance test. *Biometrika*, **29** (3/4), 322–335. doi:10.2307/2332008.

Reames, L. J. and D. J. Stensrud, 2017: Sensitivity of simulated urban-atmosphere interactions in Oklahoma City to urban parameterization. *J. Appl. Meteor. Climatol.*, in press.

Rose, L. S., J. A. Stallins, and M. L. Bentley, 2008: Concurrent cloud-to-ground lightning and precipitation enhancement in the Atlanta, Georgia (United States), urban region. *Earth Interact.*, **12**, 1–30. doi:10.1175/2008EI265.1.

Rotunno, R., 1979: A study in tornado-like vortex dynamics. *J. Atmos. Sci.*, **36**, 140–155. doi:10.1175/1520-0469(1979)036<0140:ASITLV>2.0.CO;2.

Ryu, Y.-H., J. A. Smith, E. Bou-Zeid, and M. L. Baeck, 2016: The Influence of land surface heterogeneities on heavy convective rainfall in the BaltimoreWashington metropolitan area. *Mon. Wea. Rev.*, **144**, 553–573. doi:10.1175/MWR-D-15-0192.1.

Sailor, D. J., M. Georgescu, J. M. Milne, and M. A. Hart, 2015: Development of a national anthropogenic heating database with an extrapolation for international cities. *Atmos. Environ.*, **118**, 7–18. doi:10.1016/j.atmosenv.2015.07.016.

Salamanca, F., A. Krpo, A. Martilli, and A. Clappier, 2010: A new building energy model coupled with an urban canopy parameterization for urban climate simulationsPart I. Formulation, verification, and sensitivity analysis of the model. *Theor. Appl. Climatol.*, **99** (3-4), 331–344. doi:10.1007/s00704-009-0142-9.

Schenkman, A. D., M. Xue, and A. Shapiro, 2012: Tornadogenesis in a simulated mesovortex within a mesoscale convective system. *J. Atmos. Sci.*, **69**, 3372–3390. doi:10.1175/JAS-D-12-038.1.

Schneider, J. M., D. K. Fisher, R. L. Elliott, G. O. Brown, and C. P. Bahrmann, 2003: Spatiotemporal Variations in Soil Water: First Results from the ARM SGP CART Network. *J. Hydrometeor.*, **4**, 106–120.

Seino, N., T. Aoyagi, and H. Tsuguti, 2016: Numerical simulation of urban impact on precipitation in Tokyo: How does urban temperature rise affect precipitation? *Urban Clim.* doi:10.1016/j.uclim.2016.11.007.

Shaffer, S. R., W. T. L. Chow, M. Georgescu, P. Hyde, G. D. Jenerette, A. Mahalov, M. Moustaoui, and B. L. Ruddell, 2015: Multiscale modeling and evaluation of urban surface energy balance in the Phoenix metropolitan area. *J. Appl. Meteor. Climatol.*, **54**, 322–338. doi:10.1175/JAMC-D-14-0051.1.

Shaffer, S. R., M. Moustaoui, A. Mahalov, and B. L. Ruddell, 2016: A method of aggregating heterogeneous subgrid land-cover input data for multiscale urban parameterization. *J. Appl. Meteor. Climatol.*, **55**, 1889–1905. doi:10.1175/JAMC-D-16-0027.1.

Sharma, A., H. J. Fernando, A. F. Hamlet, J. J. Hellmann, M. Barlage, and F. Chen, 2016: Urban meteorological modeling using WRF: A sensitivity study. *Int. J. Climatol.* doi:10.1002/joc.4819.

Shepherd, J. M., 2005: A review of current investigations of urban-induced rainfall and recommendations for the future. *Earth Interact.*, **9**, 1–27. doi:10.1175/EI156.1.

——, 2006: Evidence of urban-induced precipitation variability in arid climate regimes. *J. Arid Environ.*, **67**, 607–628. doi:10.1016/j.jaridenv.2006.03.022.

—— and S. J. Burian, 2003: Detection of urban-induced rainfall anomalies in a major coastal city. *Earth Interact.*, **7**, 1–17. doi:10.1175/1087-3562(2003)007<0001.

——, H. Pierce, and A. J. Negri, 2002: Rainfall modification by major urban areas: Observations from spaceborne rain radar on the TRMM satellite. *J. Appl. Meteor.*, **41** (7), 689–701. doi:10.1175/1520-0450(2002)041<0689.

——, M. Carter, M. Manyin, D. Messen, and S. Burian, 2010a: The impact of urbanization on current and future coastal precipitation: A case study for Houston. *Environ. Plan. B Plan. Des.*, **37**, 284–304. doi:10.1068/b34102t.

——, J. A. Stallins, M. Jin, and T. Mote, 2010b: Urbanization: Impacts on clouds, precipitation, and lightning. *Urban Ecosyst. Ecol.*, American Society of Agronomy, Crop Science Society of America, Soil Science Society of America, 1–27.

Siongco, A. C., C. Hohenegger, and B. Stevens, 2017: Sensitivity of the summertime tropical Atlantic precipitation distribution to convective parameterization and model resolution in ECHAM6. *J. Geophys. Res. Atmos.*, **122** (5), 2579–2594. doi:10.1002/2016JD026093.

Skamarock, W. and J. Klemp, 2008: A time-split nonhydrostatic atmospheric model for weather research and forecasting applications. *J. Comput. Phys.*, **227** (7), 3465–3485. doi:10.1016/j.jcp.2007.01.037.

Smith, J. A., M. L. Baeck, J. E. Morrison, P. Sturdevant-Rees, D. F. Turner-Gillespie, and P. D. Bates, 2002: The regional hydrology of extreme floods in an urbanizing drainage basin. *J. Hydrometeor.*, **3**, 267–282. doi:10.1175/1525-7541(2002)003<0267.

Smoliak, B. V., P. K. Snyder, T. E. Twine, P. M. Mykleby, and W. F. Hertel, 2015: Dense network observations of the Twin Cities canopy-layer urban heat island. *J. Appl. Meteor. Climatol.*, **54**, 1899–1917. doi:10.1175/JAMC-D-14-0239.1.

Stein, U. and P. Alpert, 1993: Factor separation in numerical simulations. *J. Atmos. Sci.*, **50**, 2107–2115. doi:10.1175/1520-0469(1993)050<2107:FSINS>2.0.CO;2.

Stensrud, D. J., and Coauthors, 2009: Convective-scale warn-on-forecast system: A vision for 2020. *Bull. Amer. Meteor. Soc.*, **90**, 1487–1499. doi:10.1175/2009BAMS2795.1.

Stewart, I. D., 2011: A systematic review and scientific critique of methodology in modern urban heat island literature. *Int. J. Climatol.*, **31** (2), 200–217. doi:10.1002/joc.2141.

—— and T. R. Oke, 2012: Local climate zones for urban temperature studies. *Bull. Amer. Meteor. Soc.*, **93**, 1879–1900. doi:10.1175/BAMS-D-11-00019.1.

Takane, Y., H. Kusaka, and H. Kondo, 2015: Investigation of a recent extreme high-temperature event in the Tokyo metropolitan area using numerical simulations: The potential role of a 'hybrid' foehn wind. *Q. J. R. Meteorol. Soc.*, **141** (690), 1857–1869. doi:10.1002/qj.2490.

Tan, Y. B., L. Peng, Z. Shi, and H. R. Chen, 2016: Lightning flash density in relation to aerosol over Nanjing (China). *Atmos. Res.*, **174-175**, 1–8. doi:10.1016/j.atmosres.2016.01.009.

Thielen, J., W. Wobrock, A. Gadian, P. Mestayer, and J.-D. Creutin, 2000: The possible influence of urban surfaces on rainfall development: a sensitivity study in 2D in the meso-γ-scale. *Atmos. Res.*, **54**, 15–39. doi:10.1016/S0169-8095(00)00041-7.

Thompson, R. L. and R. Edwards, 2000: An overview of environmental conditions and forecast implications of the 3 May 1999 tornado outbreak. *Wea. Forecasting*, **15**, 682–699.

——, ——, J. A. Hart, K. L. Elmore, and P. M. Markowski, 2003: Close proximity soundings within supercell environments obtained from the Rapid Update Cycle. *Wea. Forecasting*, **18**, 1243–1261. doi:10.1175/1520-0434(2003)018<1243:CPSWSE>2.0.CO;2.

Togstad, W. E., J. M. Davies, S. J. Corfidi, D. R. Bright, and A. R. Dean, 2011: Conditional probability estimation for significant tornadoes based on Rapid Update Cycle (RUC) profiles. *Wea. Forecasting*, **26**, 729–743. doi:10.1175/2011WAF2222440.1.

United Nations, 2015: World urbanization prospects: The 2014 revision. United Nations, Department of Economic and Social Affairs, Population Division Tech. Rep. ST/ESA/SER.A/366, 493 pp. [Available online at http://esa.un.org/unpd/wup/Publications/Files/WUP2014-Report.pdf.]

United States Census Bureau, 2010: 2010 Census. [Available online at http://www.census.gov/2010census/data/.]

Varquez, A. C. G., M. Nakayoshi, and M. Kanda, 2015: The effects of highly detailed urban roughness parameters on a sea-breeze numerical simulation. *Bound. Layer Meteor.*, **154** (3), 449–469. doi:10.1007/s10546-014-9985-4.

Wang, X., J. Liao, J. Zhang, C. Shen, W. Chen, and B. Xia, 2014: A numeric study of regional climate change induced by urban expansion in the Pearl River Delta, China. *J. Appl. Meteor. Climatol.*, **53**, 346–362. doi:10.1175/JAMC-D-13-054.1.

Wang, Y., C. L. Klipp, D. M. Garvey, D. A. Ligon, C. C. Williamson, S. S. Chang, R. K. Newsom, and R. Calhoun, 2007: Nocturnal low-level-jet-dominated atmospheric boundary layer observed by a doppler lidar over Oklahoma City during JU2003. *J. Appl. Meteor. Climatol.*, **46**, 2098–2109. doi:10.1175/2006JAMC1283.1.

Wang, Z.-H., E. Bou-Zeid, S. K. Au, and J. a. Smith, 2011: Analyzing the sensitivity of WRF's single-layer urban canopy model to parameter uncertainty using advanced monte carlo simulation. *J. Appl. Meteor. Climatol.*, **50**, 1795–1814. doi:10.1175/2011JAMC2685.1.

Ward, J. H., 1963: Hierarchical grouping to optimize an objective function. *J. Am. Stat. Assoc.*, **58** (301), 236–244. doi:10.1080/01621459.1963.10500845.

Webb, E. K., 1970: Profile relationships: The log-linear range, and extension to strong stability. *Q. J. R. Meteorol. Soc.*, **96** (407), 67–90. doi:10.1002/qj.49709640708.

Wilks, D. S., 2011: *Statistical Methods in the Atmospheric Sciences*, 3 ed. Academic Press, 675 pp.

Winguth, A. M. E. and B. Kelp, 2013: The urban heat island of the north-central Texas region and its relation to the 2011 severe Texas drought. *J. Appl. Meteor. Climatol.*, **52**, 2418–2433. doi:10.1175/JAMC-D-12-0195.1.

Wyngaard, J. C., 2004: Toward numerical modeling in the terra incognita. *J. Atmos. Sci.*, **61**, 1816–1826. doi:10.1175/1520-0469(2004)061¡1816:TNMITT¿2.0.CO;2.

Xian, G., C. Homer, J. Dewitz, J. Fry, N. Hossain, and J. Wickham, 2011: Change of impervious surface area between 2001 and 2006 in the conterminous United States. *Photogramm. Eng. Remote Sensing*, **77** (8), 758–762.

Xia, Y., and Coauthors, 2012: Continental-scale water and energy flux analysis and validation for the North American Land Data Assimilation System project phase 2 (NLDAS-2): 1. Intercomparison and application of model products. *J. Geophys. Res. Atmos.*, **117** (D3), D03109. doi:10.1029/2011JD016048.

Xu, X., M. Xue, and Y. Wang, 2015: The genesis of mesovortices within a real-data simulation of a bow echo system. *J. Atmos. Sci.*, **72**, 1963–1986. doi:10.1175/JAS-D-14-0209.1.

Yang, L., J. A. Smith, M. L. Baeck, E. Bou-Zeid, S. M. Jessup, F. Tian, and H. Hu, 2014a: Impact of urbanization on heavy convective precipitation under strong large-scale forcing: A case study over the MilwaukeeLake Michigan region. *J. Hydrometeor.*, **15**, 261–278. doi:10.1175/JHM-D-13-020.1.

——, F. Tian, J. A. Smith, and H. Hu, 2014b: Urban signatures in the spatial clustering of summer heavy rainfall events over the Beijing metropolitan region. *J. Geophys. Res. Atmos.*, **119**, 1203–1217. doi:10.1002/2013JD020762.

Yang, P., G. Ren, and W. Liu, 2013: Spatial and temporal characteristics of Beijing urban heat island intensity. *J. Appl. Meteor. Climatol.*, **52**, 1803–1816. doi:10.1175/JAMC-D-12-0125.1.

Yeung, J. K., J. A. Smith, M. L. Baeck, and G. Villarini, 2015: Lagrangian analyses of rainfall structure and evolution for organized thunderstorm systems in the urban corridor of the northeastern United States. *J. Hydrometeor.*, **16**, 1575–1595. doi:10.1175/JHM-D-14-0095.1.

Yin, Q. Z. and A. Berger, 2012: Individual contribution of insolation and CO2 to the interglacial climates of the past 800,000years. *Clim. Dyn.*, **38**, 709–724. doi:10.1007/s00382-011-1013-5.

Yow, D. M. and G. J. Carbone, 2006: The urban heat island and local temperature variations in Orlando, Florida. *Southeast. Geogr.*, **46** (2), 297–321. doi:10.1353/sgo.2006.0033.

Yussouf, N., D. J. Stensrud, and S. Lakshmivarahan, 2004: Cluster analysis of multimodel ensemble data over New England. *Mon. Wea. Rev.*, **132**, 2452–2462. doi:10.1175/1520-0493(2004)132<2452:CAOMED>2.0.CO;2.

Zhang, D.-L. and R. A. Anthes, 1982: A High-Resolution Model of the Planetary Boundary LayerSensitivity Tests and Comparisons with SESAME-79 Data. *J. Appl. Meteor.*, **21** (11), 1594–1609. doi:10.1175/1520-0450(1982)021<1594:AHRMOT>2.0.CO;2.

—— and W.-Z. Zheng, 2004: Diurnal cycles of surface winds and temperatures as simulated by five boundary layer parameterizations. *J. Appl. Meteor.*, **43** (1), 157–169. doi:10.1175/1520-0450(2004)043<0157.

——, Y.-X. Shou, R. R. Dickerson, and F. Chen, 2011: Impact of upstream urbanization on the urban heat island effects along the Washington-Baltimore corridor. *J. Appl. Meteor. Climatol.*, **50**, 2012–2029. doi:10.1175/JAMC-D-10-05008.1.